Internal Report
DESY F35D-95-12
November 1995

Measurement of Neutral and Charged Current Deep Inelastic Scattering Cross Sections at Very High Q^2

by

I. S. Ali

MEASUREMENT OF NEUTRAL AND CHARGED CURRENT DEEP INELASTIC SCATTERING CROSS SECTIONS AT VERY HIGH Q^2

by

ISSAM S. ALI

A dissertation submitted in partial fulfillment of the
requirements for the degree of

Doctor of Philosophy
(Physics)

at the
UNIVERSITY OF WISCONSIN — MADISON
1995

Acknowledgements

I would like to thank:

- My advisors, Wesley Smith and Don Reeder for their help and support over the years and for their patience in correcting the manuscripts of this thesis, despite their busy schedule.
- Costas Foudas, for teaching me electronics, making work at hardware fun, and for being a very good friend.
- Danny Krakauer for teaching me the bits and pieces of physics analysis and for his great contribution to this thesis.
- Carrie Fordham, for her friendship.
- The members of the exotics group, in particular B. Straub.
- The members of the Wisconsin group that went through the same "crunch" with me: Anna Goussiou, Bruce Behrens, and Sam Silverstein.
- the new members of the Wisconsin group for making the work at the Wisconsin office fun: Tony Vaiciulis and Mike Wodarczyk.
- All members of the ZEUS Collaboration for collecting the data upon which this dissertation is based, and for their interest in and advice on this subject.

- The DESY directorate for their strong support and encouragement.
- The HERA machine group for their remarkable achievements, which were essential for the successful completion of this work.
- The DESY computing and network services for their support.

To my father, Sadiq,
to my mother, Fatima,
and my wife, Nidhal.

Abstract

A quantitative study of Deep Inelastic Scattering (DIS) at very high momentum transfers, Q^2, is performed using the ZEUS detector at the HERA ep-collider at DESY. High Q^2 DIS events are observed in the Charged Current (CC - $W^{\pm}$-exchange) and Neutral Current (NC - γ/Z^0-exchange) modes at Q^2 up to and beyond the square of the mass of the heavy weak bosons. From an integrated luminosity of 0.54 pb^{-1}, a sample of 23 CC events and 436 NC events with $Q^2 > 400\mathrm{GeV}^2$ are identified. The CC and NC total cross-sections, the NC/CC ratio, and differential distributions in $d\sigma/dQ^2$ are reported. For the first time, charged-lepton scattering cross sections have been measured into the Q^2 range where the CC and NC cross sections are comparable.[2]

Contents

Chapter 1

INTRODUCTION

Particles interact via three forces. The strong force governs the interactions between quarks. The electroweak force unifies electromagnetic and weak forces. Charged particles interact via the electromagnetic force, while the decay of particles, e.g. β–decay, is caused by the weak force. Finally, large scale phenomena are governed by gravity, which is weak at the atomic and subatomic scales compared to the other forces and, therefore, is neglected at current energies accessible in particle physics experiments.

In field theory, particles are described as fields that transmit these forces. For example, the electromagnetic force in ep scattering is mediated by a virtual spin–1 photon (it is virtual because the intermediate state $ep\gamma$ violates energy conservation via the uncertainty principle). Strong forces are mediated by spin–1 gluons, and weak forces are governed by spin–1 W and Z exchanges.

Matter is composed of three types of particles: leptons (e, μ, τ, ν_e, ν_μ, ν_τ), gauge bosons (e.g. γ, W, and Z), and hadrons, which are made of quarks. The proton and the neutron are made of three quarks ($p = uud$, $n = ddu$), while mesons (e.g the pion) are made of quark-antiquark ($q\bar{q}$) pairs ($\pi^+ = u\bar{d}$). These hadrons have also been shown to contain a sea of gluons and $q\bar{q}$ pairs. The sea plays a major role in deep inelastic high energy collisions which directly

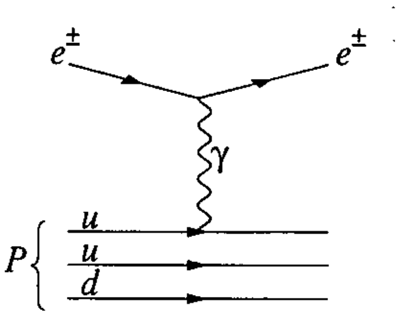

Figure 1.1: High energy collision in which a photon is able to resolve individual quarks.

scatter off individual quarks and gluons (figure 1.1).

Electromagnetic interactions are described by the Quantum Electrodynamics (QED). The photon, which transmits the electromagnetic force between charged particles, is described by an electromagnetic field A_μ that couples to the electron and proton "currents". These currents are probability currents whose forms arise from Dirac's equation, which describes spin–1/2 particle fields, or from the Klein-Gordon equation for spin–0 particles (e.g. π^+). [3]

Quark and gluon interactions are described by Quantum Chromodynamics (QCD) through the introduction of the color force. Quarks come in three colors: red, blue, and green (and antired, antiblue, and antigreen for antiquarks), with the gluon transferring the color force between gluons and quarks. A consequence of QCD is the statement that only colorless states can be free, and, therefore, observed. As a result, an individual quark cannot be set free because it has color. Therefore, for example, to study quarks, one has to scatter $e^{\pm}$ off

protons and study the scattered lepton and the struck quark, which manifests itself as a jet (when the quark separates from the other quarks in the proton, color interactions take over and decelerate the struck quark. As a result, it radiates hadrons, mostly π mesons, just like a decelerating electron radiates photons in bremsstrahlung. This hadron shower is called a *jet*).

Neutron β–decay and other interactions fall under the realm of the weak theory. The carriers of this force are the massive $W^{\pm}$ and Z^{o} that give rise to weak Charged and Neutral current interactions, respectively. Due to the $V-A$ (vector-axial) nature of the interactions, these interactions violate parity. This theory is unified with QED by the Glashow–Weinberg–Salam model of the "electroweak" theory.

A successful technique that explores the nature of these forces and the structure of hadrons is Deep Inelastic Scattering (DIS). Measurements of inclusive DIS cross sections have revealed new levels of the structure of hadrons. The gauge bosons provide excellent probes, especially at higher energies, into the proton. At high energies, the momentum transfer, Q^2, to the proton is large, resulting in a probe with small wavelength that resolves the proton structure. In addition, at high Q^2, a unique window is opened to study deviations from the Standard Model (QCD and the Glashow–Weinberg–Salam model of electroweak theory) and to look for new particles.

In Neutral Current (NC) DIS, the exchanged boson is the photon (figure 2.1) or the Z^{o} (figure 2.4) particle. In Charged Current (CC) DIS, a $W^{\pm}$ is exchanged (figure 2.2). The HERA (Hadron Electron Ring Anlage) accelerator, located at the Deuthches Electronen–Syncrotron (DESY) laboratory, in Hamburg, Germany, offers the unique study of such interactions through collisions of 26.7 GeV electrons with 820 GeV protons. In 1993, ZEUS, one of the two currently operational HERA experiments, collected a total integrated luminosity of $0.54 pb^{-1}$.

This thesis describes the measurements of NC and CC DIS cross sections at $Q^2 > 400\ GeV^2$ done with the ZEUS experiment. This is the first measurement in which NC and CC processes are compared at high Q^2, where both are expected to be of comparable strength. The H1 collaboration has measured the total CC cross section and demonstrated that the CC propagator term has a finite mass.[1] ZEUS has measured this mass and found that $M_W = 76 \pm 16 \pm 13\ GeV$.[2]

The organization of this thesis is as follows: Chapter 2 gives the theoretical background. The experimental setup is explained in Chapters 3, 4, and 5, in which HERA, the ZEUS detector, and the ZEUS calorimeter readout and trigger are described, respectively. Analysis of the data starts with kinematic reconstruction in Chapter 6.1, which also describes the Monte Carlo simulation. Data selection is given in Chapter 7. An important part of the analysis is an energy correction method applied to the CC data and this is detailed in Chapter 8. The measured cross sections and error analysis on these measurements are in Chapter 9. Finally, Chapter 10 contains the conclusions.

Chapter 2

THEORETICAL BACKGROUND

2.1 The Gauge Principle

Electroweak and QCD theories are gauge theories. When a local gauge transformation is applied (i.e., introducing an extra phase factor in the particle wavefunction that depends on space–time coordinates), then the theory is not invariant. But, if a compensating new field is introduced that transforms in a particular way and interacts with the original particles in the theory, invariance is restored. The first attempt to extract a theory from local gauge invariance was done by Yang and Mills.[4]

The photon, W, Z, and gluons are called gauge particles because they arise naturally from demanding local gauge invariance. They are precisely the compensating fields that are needed to restore local invariance. This can be understood from the following argument: any change in phase at some space–time point will have to propagate with a *finite* speed before it reaches other points. The carrier of this signal is the gauge particle. Only local gauge transformations take this finiteness of speed into account since these transformations are not simultaneous because, by definition, they perform *different* transformations at different space–time points due to the dependence of the extra phase factor on these points.

The Dirac Lagrangian, which describes free spin-1/2 charged particles, is

$$\mathcal{L} = i\bar{\psi}\gamma^\mu\partial_\mu\psi - m\bar{\psi}\psi \tag{2.1}$$

where ψ is a spinor field and $\bar{\psi}$ is its adjoint. Applying the Euler-Lagrange equation to $\bar{\psi}$, one obtains Dirac's equation for ψ (and *vice versa*). Under the local gauge transformation

$$\psi \to e^{-ie\alpha(x)}\psi \tag{2.2}$$

where $x = x^\mu$ denotes space-time points and α is some function of x, $\mathcal{L}$ becomes

$$\mathcal{L} \to \mathcal{L} + e(\partial\alpha)\bar{\psi}\gamma^\mu\psi \tag{2.3}$$

Therefore, $\mathcal{L}$ is not invariant. This extra term suggests how to recast $\mathcal{L}$ so that it becomes invariant under (2.2). Rewriting $\mathcal{L}$ as

$$\mathcal{L} = i\bar{\psi}\gamma^\mu\partial_\mu\psi - m\bar{\psi}\psi - (e\bar{\psi}\gamma^\mu\psi)A_\mu \tag{2.4}$$

where A_μ is a new gauge field that transforms according to

$$A_\mu \to A_\mu + \partial\alpha \tag{2.5}$$

then this new $\mathcal{L}$ is now invariant under (2.2). The last term in equation (2.4) is of the form $j^\mu A_\mu$ with $j^\mu = e(\bar{\psi}\gamma^\mu\psi)$, the transition current. It is this term that is used in perturbation theory to calculate cross sections since it embodies the interaction of the particle field with A^μ. By requiring $\mathcal{L}$ to be invariant under local gauge transformations, a new field, A_μ, must be introduced. One recognizes A_μ as the photon field and e as the charge of the particle that interacts with the photon. Equation (2.2) is called a $U(1)$ local transformation.

Yang-Mills fields have two interacting spin-1/2 fields. We use equation (2.1) where ψ is a two-component column vector ($\psi = (\psi_1 \quad \psi_2)^T$) and $\psi_{1,2}$ obey Dirac's equation. Since ψ is a two-component vector, then $\alpha(x)$ in (2.2) is a 2×2 matrix. But any 2×2 matrix can be expressed as a linear combination of Pauli matrices. Therefore, α is replaced by $\boldsymbol{\alpha} = \sum_i a_i\boldsymbol{\sigma}_i$ (σ_i are Pauli matrices) and e is replaced by $\mathbf{e} = (e_1, e_2, e_3)$. As a result, $e\alpha(x)$ is changed to $\mathbf{e}\cdot\boldsymbol{\alpha}(x)$. Requiring local gauge invariance gives rise to *three massless* gauge bosons. Through the Higgs mechanism, these particles acquire mass and are identified as $W^\pm$ and Z^o bosons. This is referred to as an $SU(2)$ tranformation. (In electroweak theory (section 2.4 below) the Lagrangian is different. Demanding local gauge invariance produces, through the Higgs mechanism, a *massless* boson —the photon— and three *massive* bosons —$W^\pm$ and Z^o). For QCD, ψ is a three-component vector, corresponding to three color charges, and α is a 3×3 matrix given in terms of the eight Gell-Mann matrices, giving eight massless bosons (gluons). In this case, the transformation is an $SU(3)$ transformation.

2.2 Electromagnetic Interactions

2.2.1 $ep \to eX$ DIS

Deep Inelastic Scattering (DIS) of $ep \to eX$ is shown in figure 2.1. In the diagram, a blob is put at the proton vertex which "parametrizes" the proton structure. The incoming electron has 4-momentum $l = (E_e, \mathbf{l})$ and it scatters with 4-momentum $l' = (E_e', \mathbf{l}')$. The proton enters in with $p = (E_p, \mathbf{p})$ and collides with the exchanged photon, γ. In DIS, γ is virtual and has enough

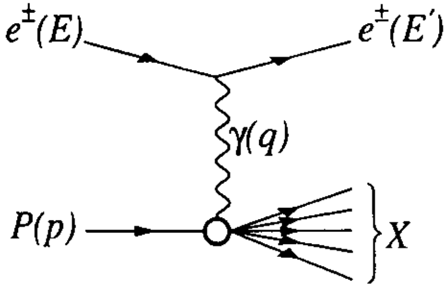

Figure 2.1: $ep \rightarrow eX$, photon exchange.

4-momentum, $q = l - l'$, to break up the proton, producing the system X, which is observed as jet(s) in the detector.

The cross section for this process is given by

$$d\sigma_{EM} = \frac{1}{F}\overline{|\mathcal{M}|^2}\frac{d^3E'_e}{2E'(2\pi)^3} \tag{2.6}$$

where $\overline{|\mathcal{M}|^2}$ is the square of the invariant amplitude averaged over incoming spins and summed over final spins. F is the flux of colliding particles and is given by

$$F = 4(|l|E_p + |p|E_e) = 4[(p\cdot l)^2 - m_e^2 m_p^2]^{1/2} \tag{2.7}$$

where m_e and m_p are the electron and proton rest masses, respectively.

$\overline{|\mathcal{M}|^2}$ can be written as[5]

$$\overline{|\mathcal{M}|^2} = \frac{16\pi^2\alpha^2}{Q^4}L^{\mu\nu}W_{\mu\nu}4\pi m_p \tag{2.8}$$

The leptonic tensor, $L^{\mu\nu}$, is[5]

$$L^{\mu\nu} = 2\left[l'^{\mu}l^{\nu} + l'^{\nu}l^{\mu} - (l'\cdot l - m_e^2)g^{\mu\nu}\right] \tag{2.9}$$

Note that

$$q_\mu L^{\mu\nu} = q_\nu L^{\mu\nu} = 0 \tag{2.10}$$

which reflects current conservation. The proton tensor, $W_{\mu\nu}$, is not the same as the electron tensor because in DIS the photon does not see a point particle. Instead, it sees the structure of the proton. $W_{\mu\nu}$ must obey two symmetry conditions: Lorentz invariance and electromagnetic current conservation similar to (2.10). It must be constructed from the available tensors and 4-momentum vectors at the proton vertex. There are two *independent* vectors, p and q, and one tensor, $g_{\mu\nu}$. The antisymmetric tensor $\epsilon_{\mu\nu\alpha\beta}$ is ruled out because it does not conserve parity. Therefore, the most general form of the tensor can be written as

$$W_{\mu\nu} = -W_1 g_{\mu\nu} + \frac{W_2}{m_p^2}p_\mu p_\nu + \frac{W_4}{m_p^2}q_\mu q_\nu + \frac{W_5}{m_p^2}(p_\mu q_\nu + p_\nu q_\mu) \tag{2.11}$$

which is Lorentz invariant. The term with W_3 is omitted because it is parity violating. The W_i's are functions of Lorentz scalar variables that are constructed from the 4-momenta available at the proton vertex. There are two independent scalar variables and they are taken to be the Lorentz invariant quantities

$$x = \frac{Q^2}{2p\cdot q} \quad , \quad Q^2 = -q^2 \tag{2.12}$$

where x represents the fraction of the proton momentum carried by the struck quark. From the current conservation condition (cf. 2.10)

$$q^\mu W_{\mu\nu} = q^\nu W_{\mu\nu} = 0 \tag{2.13}$$

W_5 and W_4 can be re-expressed in terms of W_1 and W_2, yielding

$$W_{\mu\nu} = \left(-g_{\mu\nu} + \frac{q_\mu q_\nu}{q^2}\right)W_1 + \left(p_\mu - \frac{p\cdot q}{q^2}q_\mu\right)\left(p_\nu - \frac{p\cdot q}{q^2}q_\nu\right)\frac{W_2}{m_p^2} \tag{2.14}$$

Now we can evaluate $\overline{|\mathcal{M}|^2}$ in (2.8). From (2.10), and neglecting the masses of the electron and the proton

$$L^{\mu\nu}W_{\mu\nu} = 4(l\cdot l')W_1 + \frac{2W_2}{m_p^2}(p\cdot l)(p\cdot l') \tag{2.15}$$

From 4-momentum conservation at the electron vertex we have

$$Q^2 = -q^2 = -(l-l')^2 \simeq -2(l\cdot l') = 4E_eE_e'\sin^2\frac{\theta}{2} \tag{2.16}$$

where the $l^2 = l'^2 = m_e^2 \simeq 0$ and θ is the scattered electron's angle. Also, we introduce another Lorentz invariant variable, y, given by

$$y = \frac{p\cdot q}{p\cdot l} \tag{2.17}$$

In the center of mass, $l = (E, \hat{z}E)$, $p = (E, -\hat{z}E)$, $l' = (E, \hat{x}E\sin\theta, 0, \hat{z}E\cos\theta)$, where θ is the center of mass scattering angle of the electron, resulting in

$$y = \frac{1}{2}(1-\cos\theta) \tag{2.18}$$

Using (2.16) in (2.17) one obtains

$$p\cdot l' = (1-y)(l\cdot p) \tag{2.19}$$

From (2.19) and (2.16), equation (2.15) becomes

$$L^{\mu\nu}W_{\mu\nu} = 2Q^2W_1 + \frac{W_2}{m_p^2}\frac{s^2}{2}(1-y) \tag{2.20}$$

where $s = (p+l)^2 \simeq 2(p\cdot l)$, square of the center of mass energy. The cross section is usually expressed in terms of the variables Q^2 and x. Since these are Lorentz invariant, one can find the cross section in any frame in terms of these variables, making the cross section itself Lorentz invariant. To make the mathematics simple, we find the pure photon exchange cross section in the proton rest frame where $p = (m_p, 0)$. In this case, from (2.6)

$$d^3E_e' = E_e'^2dE'd\Omega = \frac{2\pi yE_e'}{x}dxdQ^2 \tag{2.21}$$

and

$$F = 2s = 4m_pE_e \tag{2.22}$$

We now define the structure functions F_1 and F_2. In the high Q^2, or Bjorken, limit, $W_{1,2}$ become

$$\nu W_2 \rightarrow F_2(x,Q^2) = \sum_i \epsilon_i^2xf_i(x,Q^2) \tag{2.23}$$

$$m_pW_1 \rightarrow F_1(x,Q^2) = \frac{1}{2x}F_2(x,Q^2) \tag{2.24}$$

where $\nu = (p\cdot q)/m_p$ represents the fraction of energy transferred to the proton in its rest frame, ϵ_i's are the charges of the quarks in the proton, and f_i is the probability that quark i has momentum fraction x of the proton momentum. From (2.8), (2.20), (2.21), (2.22), (2.23) and (2.24), the pure photon exchange cross section is

$$\frac{d\sigma_{EM}}{dxdQ^2} = \frac{2\pi\alpha^2}{xQ^4}\left[1+(1-y)\right]F_2(x,Q^2) \tag{2.25}$$

Two comments are in order here. First, note that in (2.23) F_2 is given as an incoherent sum of probabilities, which is justified for $|\boldsymbol{p}| \gg m_e$, m_p. In this case, time dialation in the proton slows down the interaction of the quarks with each other. That is, during the short time in which the photon interacts with the proton, the quarks are essentially free, allowing the use of an incoherent sum of probabilities. Second, $F_{1,2}$ depend on x and Q^2 where the naive parton model[7] includes only the dependence on x (scaling behavior). This is due to the presence of gluons that are radiated by the quarks or gluons which interact with the photon via a quark exchange. At higher Q^2, more of these gluons are produced, leading to the dependence of the structure functions on Q^2 (i.e., scaling violation).

2.3 Electroweak Interactions

2.3.1 $V - A$ Interactions

Weak interactions violate parity and this changes the "character" of the interactions from that of the electromagnetic interactions. This is seen from interactions that involve neutrinos. We start with Dirac's equation

$$(i\gamma^\mu\partial_\mu - m)\psi = 0 \tag{2.26}$$

which describes spin-1/2 particles. For a massless particle, i.e. a neutrino, we obtain

$$\gamma^\mu\partial_\mu\psi = 0 \tag{2.27}$$

where $\partial_\mu = (\partial/\partial t, \boldsymbol{\nabla})$ and $\gamma^\mu = (\beta, \beta\boldsymbol{\alpha})$ with

$$\boldsymbol{\alpha} = \begin{pmatrix} -\boldsymbol{\sigma} & 0 \\ 0 & \boldsymbol{\sigma} \end{pmatrix} \quad , \quad \beta = \begin{pmatrix} 0 & I \\ I & 0 \end{pmatrix} \tag{2.28}$$

and we are working in the "Weyl" representation. Since $H = \partial/\partial t$ and $\boldsymbol{p} = \boldsymbol{\nabla}$, (2.27) reduces to

$$H\psi = \boldsymbol{\alpha}\cdot\boldsymbol{p}\psi \tag{2.29}$$

leading to the two decoupled equations ($\psi = (\varphi \quad \chi)^T$)

$$E\varphi = -\boldsymbol{\sigma}\cdot\boldsymbol{p}\varphi \tag{2.30}$$

$$E\chi = \boldsymbol{\sigma}\cdot\boldsymbol{p}\chi \tag{2.31}$$

For positive energy solutions, (2.30) describes a left-handed neutrino, ν_L (helicity +1/2). It can also be written in the form of $E\varphi = \boldsymbol{\sigma}\cdot(-\boldsymbol{p})\varphi$ which gives the negative energy solutions. However, with this form, the helicity is opposite and, therefore, gives a right-handed anti-neutrino, $\bar{\nu}_R$. Similarly, (2.31) describes ν_L and ν_R. Under parity operation, (2.30) takes $\nu_L \rightarrow \nu_R$ which violates parity since a ν_R has not been found. Therefore, to select the right helicity state, the electromagnetic *vector* interaction of the form γ^μ is modified to

$$\gamma^\mu\frac{1}{2}(1 - \gamma^5) \tag{2.32}$$

which is a ***vector-axial*** interaction, $V - A$. The interaction (2.32) does pick the right helicity state because

$$\frac{1}{2}(1 - \gamma^5)\psi = \begin{pmatrix} I & 0 \\ 0 & 0 \end{pmatrix}\begin{pmatrix} \varphi \\ \chi \end{pmatrix} = \begin{pmatrix} \varphi \\ 0 \end{pmatrix} \tag{2.33}$$

which selects only ν_R and ν_L.

2.3.2 Charged Current $ep \rightarrow \nu_e X$ DIS

Charged Current reactions involve the exchange of $W^\pm$ particles and are weak interactions. In $e^-p \rightarrow \nu_e X$ (figure 2.2), the outgoing lepton is a neutrino which follows the $V - A$ nature of the neutrino interactions. At the lepton vertex, the current has the form

$$\frac{g}{2}\bar{\psi}_{\nu_e}\gamma_\mu\frac{(1 - \gamma_5)}{2}\psi_e \tag{2.34}$$

where $g/2$ is the weak coupling and is related to Fermi's constant, G_F, by $g^2/8M_W^2 = G_F/\sqrt{2}$. The propagator for the massive exchanged vector boson,

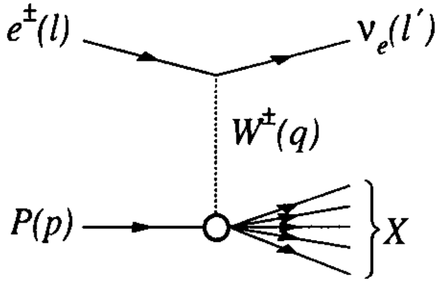

Figure 2.2: $ep \rightarrow \nu X$, $W^{\pm}$ exchange.

$W^{\pm}$, is

$$\frac{-g^{\mu\nu} + q^{\mu}q^{\nu}/M_W^2}{q^2 - M_W^2} \tag{2.35}$$

For the proton vertex, in equation (2.11), W_3 is omitted because electromagnetic interactions respect parity. Weak interactions, however, violate parity and, hence, W_3 has to be included in (2.11) with the antisymmetric tensor, changing equation (2.14) to

$$\begin{aligned} W_{\mu\nu} &= \left(-g_{\mu\nu} + \frac{q_{\mu}q_{\nu}}{q^2}\right) W_1 + \left(p_{\mu} - \frac{p \cdot q}{q^2} q_{\mu}\right) \left(p_{\nu} - \frac{p \cdot q}{q^2} q_{\nu}\right) \frac{W_2}{m_P^2} \\ &\quad - \frac{i}{2m_p^2} \epsilon_{\mu\nu\alpha\beta} p_{\alpha} q_{\beta} W_3 \end{aligned} \tag{2.36}$$

At high energy, or in the Bjorken limit, W_3 becomes

$$\nu W_3 \rightarrow F_3(x, Q^2) \tag{2.37}$$

The leptonic tensor is calculated in the same way as for the electron and is[8]

$$L^{\mu\nu} = 2\left[l^{\mu}l'^{\nu} + l'^{\mu}l^{\nu} - g^{\mu\nu}(l \cdot l') - i\epsilon_{\mu\nu\alpha\beta} l^{\alpha} l'^{\beta}\right] \tag{2.38}$$

This results in the following cross section for $e^- p$ CC interactions:

$$\frac{d\sigma_{CC}}{dxdQ^2} = \frac{\alpha M_W^4 G_F^2}{8\pi} \left(\frac{Q^2}{Q^2 + M_W^2}\right)^2 \left[Y_+ F_2^{CC}(x, Q^2) + Y_- x F_3^{CC}(x, Q^2)\right] \tag{2.39}$$

where $Y_{\pm} = 1 \pm (1 - y)^2$ and M_W is mass of the $W^{\pm}$ boson. The structure functions are given by

$$F_2^{CC} = 2x \sum_i \left[u_i(x, Q^2) + \bar{d}_i(x, Q^2)\right] \tag{2.40}$$

$$F_3^{CC} = 2x \sum_i \left[u_i(x, Q^2) - d_i(x, Q^2)\right] \tag{2.41}$$

where $u_i = (u, c, t)$ and $d_i = (d, s, t)$ represent the u, d, s, c, and t quark momentum distribution functions. If the expressions for $F_{2,3}^{CC}$ are substituted in (2.39), then

$$\frac{d\sigma_{CC}}{dxdQ^2} \sim \sum_i u_i + (1 - y)^2 \sum_i d \tag{2.42}$$

giving a different structure than for the electromagnetic case, (2.25), which is proportional to $\sum_i e_i^2 f_i$ with $f_i = u_i, d_i, ...$etc. This is due to the fact that in electromagnetic scattering, the exchanged photon sees the charge of the quarks and, therefore, F_2 must sum over all the quark distributions weighted by their charges. In weak interactions, there is a universal coupling given by G_F and, therefore, charges of the particles do not enter.

Parity violation plays a major role (recall that only left-handed neutrinos and right-handed antineutrinos exist) as manifested in helicity conservation which is reflected in (2.42). The basic argument[9] is shown in figure 2.3. In the center of mass frame (CM), the electron, e^-, which is left-handed, collides with a left handed quark, u, with total $J_z = 0$, where J_z is the spin projection on the z-axis, taken to be along the direction of the incoming quark. The scattered particles are ν_e and d, both are left-handed. In backward scattering,

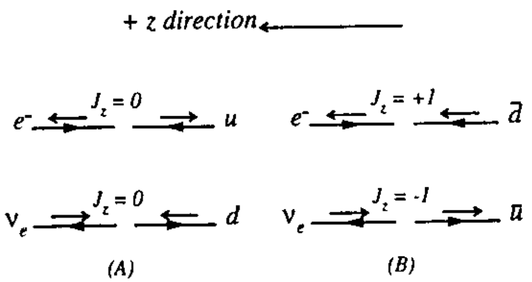

Figure 2.3: Helicity diagrams for electron–quark interactions: (A)e^-, u, d, and ν are left-handed and helicity is conserved, corresponding to the first term of equation (2.42). (B) $\bar{d}$ and $\bar{u}$ are right-handed and helicity is not conserved, corresponding to the second term in (2.42).

(scattering angle = 180°), $J_z = 0$ and helicity is conserved giving rise to the constant term $\sum_i u_i$ in (2.42). However, if the e^- collides with a $\bar{d}$, then $J_z = 1$ since $\bar{d}$ is right-handed. In backward scattering, where the scattered particles are ν_e and $\bar{u}$, then $J_z = -1$ and helicity is not conserved. Therefore, backward scattering is forbidden in CM, resulting in the $(1-y)^2$ term (2.42) which vanishes when $y = 1$, where in CM, $y = 1$ for backward scattering (equation (2.18)).

2.3.3 Neutral Current $ep \to eX$ DIS

NC interactions include both photon and Z^o exchange. The photon exchange reaction is electromagnetic and it has been discussed (section 2.2.1). In this section, only the weak NC interaction involving the Z^o is considered (figure 2.4). One must note that when both photon and Z^o exchanges occur, then this will give rise to interference terms between the photon and the Z^o.

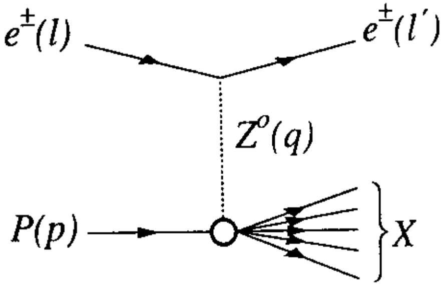

Figure 2.4: $ep \to eX$, Z^o exchange.

CC weak interactions are pure $V-A$ interactions (maximal mixing of vector and axial interactions) and, therefore, are left-handed. However, weak NC interactions are *not* purely $V-A$. The interaction in (2.32) is then changed to

$$\frac{g}{\cos\theta_W}\frac{1}{2}\gamma^\mu(c_v - c_a\gamma^5) \tag{2.43}$$

where the coefficients $c_v = -1/2$ and $c_a \simeq -0.05$ for e^- (they are different for different particles), and θ_W is the weak mixing angle (see section 2.4 below). The fact that $c_a \neq 1/2$ and is small means that parity is not maximally violated, as is the case for CC interactions. It also signifies the existence of a right-handed component in the NC interaction. In the Standard Model, the coefficients are functions of the parameter $\sin^2\theta_W$ which is determined by experiment. The present value of this parameter[10] is $\sin^2\theta_W = 0.225$.

The Z^o propagator is the same as in (2.35) but with M_W replaced by M_Z

$$\frac{-g^{\mu\nu} + q^\mu q^\nu/M_Z^2}{q^2 - M_Z^2} \tag{2.44}$$

The leptonic tensor is

$$L^{\mu\nu} = 2(c_a^2 + c_v^2)\left[l^\mu l'^\nu + l'^\mu l^\nu - g^{\mu\nu}(l \cdot l') - 4ic_a c_v \epsilon_{\mu\nu\alpha\beta} l^\alpha l'^\beta\right] \tag{2.45}$$

The tensor at the proton vertex remains the same as in CC, where W_3 is included to account for parity violation. The cross section, for a pure Z^o exchange, is

$$\frac{d\sigma_{NC_Z}}{dx dQ^2} = \frac{2\pi\alpha^2}{xQ^4}\mathcal{R}^2\left(\frac{Q^2}{Q^2 + M_Z^2}\right)^2\left[(c_a^2 + c_v^2)F^{NC_Z}(x, Q^2) + 2c_a c_v x F_3^{NC_Z}(x, Q^2)\right] \tag{2.46}$$

with $\mathcal{R} = 1/(4\sin^2\theta_W \cos^2\theta_W)$. The structure functions for pure Z^o exchange are

$$F_2^{NC_Z} = x\sum_i \left(c_a^{i2} + c_v^{i2}\right)\left[q_i(x, Q^2) + q_i(x, Q^2)\right] \tag{2.47}$$

$$F_3^{NC_Z} = 2\sum_i c_a^i c_v^i \left[q_i(x, Q^2) - q_i(x, Q^2)\right] \tag{2.48}$$

2.4 Electroweak Unification

The factor $\cos\theta_W$ in (2.43) comes from Glashow-Weinberg-Salam theory of electroweak unification. In this theory, the CC current for W^- emission, is (cf. (2.34))

$$j_\mu^- = \bar{\nu}\gamma_\mu\frac{1}{2}(1 - \gamma_5)\epsilon \equiv \nu_L\gamma_\mu e_L \tag{2.49}$$

where $\epsilon \equiv \psi_e$ and $\nu \equiv \psi_\nu$. The subscript L stands for left-handed. Here we redefine the electron spinor by absorbing the $(1/2)(1 - \gamma_5)$ factor and set $\epsilon_L = (1/2)(1 - \gamma_5)\epsilon$. The neutrino is, of course, left handed.

For W^+ emission, we have

$$j_\mu^+ = \epsilon\gamma_\mu\frac{1}{2}(1 - \gamma_5)\nu \equiv \bar{\epsilon}_L\gamma_\mu\nu_L \tag{2.50}$$

Therefore, we can put ϵ and ν in a doublet

$$\begin{pmatrix} \epsilon \\ \nu \end{pmatrix}_L = \phi_L \Longrightarrow j_\mu^\pm = \bar{\phi}_L\gamma_\mu\sigma_\pm\phi_L \tag{2.51}$$

with $\sigma_\pm \equiv (1/2)(\sigma_1 \pm i\sigma_2)$, where $\sigma_{1,2}$ are Pauli matrices. This resembles the isospin structure of the $SU(2)$ group. To complete the group, we have to construct j_μ^3 by using σ_3. In analogy with (2.49) and (2.50), we have

$$j_\mu^3 = \bar{\phi}_L\gamma_\mu\frac{1}{2}\sigma_3\phi_L = \frac{1}{2}(\bar{\epsilon}_L\gamma_\mu\epsilon - \bar{\nu}_L\gamma_\mu\nu_L) \tag{2.52}$$

Therefore, we have created isotriplet currents belonging to the $SU(2)_L$ group with the currents being j_μ^i, $i = +, -, 3$. The charges of this group are its generators and are given by, along with their commutation relation,

$$I^i = \int j_0^i(x)d^3x \quad , \quad \left[I^i, I^j\right] = i\epsilon_{ijk}I^k \tag{2.53}$$

We would like to identify j_μ^3 with the NC reaction. However, as pointed out in section 2.3.3, NC is not pure $V - A$, i.e. it is not purely left-handed as (2.52) would suggest. Right-handed currents must be included in order to fully characterize NC interactions. For this, we turn to the electromagnetic interaction, which is a NC reaction but with a massless gauge boson. It has both left *and* right components since we can write the electromagnetic current as

$$\bar{\epsilon}\gamma_\mu\epsilon = \bar{\epsilon}_R\gamma_\mu\epsilon_R + \epsilon_L\gamma_\mu\epsilon_L \tag{2.54}$$

where $\epsilon_R \equiv (1/2)(1 + \gamma_5)\epsilon$. Using the charge operator, Q_{em}, the electromagnetic current is $j_\mu^{em} = e\bar{\psi}_e\gamma_\mu Q_{em}\psi_e$. Q_{em} has eigenvalue $= -1$ for the electron.

Since we have Q_{em} and I_3, we use the analogy with the Gell-Mann-Nishijima formula[5] and define the ***weak hypercharge*** Y, belonging to the group $U(1)_Y$, which relates isospin and electromagnetic charge by

$$Q_{em} = I_3 + \frac{1}{2}Y \tag{2.55}$$

with the hypercharge current given as $j^Y_\mu = \bar{\psi}_Y \gamma_\mu \psi_Y$. Therefore

$$j^{em}_\mu = j^3_\mu + \frac{1}{2} j^Y_\mu \tag{2.56}$$

Note that j^3_μ respects $SU(2)$ symmetry by construction and is unchanged by $U(1)_Y$. However, j^Y_μ is constructed so that it is invariant under $SU(2)$ transformations. Therefore, it is a weak isospin singlet. Thus, through (2.56), the electromagnetic and weak interactions are unified, resulting in the group $SU(2)_L \times U(1)_Y$ with both left-handed and right-handed components.

The Z^o current comes from j^3_μ because j^3_μ gives us the W^3_μ field, which is neutral. Since j^3_μ "interacts" with j^Y_μ producing j^{em}_μ, it is expected to interact again with j^Y_μ resulting in j^Z_μ. To find j^Z_μ, we have to turn to the electroweak interaction which is, according to the Standard Model,

$$-i\left[g\boldsymbol{j}\cdot\boldsymbol{W}^\mu + \frac{g'}{2} j^Y_\mu B^\mu\right] \tag{2.57}$$

where g and $g'/2$ are the current couplings to the fields. This form of the interaction is justified by the need for three interacting fields and currents ($W^{\pm,3}_\mu$, $j^{\pm,3}_\mu$). This is given by the first term, which is the form for an $SU(2)$ interaction. Hypercharge is introduced by the current relation in (2.56). Therefore, the hypercharge field which interacts with the the hypercharge current is given by the second term, in analogy with the electromagnetic interaction, $iQ_{em} j^{em}_\mu A^\mu$ (since both belong to $U(1)$ group — see last term of (2.4)). The neutral bosons, Z^o and photon, must come from the neutral fields W^μ_3 and B^μ.

When the Higgs mechanism is invoked,[5] a mass matrix is obtained with two eigenvalues: zero value, the mass of the photon, and a nonzero value which is identified with the Z^o mass. The corresponding normalized orthogonal eigenvectors are

$$\frac{g' W^\mu_3 + g B^\mu}{\sqrt{g^2 + g'^2}} \equiv A^\mu \quad , \quad eigenvalue = M_\gamma = 0 \tag{2.58}$$

$$\frac{g' W^\mu_3 - g B^\mu}{\sqrt{g^2 + g'^2}} \equiv Z^\mu \quad , \quad eigenvalue = M_Z \neq 0 \tag{2.59}$$

The electroweak mixing angle is obtained from the definition (since the fields are normalized)

$$\frac{g'}{\sqrt{g^2 + g'^2}} \equiv \cos\theta_W \tag{2.60}$$

$$\frac{g}{\sqrt{g^2 + g'^2}} \equiv \sin\theta_W \tag{2.61}$$

Examining the third component of the interaction (2.57), we find

$$\begin{aligned} -i\left[g j^3_\mu W^\mu_3 - \frac{g'}{2} j^Y_\mu B^\mu\right] &= -i\left[g\sin\theta_W j^3_\mu + g'\cos\theta_W \frac{j^Y_\mu}{2}\right] A^\mu \\ &\quad -i\left[g\cos\theta_W j^3_\mu - g'\cos\theta_W \frac{j^Y_\mu}{2}\right] Z^\mu \end{aligned} \tag{2.62}$$

where (2.58), (2.59), (2.60), and (2.61) have been used. Because the first term is the electromagnetic interaction, the first term in parenthesis is $\epsilon j^{em}_\mu = \epsilon(j^3_\mu + j^Y_\mu/2)$ resulting in

$$g\sin\theta_W = g'\cos\theta_W = \epsilon \tag{2.63}$$

This yields the result from the Higgs mechanism

$$\frac{M_W}{M_Z} = \cos\theta_W \tag{2.64}$$

Using (2.63) and (2.56), the second term in parenthesis in (2.62) is

$$-i\frac{g}{\cos\theta_W}\left(j^3_\mu - \sin^2\theta_W j^{em}_\mu\right) Z^\mu \equiv -i\frac{g}{\cos\theta_W} j^{NCz}_\mu Z^\mu, \tag{2.65}$$

$$j^{NCz}_\mu \equiv j^3_\mu - \sin^2\theta_W j^{em}_\mu \tag{2.66}$$

Note that the same coupling $g/\cos\theta_W$ also appears in (2.43). As is mentioned in section 2.3.3, c_v and c_a are given in terms of the weak mixing angle. To see this, replace $\sigma_3/2$ by I_3 in (2.52) and note $\bar{\phi} = \phi^\dagger\gamma^0$,

$$\begin{aligned} j^3_\mu &= \bar{\phi}_L\gamma_\mu I_3\phi_L \\ &= \frac{1}{2}(1-\gamma_5)^\dagger\phi^\dagger\gamma_0\gamma_\mu I_3\frac{1}{2}(1-\gamma_5)\phi \\ &= \frac{1}{4}\phi^\dagger\gamma_0\gamma_\mu(1-\gamma_5)(1-\gamma_5)I_3\phi \\ &= \frac{1}{2}\bar{\phi}\gamma_\mu(1-\gamma_5)I_3\phi \end{aligned} \tag{2.67}$$

where the relations $\{\gamma_\mu,\gamma_\nu\} = 2g_{\mu\nu}$ and $\{\gamma_5,\gamma_\mu\} = 0$ are used. We also have $j^{em}_\mu = e\bar{\phi}\gamma_\mu Q_{em}\phi$ (recall that ϕ is given by (2.51); but $Q_{em} = 0$ for ν). Therefore, the second term in parenthesis in (2.62) can be written as

$$-i\frac{g}{\cos\theta_W}\underbrace{\bar{\phi}\gamma_\mu\left[\frac{1}{2}(1-\gamma_5)I_3 - \sin^2\theta_W Q_{em}\right]\phi}_{j^{NCz}_\mu} Z^\mu \tag{2.68}$$

Comparing this with (2.43), c_v and c_a are given by

$$\begin{aligned} c_v &= I_3 - 2\sin^2\theta_W Q_{em} \\ c_a &= I_3 \end{aligned} \tag{2.69}$$

For the electron, $I_3 = -1/2$ and $Q_{em} = -1$ giving $c_v = 0.05$ (using $\sin^2\theta_W = 0.225$) and $c_a = -1/2$ as is given in section 2.3.3.

2.5 Summary of Cross Sections and Kinematics in DIS

The e^-p cross sections are

$$\begin{aligned} \frac{d\sigma_{NC}}{dxdQ^2} &= \frac{2\pi\alpha^2}{xQ^2}\left[Y_+F_2^{NC}(x,Q^2) + Y_-F_3^{NC}(x,Q^2)\right] \\ \frac{d\sigma_{CC}}{dxdQ^2} &= \frac{2\pi\alpha^2}{xQ^2}\mathcal{R}_{CC}\left[Y_+F_2^{CC}(x,Q^2) + Y_-xF_3^{CC}(x,Q^2)\right] \\ \mathcal{R} &= \frac{1}{4\sin^2\theta_W}\left(\frac{Q^2}{Q^2+M_W^2}\right), \end{aligned} \tag{2.70}$$

where the relation

$$M_W^2 G_F = \frac{\sqrt{2}\pi\alpha}{2\sin^2\theta_W} \tag{2.71}$$

is used. The structure functions for NC interaction are[8] (for an unpolarized electron beam)

$$\begin{aligned} F_2^{NC} &= F_2^{EM} - \mathcal{P}F_2^{int} + \mathcal{P}^2(c_v^2 + c_a^2)F_2^{NCz} \\ F_3^{NC} &= -c_a\mathcal{P}F_3^{int} - 2c_vc_a\mathcal{P}^2xF_3^{NCz} \end{aligned} \tag{2.72}$$

where

$$\begin{aligned} F_2^{EM} &= x\sum_i e_i\left[q_i(x,Q^2) + \bar{q}_i(x,Q^2)\right] \\ F_2^{int} &= 2x\sum_i e_ic_vi\left[q_i(x,Q^2) + q_i(x,Q^2)\right] \\ F_2^{NCz} &= x\sum_i(c_v^2i + c_a^2i)\left[q_i(x,Q^2) + q_i(x,Q^2)\right] \\ F_3^{int} &= 2\sum_i e_ic_ai\left[q_i(x,Q^2) - \bar{q}_i(x,Q^2)\right] \\ F_3^{NCz} &= 2\sum_i e_ic_vic_ai\left[q_i(x,Q^2) - \bar{q}_i(x,Q^2)\right] \end{aligned} \tag{2.73}$$

and

$$\mathcal{P} = \frac{1}{4\sin^2\theta_W\cos^2\theta_W}\left(\frac{Q^2}{Q^2+M_Z^2}\right) \tag{2.74}$$

The γZ^o interference terms are given by $F_{2,3}^{int}$. For the CC interaction, the structure functions are given by

$$\begin{aligned} F_2^{CC} &= 2x\sum_i \left[u_i(x,Q^2) + d_i(x,Q^2)\right] \\ F_3^{CC} &= 2\sum_i \left[u_i(x,Q^2) - \bar{d}_i(x,Q^2)\right] \end{aligned} \tag{2.75}$$

For an incoming(scattered) lepton 4–momentum $l(l')$ and an incoming proton 4–momentum p, the kinematical variables x, y, and Q^2 are given in the laboratory frame by

$$\begin{aligned} Q^2 &= -q^2 = -(l-l')^2 = 4E_lE_l'\sin^2\frac{\theta}{2} \\ x &= \frac{Q^2}{2m_p\nu} \\ m_p\nu &= \frac{1}{2}(s-m_p^2) - E_l'E_p(1+\cos\theta) \\ y &= \frac{Q^2}{sx} \end{aligned} \tag{2.76}$$

where θ is the scattered lepton angle and, neglecting electron and proton masses,

$$\begin{aligned} p &= E_p(1,0,0,-1) \\ l &= E_l(1,0,0,1) \\ l' &= E_l'(1,\sin\theta\cos\phi,\sin\theta\sin\phi,\cos\theta) \\ s &= 4E_eE_p \end{aligned} \tag{2.77}$$

At HERA in 1993, $E_e = 26.7\ GeV$ and $E_p = 820\ GeV$, giving a center of mass energy $\sqrt{s} = 296\ GeV$.

Chapter 3

HERA

3.1 General Overview

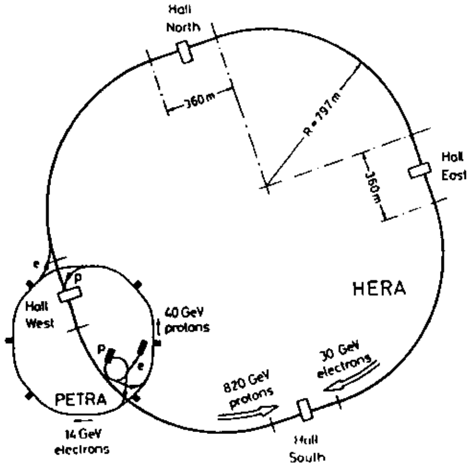

Figure 3.1: HERA collider ring.

HERA,[11] figure 3.1, is the world's only ep collider. It is located at the DESY laboratory, in Hamburg, Germany. The HERA tunnel is located $10m - 25m$

Energy	$E_p = 820\ GeV,\ E_e = 30\ GeV$
Luminosity	$1.5 \times 10^{31} cm^{-2} s^{-1}$
Magnetic Field	Proton ring $4.65T$ Electron Ring $0.165T$
Energy Range	$300 - 1000\ GeV$ protons $10 - 33\ GeV$ electrons
Total Number of Particles	2.1×10^{13} protons 0.8×10^{13} electrons
Number of Bunches	$220^{\dagger}$ for protons and electrons
Time Between Crossings	$96ns$
RF Frequency	$52MHz$ and $208MHz$ for protons $500MHz$ for electrons

†210 filled bunches and 10 empty for background studies

Table 3.1: Some design Parameters for HERA.

under a large park and residential area. HERA has two accelerator rings, electron and proton, that intersect at four collision points. The circumference of each accelerator ring is $6.3km$. The four collision points are sites for the two currently operational collider experiments, ZEUS and H1, and two future fixed target experiments, HERMES and HERA-B. Some of the HERA design parameters are listed in Table 3.1.

3.1.1 Injection Scheme

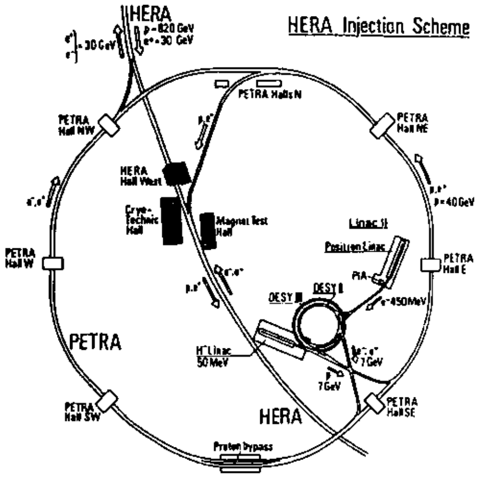

Figure 3.2: HERA injection scheme.

As shown in figure 3.2, the injection begins with LINAC II which accelerates electrons to 500 MeV. These electrons are injected into a small storage ring (PIA) till the current per bunch reaches $60mA$. Once this current is achieved, the bunches are injected into DESY II which accelerates them to 7 GeV before they are sent to PETRA II. This is repeated at $12.5Hz$ until 70 bunches are obtained with $28.8m$ spacing between the bunches, at which point they are accelerated to 14 GeV and then injected to HERA. HERA uses conventional magnets to provide a magnetic field of $0.165T$ for bending electrons. The electrons' energy energy lost by synchrotron radiation is restored by $500MHz$ RF cavities.

Protons are obtained from an H^- ion source and are injected to a linear accelerator that accelerates them to $50 MeV$. Upon entering DESY III, H^- are stripped of electrons and captured into bunches. The protons are accelerated to 7.5 GeV and are injected into PETRA II, in which 70 bunches are collected at 40 GeV before the final injection into HERA. This process is repeated until 220 bunches are stored in HERA.

To maintain 820 GeV protons in their orbit, a bending field of $4.65T$ is required. For such high fields, superconducting magnets are used. Since the proton is about 2000 times more massive than the electron, the energy loss due to synchrotron radiation is $(m_p/m_e)^4 \sim 10^{13}$ times smaller than for electrons. Therefore, this loss is not a problem even at 820 GeV and conventional klystrons and cavities are used, as in the electron case. The RF frequency used at injection is $52 MHz$. However, to sharpen the bunches, the RF frequency is increased to $208 MHz$ at full energy.

The collision of the two beams occurs every $96 ns$ with a zero degree crossing angle, requiring extra bending magnets close to the collision point, thereby generating a large amount of synchrotron radiation from the electron beam. The experiments must be shielded against this radiation.

In 1993, HERA delivered 84 filled electron and proton bunches. 10(6) electron(proton) bunches were left empty for background studies (mainly beam–gas interactions). The integrated luminosity delivered was $\sim 1 pb^{-1}$ with ZEUS collecting $0.54 pb^{-1}$.

Chapter 4

THE ZEUS DETECTOR

4.1 Overview

The ZEUS detector, shown in figure 4.1, consists of several components. Of major importance is the depleted uranium/scintillator calorimeter, which is, for the 1993 run, the principle instrument for particle energy and location measurements. Charged particles are tracked from the interaction point using the vertex detector (VXD) and the central tracking detector (CTD). The backing calorimeter, made of iron plates and proportional tubes, surrounds the calorimeter. Muons are detected by the muon chambers (FMUO, BMUO and RMUO). The Veto Wall is used to veto muons due to proton–gas interaction upstream in the proton beampipe, Finally, the luminosity is measured by the Luminosity Monitor, as described in section 4.5 below. In the following, components relevant to this analysis are described. More details concerning the rest of the components can be found in reference 12.

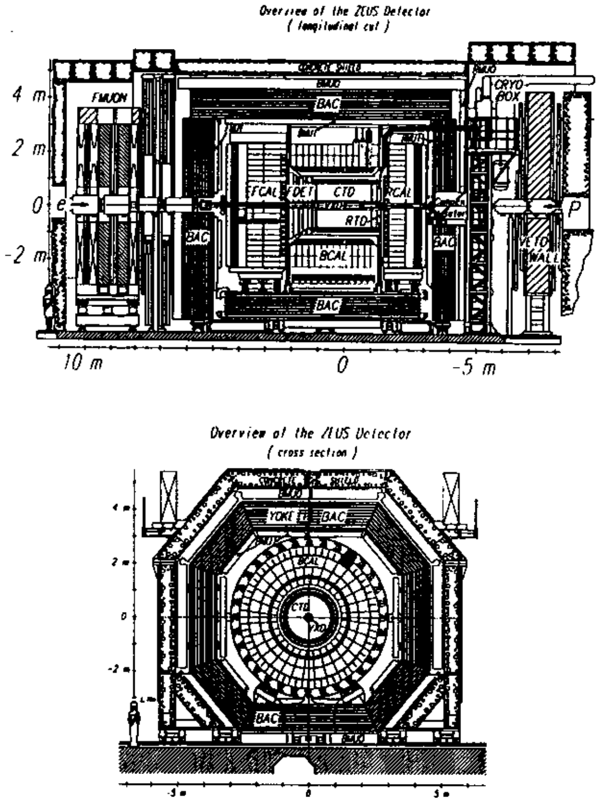

Figure 4.1: *ZEUS Detector: The top diagram shows the xz-projection, where +z is the direction of the incoming proton beam and +x is upward. The bottom figure shows the xy-projection.*

4.2 The ZEUS Calorimeter

The particles produced in an ep interaction usually traverse some detecting, or active, medium in which they deposit all or a fraction of their energy. It is important to measure the energy of these particles as accurately as possible in order to reconstruct the events. The calorimeter is among the several devices that achieve these measurements.

In the calorimeter, particles interact with its material and energy is measured in the form of light that is proportional to the energy of the incoming particle or jet. Not all of the original energy of the incoming particle(s) is detected since the majority of the material in the calorimeter does not produce light. However, the important feature is the fact that the detected light is proportional to the energy of the particles. The proportionality constants can be determined from exposing different sections of the calorimeter to beams of known energy and measuring the response. Using the results of this calibration, the energy of the incoming particles or jets during physics runs can be reconstructed. In addition, calorimeters provide fast signals $\sim 100ns$ permitting fast decisions on event selection, which is very important at the HERA environment since the ep collisions occur every $96ns$ (section 3).

4.2.1 Electromagnetic Showers

At high energies, $e^{\pm}$ lose energy mainly through bremsstrahlung, where the nuclear fields accelerate $e^{\pm}$ which emit photons. In this regime ($E > 1\ GeV$), the energy loss is characterized by X_o, or radiation length, which is the length of material in which an electron deposits about 63% of its energy. The energy,

E, of the electron after traversing a thickness t is

$$E = E_o e^{-t/X_o} \tag{4.1}$$

where E_o is the initial energy of the electron. X_o can be parametrized for $Z > 13$, to 20%, as[13]

$$X_o = 180\frac{A}{Z^2}\left[\frac{g}{cm^2}\right] \tag{4.2}$$

Photons, on the other hand, lose energy mainly by pair creation at energies above 10 MeV.

At lower energies, Bhabha and Møller scattering and ionization losses dominate for electrons. Positrons also suffer annihilation. For energies less than 10 MeV, photons lose energy mainly by the photoelectric effect and Compton scattering. The energy below which all such low energy losses become important is called the ***critical energy***, E_c, and is given by

$$E_c \simeq \frac{550}{Z} \quad [MeV] \tag{4.3}$$

which is correct to 10% for $Z > 13$. Using this formula, we can estimate the maximum length of an electromagnetic shower. On average, after an electron with initial energy E_o passes through a thickness X_o, it radiates a photon. After another X_o, the electron emits another photon, while the initially radiated photon is likely to create an e^-e^+ pair. Therefore, after every X_o, the number of particles increases by about a factor of 2. Then one can see that after a thickness t in the material, in units of X_o, the number of particles produced is 2^t. Assuming the produced particles equally share the energy of the original electron, then the average energy per particle is

$$E_{av} \simeq \frac{E_o}{N_{\gamma e^- e^+}} = \frac{E_o}{2^t} \tag{4.4}$$

where $N_{\gamma e^- e^+}$ is the number of particles. The process of energy degradation per newly produced particle continues on until $E_{av} = E_c$, at which point collision losses become large, terminating the shower in the process, since no more radiation is possible. This occurs at $t = t_{max}$ where

$$E_{av} = E_c = \frac{E_o}{2^{t_{max}}} \rightarrow t_{max} = \frac{\ln(E_o/E_c)}{\ln 2} \tag{4.5}$$

This indicates that the maximum length of an electromagnetic shower increases only logarithmically with energy. Therefore, one can measure low and high energies with a compact calorimeter (the ZEUS calorimeter can measure energies up to 400 GeV). Another useful property that we get from the above argument is that the number of produced particles, N, is directly proportional to the original energy of the incoming particle E_o.

To contain 98% of the electromagnetic shower, the required length of the calorimeter is

$$L_{0.98} \simeq t_{max} + 4\lambda \tag{4.6}$$

where λ is in units of X_o and is given by

$$\lambda \simeq 3.4 \pm 0.5 X_o \tag{4.7}$$

λ gives the length at which the shower decays after it reaches its maximum longitudinal spread. The decay is of the form $e^{-t/\lambda}$ with $4\lambda = 0.4(1.2)$ for electron(photon). For the uranium/scintillator ZEUS calorimeter, $E_c \simeq 10.6$ MeV resulting in $L_{0.98} \simeq 25X_o$.

The electromagnetic shower also develops laterally mainly due to multiple scattering from electrons with energy insufficient for radiation but enough to collide and veer off the shower axis.[14] The relevant length scale is the Molière radius, ρ_M, which is defined to be the average deflection of these electrons. An electron with energy E, after traversing a longitudinal length of X_o, will have ρ_M given by

$$\rho_M = \frac{21X_o}{E_c} \simeq 7\frac{A}{Z} \quad \left[\frac{g}{cm^2}\right] \tag{4.8}$$

95% of the energy of a showering $e^\pm$ is deposited in a cylinder with radius $2\rho_M$. At ZEUS, ρ_M for the electromagnetic calorimeter is $3.3cm$. Therefore, to contain 95% of an electromagnetic shower, the radius needed is $2\rho_M \times 2 = 13.2cm$.

4.2.2 Hadronic Showers

Many interactions occur during the development of hadronic showers. As a result, they are hard to model in detail and one must rely heavily on Monte Carlo-based models and experimental results. Unlike the electromagnetic shower, where most of the energy appears in the form of detectable ionization energy, a hadronic shower loses ~ 50% of its energy in nuclear excitations, breakup of nuclei and evaporation of protons and neutrons.

At energies above 50 MeV, spallation starts, where nuclei are excited and then de-excited through evaporation and emission of protons, neutrons, pions,...etc. These secondary particles are emitted if their kinetic energies are greater than the nuclear binding energy. They are emitted with $< p_t > \simeq 0.35\ GeV$, absorbing ~ 1/2 of the incoming hadronic shower energy.[13] The remainder of the energy is carried off by fast forward-going particles such as pions and nucleons. Photons are also emitted during nuclear de-excitation. Therefore, part of the shower is electromagnetic in character, which is enhanced by the fact that a good proportion of the secondary particles are π^0s

that interact electromagnetically without undergoing nuclear reactions.

Due to binding energies and nuclear breakup, a sizable fraction of available energy is absorbed, leading to a reduction in the signal. In addition, neutrinos leave the calorimeter without being detected, also contributing to signal loss. Muons are minimum ionizing particles and they leave only part of their energies in the calorimeter, further degrading the signal resolution. If uranium is used, then fission starts, especially at higher energies, producing slow neutrons (few MeVs) that carry part of the signal.

The length needed to contain 95% of the shower, including all of the above effects, can be obtained from Monte Carlo studies and experimental results. This length is parametrized as

$$L_{0.95} \simeq 0.2 \ln E + 0.7 + 2.5\lambda E^{0.13} \tag{4.9}$$

where E is in GeV and λ is the absorption length given by

$$\lambda \simeq 35\frac{A^{1/3}}{\rho} \quad [cm] \tag{4.10}$$

where ρ is the density in g/cm^3. For uranium, 300 GeV pions are contained in ~ $80cm$ while 300 GeV electrons are contained in ~ $10cm$. In ZEUS, the depth of the calorimeter is such that containment in excess of 95% is achieved for 90% of jets with maximum energy for high Q^2 events.[12] Also for ZEUS, the hadronic shower has $E_c = 12.3\ MeV$ with $\rho_M = 2cm$.

The structure of the ZEUS calorimeter is described in section 4.3

4.2.3 Sampling, Resolution, and Compensation

In a sampling calorimeter, the active material is sandwiched between two absorber materials. Although this degrades the signal, since only part of the shower is sampled in the active material, this design has the advantage that it ensures shower containment in a compact calorimeter when a dense absorber material is used (e.g. uranium).

Because part of the shower is sampled, the resolution is affected. Other factors also contribute to worsening of the resolution, such as the lateral spread of the shower, nonuniformities due to calorimeter construction and instrumentation, photostatistics (from photomultipliers—PMTs— that collect light and generate electrons). Since the number of particles produced in the calorimeter is proportional to energy, then resolution follows a $1/\sqrt{N} \sim 1/\sqrt{E}$ distribution.

Hadronic showers suffer from greater loss of energy (see above) which affects resolution even more. The figure of merit for the difference in response of the calorimeter to electromagnetic and hadronic showers is the ratio e/h, or the ratio of the response to electrons and hadrons. Due to this greater loss of energy of hadronic showers, $e/h > 1$ which causes nonlinearity to hadronic response. This nonlinearity degrades the energy resolution (more energy smearing) which is important for high energy jets at high Q^2, where events at lower Q^2 can be recontructed at higher Q^2. Using uranium as a passive material helps in compensating for this loss by detecting neutrons resulting from nuclear breakup for two reasons. First, the number of these neutrons is proportional to the binding energy.[15] Second, they are not affected by uranium. In addition, the electromagnetic response caused by hadronic showers must be reduced (to curtail the electromagnetic fluctuations that are nonlinear with energy). Therefore, to achieve maximal compensation, the spacing and thickness of absorber and scintillating materials are tuned so that $e/h = 1$.

Calorimeters that have $e/h = 1$ are referred to as *compensating*. At ZEUS, 3.3mm uranium plate is sandwiched between 2.6mm scintillator. With this configuration, $e/h = 1.0 \pm 0.03$ has been achieved.[16] The resolutions obtained are[12]

$$\begin{aligned} \frac{\sigma(E)}{E} &= \frac{35\%}{\sqrt{E}} \oplus 2\% \quad \mathit{for\ hadrons} \\ \frac{\sigma(E)}{E} &= \frac{18\%}{\sqrt{E}} \oplus 1\% \quad \mathit{for\ electrons} \end{aligned} \qquad (4.11)$$

where the extra 1% and 2% come from nonuniformities in the calorimeter and readout, described above.

4.3 Mechanical Description

The ZEUS calorimeter is divided into three parts with the following angular regions coverage:

-The Forward calorimeter (FCAL): 2.2° – 39.9°.

-The Barrel calorimeter (BCAL) : 36.7° – 129.1°.

-The Rear calorimeter (RCAL) : 128.1° – 176.5°.

Each part is divided into modules with each module, in turn, divided into several towers. Generally, each tower consists of 4 electromagnetic calorimeter (EMC) cells (F/BCAL) or 2 EMC cells (RCAL) and 2 hadronic calorimeter (HAC) cells (F/BCAL) or 1 HAC cell (RCAL) located behind the EMC cells. The exceptions are towers in the FCAL or RCAL region shadowed by BCAL EMCs. In this case, the 4 EMC cells are replaced by a single HAC cell.

Taking the origin at the interaction point and defining the $+z$-direction along the incoming proton beam, FCAL extends from $z = 222cm - 452cm$

and RCAL extends from $z = -148cm$ to $-309cm$. FCAL and RCAL HAC cells are $20 \times 20cm^2$. The FCAL EMCs are $5 \times 20cm^2$ while the RCAL EMCs are $10 \times 20cm^2$. The 23 FCAL and 23 RCAL modules are placed so that the EMC cells face the direction of the interaction point. The depth of an EMC is about $25X_o(\sim 1\lambda)$. The depth of the HAC changes from $\sim 6\lambda$ in the very forward direction to $\sim 3\lambda$ in the rear direction.

BCAL cells are arranged in 32 modules placed parallel to the beam axis. BCAL towers are wedge–shaped with an opening angle of 11.25°. The EMCs are $5cm$ long along the z–direction and the HACs are $20cm$. Each BCAL module has an inner radius $123.2cm$ and an outer radius of $291.2cm$.

The ZEUS calorimeter covers 99.8% of 4π with an angular resolution of $10mrad$. Calibration of the absolute energy scale is better than 1% and event times can be measured to $1ns$. It is constructed from depleted uranium (DU) plates sandwiched between scintillator plates. The depleted uranium is 98.1% ^{238}U, 1.7% Nb, and less than 0.2% ^{235}U, with a density of $18.9g/cm^3$. The scintillator is made of SCSN-38 which has a relatively high light yield and is stable against aging and radiation. The uranium radioactivity insures a stable calibration signal which is used for monitoring over time. DU plates are enclosed in a stainless steel foil of $0.2mm$ thickness in the EMCs and $0.4mm$ in HACs to keep radioactivity emitted low so the resulting PMT dark current is low. At the same time, it is high enough for calibration. The stainless steel foil also protects against contamination.

Wave Length Shifters (WLS) are placed perpendicular to and used to read the light output from the scintillator plates. They are made of polymethyl methacrylate (PMMA) doped with fluorescent dye Y7, with an ultraviolet light absorber for wavelengths less than $360nm$.

4.4 Tracking

The tracking system identifies charged particles and reconstructs their tracks for momentum measurements. It is designed to reconstruct electrons and hadrons with $\sigma(p_t)/p_t < 0.003p_t$ over a wide angular range.

4.4.1 Central Tracking Detector

The Central Tracking Detector (CTD) reconstructs the trajectories of particles within an angular range of 15° – 164°. The active length of the CTD is $2m$, with an outer radius of $85cm$, and is positioned around the Vertex Detector (see below). It is divided into 9 superlayers with each layer containing 8 sense wires. 5 of these layers run parallel to the beam axis and 4 are tilted by a stereo angle of ±5° to make polar and azimuthal angular resolutions approximately equal. In 1993, the CTD was operated with a magnetic field of $1.43T$ using a mixture of Ar:CO_2:C_2H_6 with ratios 90:8:2. The resolutions obtained[17] were $260\mu m$ for $r\phi$ measurements and $4.5cm$ for reconstructing the track z–coordinate.

4.4.2 Vertex Detector

The Vertex Detector (VXD) detects short–lived particles and improves the angular and momentum resolution of particles measured in the CTD. It is a cylindrical drift chamber that covers the angular region from 8.6° – 165°. The VXD has an inner radius of $8.8cm$ and an outer radius of $16.2cm$. It is filled with dymethyl ether with a trace of oxygen and is situated between the beampipe and the CTD. Enclosed within the VXD are 120 drift cells each containing 12 sense wires with 1.6m length parallel to the beam axis. For the 1993 run, the $r\phi$ resolution was 50μm in the center of a cell and 150μm at the edges.[17] Using the hit information from both the VXD and CTD, the track momentum and distance of closest approach improves by a factor of 2–3 when compared to the CTD measurements alone, resulting in momentum resolution for full VXD and CTD reconstructed tracks of[17] $\sigma(p_t)/p_t = 0.005p_t \oplus 0.016$, where p_t is in GeV.

4.5 Luminosity Monitor

The luminosity is measured using the precisely known Bethe–Heitler cross section describing bremsstrahlung, $ep \rightarrow ep\gamma$, at small angle. The Luminosity Monitor detects electrons and photons from this interaction in coincidence. The cross section for this interaction is given by the Bethe–Heitler formula

$$\frac{d\sigma_{BH}}{dk} = 4\alpha r_e^2 \frac{E'}{kE}\left(\frac{E}{E'} + \frac{E'}{E} - \frac{2}{3}\right)\left[\ln\left(\frac{E_p E E'}{m_p m_e k}\right) - \frac{1}{2}\right] \qquad (4.12)$$

where k is the photon energy, $E(E')$ is the incoming(scattered) electron energy, E_p is the incoming proton energy, m_p and m_e are the proton and electron masses, respectively, and r_e is the electron's classical radius.

The Monitor consists of two detectors. The electron detector is located at $z = -35m$ from the interaction point in the direction of the incoming electron beam. It is made of a lead scintillator sampling calorimeter surrounded by lead shielding. It tags electrons with scattering angle less than 0.5$mrad$ and with energies in the range of 14 GeV – 19 GeV. Photons are detected in the photon calorimeter which is located at $z = -106m$. It is made of a carbon filter to absorb synchrotron radiation, a Čerenkov counter to veto electrons coming mainly from photon conversions in the filter, and a photon lead scintillator sampling calorimeter. Photons in the range of 10 GeV – 16 GeV are detected in the Monitor.

Luminosity, $\mathcal{L}$, is related to the bemsstrahlung events rate, R_b, by

$$\mathcal{L} = \frac{R_b}{\sigma_{obs}} \qquad (4.13)$$

Electron–gas interactions have a large cross section which approximately varies like Z^2 . Since this has the same signature as a bremsstrahlung event, it is a significant background which must be subtracted. This rate can be obtained from the electron pilot bunch rate, where the pilot bunch is one that does not have a corresponding proton bunch to collide with. Therefore, the total rate is

$$R_b = R_t - \frac{I_{tot}}{I_{pilot}} R_{pilot} \qquad (4.14)$$

where R_t is the total observed rate, I_{tot} is the total electron current, I_{pilot} is the electron pilot bunch current, and R_{pilot} is the observed rate from the electron pilot bunch. The observed cross section is the Bethe–Heitler cross section folded with the Luminosity Monitor's acceptance, A_{lumi}, and is given by

$$\sigma_{obs} = \int A_{lumi} d\sigma_{BH} \qquad (4.15)$$

As mentioned above, the total integrated luminosity in 1993 was 0.54pb^{-1}. The total systematic error on the measurement was[18] 2.5% which included error in electron–gas subtraction(0.5%), cross section calculation(1.0%), corrections for multiple events(0.05%), counting errors(0.3%), energy scale errors(1.9%), acceptance correction(0.5%), and Monte Carlo statistics(1.0%).

4.6 Backing Calorimeter

The Backing Calorimeter (BAC) surrounds the ZEUS calorimeter. It is designed to include the energy leaking from the calorimeter to improve energy resolution. In addition, it is used to detect muons, from ep interactions and cosmics. The BAC energy resolution is $101\%/\sqrt{E}$.

The iron yoke of the BAC is made of $7.3cm$ plates with $3.7cm$ gaps which are equipped with aluminum proportional tubes filled with 87% Ar and 13% CO_2. Signals are carried by gold plated tungsten wires $50\mu m$ in diameter that are stretched in $15 \times 11mm^2$ cells of an aluminum extrusion.

4.7 Veto Wall

The Veto Wall is located ar $z = -7.5m$. Its is used to detect muons coming from upstream inside the proton beampipe. These muons result from proton–gas interactions.

The Veto Wall is an 800(width)×907(height)×87($thickness$) cm^3 iron wall consisting of 13 layers of iron blocks used as a passive absorber. A rectangular hole with dimensions $-40cm < x < 40cm$ and $-45cm < y < 130.5cm$ is left in the middle of the wall for beam magnets and a vacuum chamber. Two scintillator hodoscope arrays are also present on both sides of the wall, with each array consisting of 48 scintillator counters.

4.8 C5 Counter

Beam–gas interactions are significant background in HERA, especially from protons. To reduce the beam–gas rate, the C5 counter is used. It consists of four $2.6mm$ thick scintillator counters surrounding the beampipe and located behind the RCAL at $z = -315cm$. These counters are at about $5cm$ distance from the beam. Each pair of counters is used in coincidence to detect beam–gas interactions. The C5 Counter measures both the times and energies of the detected particles.

The characteristic time of a beam–gas event is different from an ep event. When a proton in the beampipe collides with a gas particle, the scattered particles arrive at the RCAL earlier than those particles originating from an ep collision (in this case, the proton has to traverse an extra distance to the interaction point making the scattered particles arrive at the RCAL at later times). From such timing information, the background rate is reduced by an order of magnitude. [29]

Chapter 5

TRIGGER AND READOUT

5.1 Layout

The main trigger backgrounds in HERA are beam-gas interactions ($\sim 100kHz$), cosmics ($\sim 1kHz$), and electronics noise ($\sim 0.1kHz$). The goal of the trigger is to reduce this background efficiently while identifying the "interesting" physics events. The readout, on the other hand, has to measure the energy deposits and their times accurately to reconstruct these events. Because the time between crossings is $96ns$, it is very difficult to make a decision to keep an event within such a short time. To overcome this, both the trigger and readout are designed as pipelines. The trigger pipeline performs the necessary calculations and distributes the decision to the readout in $\sim 5\mu s$, while accepting events every $96ns$, avoiding any deadtime in the process. The readout keeps the event information in buffers until it receives a trigger decision while still accepting events every $96ns$. The data acquisition system is shown schematically in figure 5.1.

ZEUS uses a three level trigger. At the first level, the rate is reduced to below $1kHz$ by using programmable dedicated logic circuits. The results of each detector component are sent to the Global First Level Trigger (GFLT)

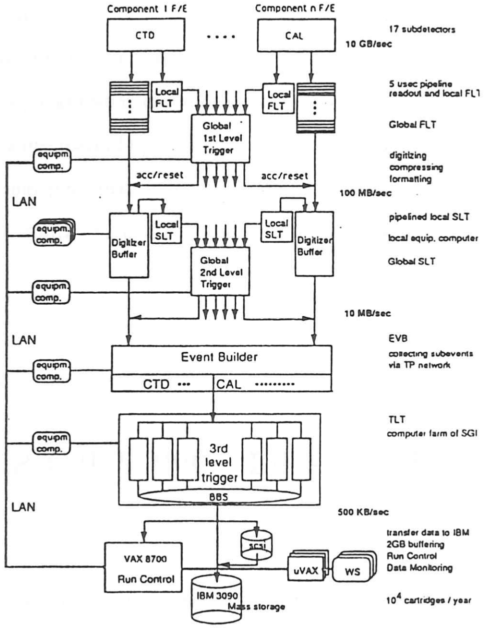

Figure 5.1: *ZEUS Data Acquisition chain.*

within 26 crossings. The GFLT takes 20 more crossings before sending a decision ("level 1 accept") for the component readouts to read the event, that is, digitize and send the event to the Second Level Trigger (SLT). Therefore, the trigger takes a total of 46 crossings, or $4.4\mu s$ before issuing an accept. The Calorimeter First Level Trigger (CFLT) has, in addition, the Fast Clear[19] which runs hardware cluster finding algorithms on the CFLT data. It can abort events before initial data processing by the SLT. The CFLT/Fast Clear design goal is to reduce the input rate to the SLT to below $1kHz$.

After the GFLT decision, the component SLT, which is software based, processes digitized data, enabling more precise calculations. The results of these calculations are sent to the Global Second Level Trigger[20] (GSLT) which combines the information of all components and reduces event rate to less than $100Hz$. A positive decision from the GSLT is fanned out to the components via the Event Builder.[21] The components then send their data to the Event Builder which formats them into ADAMO structure[22] before transmitting them to the Third Level Trigger[23] (TLT). The TLT is a Silicon Graphics computer farm (6 VME crates with each crate connected to 6 computers). It runs a simplified version of the offline reconstruction code to reduce the event rate to $5Hz$ ($500k$Bytes/s). The results of the TLT processes are sent to mass storage devices or to the central online computer for online monitoring.

5.2 ZEUS Calorimeter Readout

The ZEUS calorimeter readout[24,25] shapes, amplifies, and samples the signal at a rate of $10MHz$. It is a $5\mu s$ deep pipeline that reconstructs energy and time of the events, measures the level of noise from the radioactive depleted uranium, and sends 5% of the charge on each channel to the CFLT (see below).

The ZEUS calorimeter data acquisition chain starts with the Analog Cards of the readout, which are placed on the calorimeter. They are pipelined and each card reads 12 PMTs. They provide 17 bits of pulseheight dynamic range (up to 400 GeV) and times of energy deposits accurate to $1ns$, which are for vetoing beam-gas interactions. The 12 PMT signals are integrated and shaped before being sampled every $96ns$. The samples are stored in an analog pipeline until a receipt of a level 1 accept. If there is no such trigger, they are discarded. Once triggered, these samples are sent via $60m$ twisted pair cables to the Digital Cards, located in the electronics house (ruck sack).

The Digital Cards digitize the samples, correct for gain and pedestal errors, and calculate the energy and time. Signals from 24 PMTs are handled by one Digital Card. The result of these calculations are sent to the calorimeter SLT.

The SLT[26] is a 3-layer transputer processor network that interfaces with the Digital Cards. To cut on time dedicated for events, each transputer processes data from several neighboring calorimeter cells, in parallel with other transputers. The SLT monitors the calorimeter continuously and also controls the readout electronics. It identifies electron and hadron clusters and sparks. It also calculates the times of the energy deposits. The results are sent to the GSLT.

5.3 ZEUS Calorimeter First Level Trigger

5.3.1 Rates and Goals

The CFLT[27] task is to identify NC (characterized by low P_t and an isolated electron in the final state), CC (high missing $P_{t_{miss}}$), photoproduction and low x events (typically low energies), and exotic events (leptoquarks, excited fermions,...etc, that have high missing $P_{t_{miss}}$, or isolated electron/muon in the final state). This interesting physics comes at a rate of few Hz which has to be extracted from a background made of beam-gas interactions ($\sim 100kHz$)and cosmic and beam muons (few 100s Hz). The goal is to cut the background rate to below $1kHz$ while maintaining high efficiency for physics events.

5.3.2 Data Flow

A typical calorimeter trigger tower consists of 1 (F/BCAL) or 2 (RCAL) EMC cells and 2 (F/BCAL) or one (RCAL) HAC cells that lie most projectively behind the EMC towers. The collection of the EMC cells or HAC cells of a tower is called an EMC, or HAC, section. As is mentioned in section 4.3, some of the F/RCAL cells are shadowed from the interaction point by BCAL. A particle that scatters to these cells will first hit a BCAL EMC cell, BCAL HAC cell, then the shadowed cell. For this reason, these shadowed cells are used as HAC cells and are combined, through cabling, with the BCAL HAC cells to make the geometry as projective as possible. Therefore, the CFLT treats the shadowed cells as part of the BCAL. Using a combination of cables and electronics assignments, the calorimeter is divided into 896 trigger towers (figure 5.2(A)) that are further subdivided into 16 regions (4 FCAL, 8 BCAL, and 4 RCAL — figure 5.2(B)), each region being an 8 × 7, or 56, CFLT tower region. Each region is served by one CFLT VME crate in the electronics house. Each VME crate is custom made with a standard VME J1 and custom J2 and J3 backplanes. The J2 and J3 buses are split in the middle.

Trigger Sum Card

Typically, each Analog Card reads 12 PMTs. The "left" Analog Card reads 6 PMTs from the "left" side of a tower and 6 PMTs from the left side of another tower. The "right" Analog Card does the same but with the right sides of the two towers (figure 5.3). The Analog Card sends 5% of the charge in sums of up to 6 PMT signals from one tower to the Trigger Sum Card (TSC), the first element in the CFLT chain. Like the Analog Cards, the TSCs are also

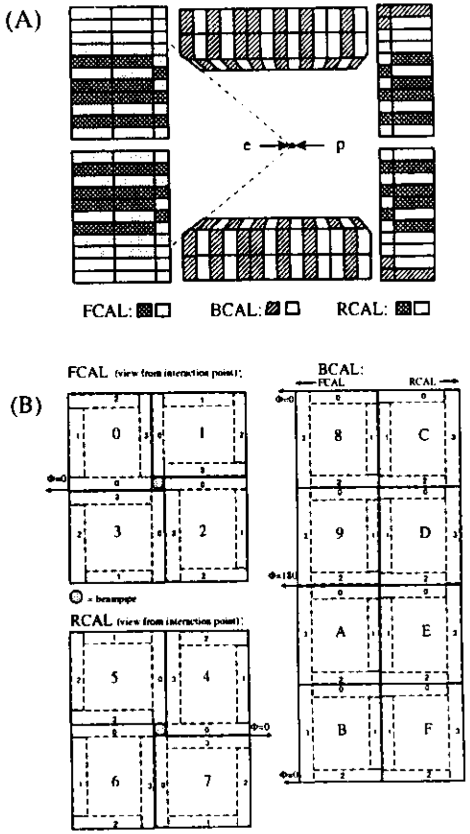

Figure 5.2: *Figure(A): Trigger Tower arrangement. Figure(B): Trigger region assignments of the calorimeter (0–F) with edge regions shown.*

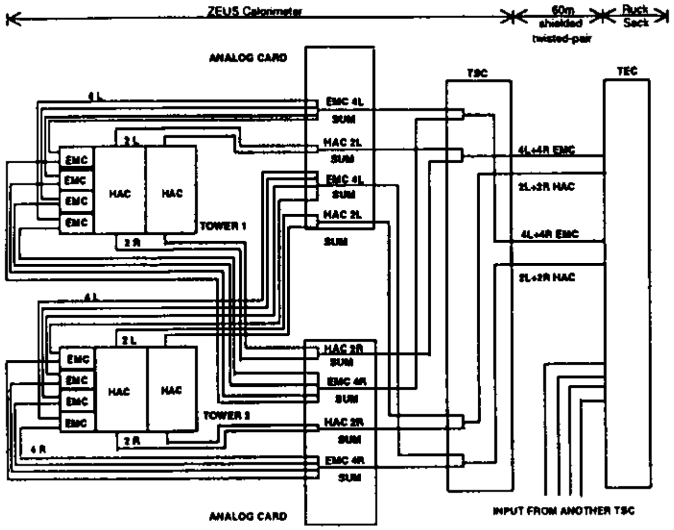

Figure 5.3: *Summation scheme of Analog and Trigger Sum Cards. L stands for left and R for right. TEC is the Trigger Encoder Card (see section 5.3.2).*

mounted on the calorimeter.

The TSC has 8 inputs, 4 for left PMTs and 4 for right PMTs. Each left/right input pair is integrated and summed with 12-bit dynamic range. The baseline is restored every $96ns$. The resulting signal is then shaped and sent by a $60m$ shielded twisted-pair cable to the Trigger Encoder Card (TEC), located in the electronics house.

PMT gains are set such that 1 GeV of energy produces $3.65pC$ of charge on each of the 2 PMTs attached to an FCAL cell. For B/RCAL, the gain is $5.30pC/GeV$. When left and right PMTs are summed, the total charge per GeV of energy is either $7.3pC$ (FCAL) or $10.6pC$ (B/RCAL). 5% of this charge is sent to the TSC. In FCAL, the maximum deposited energy is 400 GeV. In B/RCAL, it is 100 GeV. Therefore, the maximum charge delivered to each TSC is $400\ GeV \times 7.3pC/GeV \times 0.05 = 146pC$ for FCAL and $100\ GeV \times 10.6pC/GeV \times 0.05 = 53pC$ for B/RCAL. For FCAL cells shadowed by BCAL, although summed with BCAL HAC cells, the TSC gain is set for the maximum deposited energy of 400 GeV, resulting in a maximum charge of $400\ GeV \times 10.6pC/GeV \times 0.05 = 212pC$. The TSC maximum driving voltage on its output is $2V$. Therefore, the TSC gains are set to $13.7mV/pC$ for FCAL, $37.7mV/pC$ for B/RCAL, and $9.4mV/pC$ for FCAL cells summed with BCAL HAC cells.

Each individual TSC input is controlled by serial data via fanouts located on the detector. This flexibility allows individual left or right inputs to be shut off when they become noisy. Calibration compensates for this at the Trigger Encoder Card (see below) level by applying a multiplicative factor to the charge to energy conversions of the remaining active inputs. In addition, the fanouts can be used to set thresholds used in detecting sparks through differences in left and right pulseheights. There are ~ 5000 TSC input channels on the calorimeter controlled by 130 fanouts.

Trigger Encoder Card

The Trigger Encoder Cards (TECs—figure 5.4) are located in the CFLT crates in the electronics house. There are 14 TECs per each of the 16 trigger crates covering a 8 × 7 trigger region (56 towers). Therefore, there are 224 TECs in

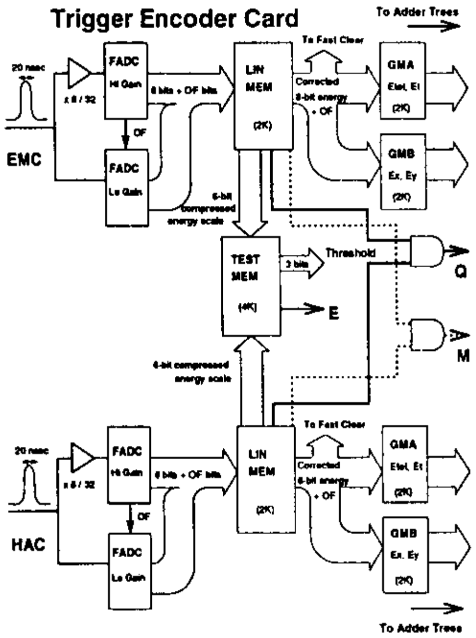

Figure 5.4: *TEC Schematic for Front End, Linearization, and Tests.*

the system, giving a total of 1792 channels (896 low gain and 896 high gain channels). Each TEC receives signals for up to 4 EMC and 4 HAC sections from TSCs. The TEC is a 370 × 400mm^2 13-layer printed circuit board with 8700 *vias*, and 1100 components that occupy 75% of the board area. It provides a dynamic range of 0 – 400 GeV.

The analog pulse, with 80ns width and 20ns flat top, is digitized, after being pedestal corrected, by two 8-bit Flash Analog to Digital Converters (FADCs), in low and high gain channels. In the high gain channel, the signal

is multiplied by 8 (B/RCAL) or 32 (FCAL). The pedestals are set by two Digital to Analog Converters (DACs), one for the low gain channel and one for the high gain channel. The noise in the system is less than 4 counts on any individual high gain channel.

Each FADC (low and high gain) is clocked by a 96ns clock whose phase is adjusted by a delay line in order to digitize the midpoint of the flat top of the incoming pulse. The digitized signal is then sent to a register that synchronizes the data with the GFLT 96ns clock that drives the whole system.

The digitized data, along with the high/low gain overflow bits, are received by a 2-page programmable Linearization Memory. Its first page corrects the data for calibration and places the corrected data on one of two 8-bit scales, low and high gain (determined by the FADC high gain overflow bit). In the high gain channel, the full scale energy is $E_{max} = 12.5\ GeV$ while it is 400 GeV(100 GeV) in the low gain channel for FCAL(B/RCAL), yielding a gain of 32(8). The resulting resolution is $E_{max}/2^8 = E_{max}/256$. The high gain scale resolution is then 49 MeV/bit, while the low scale resolution is 1.6 GeV/bit in the FCAL and 390 MeV/bit in B/RCAL. Energies below 464 MeV are set to zero

The second page contains 8-bit words that include one "Q"(or Quiet) bit, indicating a section (HAC or EMC) with energy less than that of a minimum ionizing particle (MIP), one "M" bit for an energy consistent with a MIP, and 6 bits of energy placed on a nonlinear (compressed) scale between minimum ionizing and maximum scale. The maximum value of 63 of these 6 bits is reserved for the low gain overflow.

The Linearization Memory sends its 8 bits of data from the first page, along

	Threshold number							
	0	1	2	3	4	5	6	7
Threshold bit representation	000	001	010	011	100	101	110	111
Tower Energy > (GeV)	-	1.25	2.5	5.0	10.0	20.0	40.0	overflow

Table 5.1: *Threshold bits used for tests by the TEC.*

with the high gain overflow bit, to two 2–page programmable Geometric Memories, GMA and GMB. GMA calculates E_{tot} (first page) and $E_t = E_{tot}\sin\theta$ (second page), while the GMB finds $E_x = E_{tot}\sin\theta\cos\phi$ (first page) and $E_y = E_{tot}\sin\theta\sin\phi$ (second page). E_{tot} values are set for all channels at $100\ GeV/256 = 1.6\ GeV/\text{bit}$. E_t values for all channels are placed at a scale of $75\ GeV/256 = 0.29\ GeV/\text{bit}$, where $E_{t_{max}} = 75\ GeV$. E_x and E_y are signed quantities ranging from $-75\ GeV$ to $75\ GeV$ and are expressed in 2's–complement notation at a scale of $75\ GeV/2^7 = 75\ GeV/128 = 0.58\ GeV/\text{bit}$.

It takes $96ns$ to send these quantities to the adder trees. During the first $18ns$, E_{tot} and E_x are presented to their respective adder trees. In the second $18ns$, E_t and E_y are presented (E_t and E_y go through the *same* trees as E_{tot} and E_x, respectively). There are two trees for EMC and two for HAC. The results of the adder trees are sent to the Adder Card via modified J2 and J3 split backplanes at $12ns$ rate.

The test circuitry uses the Q, M, and the 6 bits of compressed scale energy from the EMC and HAC sections of each tower. The sum of the HAC and EMC energies is tested against 6 energy thresholds. The result of this comparison is given as three programmable threshold bits whose definition is shown in table 5.1. In addition, an "E" bit is reported if the tower is consistent with electromagnetic energy. This bit is determined by a programmable function of six bits a piece of EMC and HAC energy. The EMC Q bit is ANDed with the HAC Q bit. The same is done with the M bit. The resulting 6 bits (3 threshold bits, E bit, Q bit, and M bit) are multiplexed to three bus lines on modified J2 and J3 split backplanes at a $12ns$ rate.

Trigger Adder Card

There are two Trigger Adder Cards (TACs) per CFLT crate (a total of 32 in the system). One is on the left of the split of the J2 and J3 backplane and one on the right. Each receives data from 7 TECs. One TAC is designated as the "Master" and the other is the "Slave" (no connection to the corresponding VME terms). The two TACs communicate with each other via a bi–directional front panel printed circuit board.

The TACs continue the energy summation of the TECs which send E_{tot}, E_t, E_x, E_y, and the overflow bit. The summation is done with 8 bits of dynamic range. The Master card combines the information from the two TACs and sends energies and the overflow (ORed with the carry bit) via cables to the CFLT Processor (CFLTP).

Energies in subregions within the 8×7 tower region, served by one crate, are also calculated. These subregions are programmable and up to 8 subregions can be defined. This is essential for regions in the calorimeter that span more than one trigger crate. For example, specific trigger towers in the 4 RCAL regions served by 4 crates are assigned to the RCAL beampipe area. Energies found from the threshold test bits of the TECs for these towers are summed up by their respective TACs of that crate. The results are then sent to the CFLTP which finds the total beampipe subregional energy sums by summing the results of the 4 crates.

The number of towers in a 56 tower trigger region exceeding each threshold, but not the one above it, are histogrammed. This is used to search for jet candidates in which energy deposition is contained in a few towers.

Isolated electrons and muons are found by the TACs. It is important to do such a search at the first level trigger for four reasons. First, no Q^2 cut is needed to find electrons. Second, the background coming from hadrons faking an electron, by passing at an angle from an EMC cell of one tower to a HAC cell of *another* tower, is reduced. Third, muons can indicate the production of heavy quarks, decay of heavy leptons, or production of gauge boson. Fourth, the muon trigger background rate is reduced when the CFLT muon trigger is combined with the muon triggers of the muon detectors.

The TACs use E and Q bits to find electrons (for muons, the M bit is used) by searching for a pattern consistent with an isolated electron (7 patterns are considered in the hardware[28]). One such pattern is shown in figure 5.5. The pattern logic starts with seven overlapping 2 × 2 trigger tower regions across the top of the 56 tower region in parallel. In each 4 × 4 region, of the 8 × 7 tower region, the pattern logic searches the central 1–4 (2 × 2) towers with an electromagnetic signal (E bit). It then checks the surrounding (up to 12) towers to be quiet. It takes $12ns$ to identify a pattern in the 2×2 region and two cycles of $12ns$ for the remaining 12 towers surrounding it (to complete the 4 × 4 region). However, when the search in the 12 surrounding towers begins

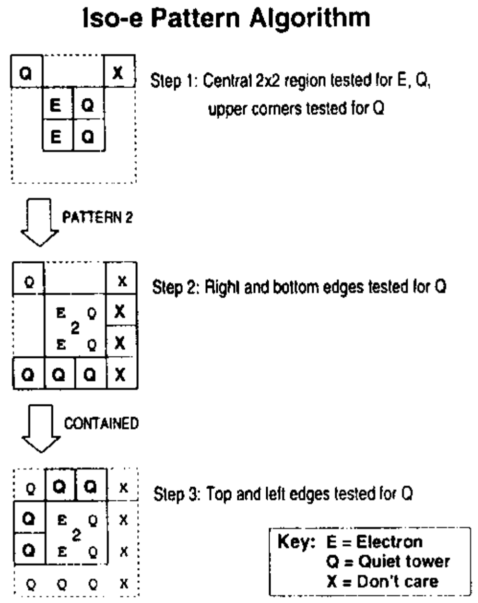

Figure 5.5: *The three step algorithm to identify isolated electrons by the TACs.*

at the next $12ns$ step, a new 2×2 search starts with towers in the 8×7 tower region that are one row below. In total, it takes nine $12ns$ cycles to analyze a 56 tower region for contained and edge leptons (edge leptons are found at the edges of an 8×7 region. Their isolation is confirmed by the CFLTP).

CFLT Processor

The CFLTP gets information from all 16 CFLT crates and produces global and regional trigger quantities which it transmits to the GFLT. It receives the number of contained and edge leptons and verifies isolation for the edge leptons. It continues the process of energy summation of the TECs and calculates regional and global E_{tot}, E_x, E_y, $E_{miss} = \sqrt{E_x^2 + E_y^2}$, and total missing electromagnetic energy. The transverse energies of HAC and EMC calorimeter sections and missing transverse EMC energy are compared against programmable thresholds. Sums of energies in FCAL beampipe and RCAL beampipe are also calculated. The results of this summation are sent in 32 16-bit words to the GFLT (table 5.2).

The hardware of the CFLTP consists of 8 Input Cards (ICs), one Communications Card (CommC), and 10 Algorithm Cards (ACs). Each IC gets data from TACs in 2 crates at 128bits/24ns and sends data at 48ns rate to the ACs. Each AC executes a different algorithm and receives different subsets of the data through the backplane from the ICs for the appropriate calculations.

The CommC receives and distributes clocks and control signals from the GFLT. From the GFLT 96ns clock, it creates the 12ns clock for the TACs and the 48ns clock for the ICs and ACs. The CFLT control signals and the 12ns and 96ns clocks are fanned out to the TACs through the Adder Support Module. The 96ns clock can also be generated by the CommC for standalone testing. The delays on the various clocks are independently adjusted by software.

5.3.3 Calibration

The CFLT is calibrated using charge injectors that mimic both the pulse size and time structure of real physics data. The precision of the charge injectors is known to within 1%. These injectors are controlled by the calorimeter readout,

Regional Quantities ×16		Global Quantities	
Pattern Logic			
Isolated ϵ	2 bits	Isolated ϵ	1 bits
Isolated μ	2 bits	Isolated μ	1 bits
8-bit resolution adders, full scale 50 GeV or 75 GeV			
E_{tot}^{EMC}	3 bits	E_{tot}^{EMC}, E_t^{EMC}	8 bit ×2
E_t	3 bits	E_t	8 bits
		E_{tot}	8 bits
		$\|E_{tmiss}\|$, angle	8 bits ×2
		$\|E_{tmiss}^{EMC}\|$	7 bits + sign
		E_x, E_y	7 bits + sign ×2
		E_{tot}^{FCAL}	8 bits
		E_{EMC}^{RCAL}, E_{HAC}^{RCAL}	8 bits ×2
		$(E_{EMC}/E_{HAC})_{RCAL}$	1 bits
		E_{EMC}^{BCAL}	3 bits
Quantities based on 3-bit comparisons, "Threshold Sums"			
Quiet Region	1 bit	BCAL Towers > $E_{Thr}^{\dagger}$	8 bits
		$E_{F/RCAL}$ outside bp‡	8 bits ×2
$E_{F/RCAL}$ in bp	3 bits ×8	$E_{F/RCAL}$ bp	8 bits ×2
Electronic OF*	1 bit	Any RCAL Tower > KL§	1 bit
Jet Likelihood	3 bits	Global Jet Likelihood	8 bits

†Thr = Threshold, ‡bp = Beampipe

§KL = Kinematic Limit, *OF = Overflow

Table 5.2: *Quantities available from the CFLT (every 96ns).*

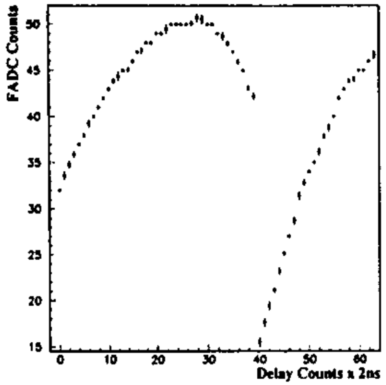

Figure 5.6: *Time evolution of a typical pulse charge injector pulse profile at the FADC on the TEC. Vertical bars are root mean square errors arising from sampling each point 10 times. Note that the pulse rises again after the peak is reached. This is because the next edge of the 96ns clock is starting to digitize (next crossing).*

which is interfaced to the CFLT by a 2TP-VME[26] module located in one of the readout crates. This module, which is part of the CFLT crate system, is used to send control signals to fire the charge injectors at a certain pulse height (set by a DAC on the Analog Card) and time.

If the pulse heights are set at some fixed voltage, then by varying the clock delay line of the TEC for every *individual* FADC, one can obtain a pulse height–time profile at the FADC (which is accessed by reading the digitized data from the TEC Linearization Memory). Figure 5.6 shows a typical pulse profile. This type of information is used to find bad channels in the calorimeter.

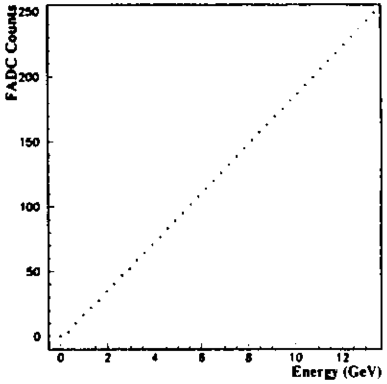

Figure 5.7: *A linearity profile for one of the high gain channels. The Error bar on each point is too small to be seen. Note that the first point deviates a little from a straight line. This point is the pedestal setting of the channel.*

Any channel that reports a pulse height different by 10% from expectation is flagged as a bad channel and later fixed. It is also be used to find bad clock delay lines (since in this case the pulse profile will either be digitized at an "abnormal" delay setting of the delay line or will have a different time structure from that expected, shown in figure 5.6). In addition, such profiles are used to obtain the setting of *each* FADC delay line needed to digitize the middle of the pulse flat top.

If the FADC clock delays are set so that the FADCs always digitize at the pulse flat top, then by changing the Analog Card DAC setting, so that the pulse height is changed, and reading the FADC data after the pulse is digitized, one can check the linearity of the analog part of the CFLT. Such linearity profiles, an example of which is shown in figure 5.7, give the maximum low and high gain pedestal corrected scales (ideally, gain of 1 for the low gain channel, and gain of 32(8) for high gain channel in the FCAL(R/BCAL)). These gains constitute the calibration constants, which are stored in the Linearization Memories in the form of multiplicative factors. During 1993, these multiplicative factors were set to unity. The calibration procedure was first implemented during the 1994 run.

5.3.4 Trigger Conditions and Performance in 1993

Trigger Quantities

The principle algorithm used in 1993 to reduce $\sim 100kHz$ of background rate, while retaining high efficiency for NC and CC events, is an OR of energy threshold requirements on several trigger quantities (table 5.3). Not all the CFLT quantities listed in table 5.2 are used since the luminosity in 1993 was about 5% the design luminosity.

The REMCthr (E^{RCAL}_{EMCThr}) trigger shown in table 5.3 uses the three energy threshold bits of the TECs to find electrons. The isolated electron trigger was first implemented in 1994.

Rates and Efficiencies

In 1993, the total CFLT rate was $75Hz$ from a total background rate of $\sim 100kHz$, at a HERA luminosity of 0.7×10^{30}. The efficiency of each trigger has been studied with the CFLT triggers collected by GFLT. To obtain the efficiency of E^{BCAL}_{EMC}, for example, one obtains the E^{BCAL}_{EMC} energy spectrum

$E_{tot} \geq 15\ GeV$	OR
$E_t \geq 11.5\ GeV$	OR
$E^{EMC}_{tot} \geq 10\ GeV$	OR
$E^{BCAL}_{EMC} \geq 3.4\ GeV$	OR
$E^{RCAL}_{EMC} - \mathrm{bp}^{\dagger} \geq 2\ GeV$	OR
$E^{RCAL}_{EMCthr} \geq 3.75\ GeV$	

†bp = Beampipe.

Table 5.3: *Threshold requirements on CFLT quantities for 1993.*

of data triggered by other quantities irrespective of whether E^{BCAL}_{EMC} trigger tagged the events. Another E^{BCAL}_{EMC} energy spectrum is obtained but with the requirement that all the events are also tagged with the E^{BCAL}_{EMC} trigger. Dividing this spectrum by the previous spectrum results in an efficiency curve. To correct for the CFLT acceptance, we use a E^{BCAL}_{EMC} spectrum for Monte Carlo data that passed through the CFLT simulation. Multiplying this spectrum by the efficiency curve and integrating the result gives the total efficiency of the E^{EMC}_{BCAL} trigger.

The overall CFLT efficiency for NC events is 98% and for CC events 85%. The REMCthr trigger has been the most efficient trigger for NC, where more than 92% of the ZEUS NC sample has been tagged by this trigger with 49% of it being collected exclusively by this trigger. The purity of the REMCthr trigger is low with 95% of it being rejected at the SLT as originating from beam–gas interactions.

The REMCthr rate was estimated to be too large for the 1994 run, where the luminosity was 5 times that of 1993. As a result, the isolated electron trigger was studied in 1993 to find the best algorithm needed for the 1994 run. As discussed above, the isolated electron algorithm searches for towers with electromagnetic (E) bits surrounded by quiet towers (Q bit). An EMC(HAC) tower is quiet if its energy is less than some programmable threshold, $Q_{emc}(Q_{hac})$. The E bit is based on a programmable function. The algorithm chosen is $Q_{emc} = 2.52\,GeV$, so the trigger has 100% efficiency (including energy sharing between towers) for electron energy $> 5\,GeV$, $Q_{hac} = 0.95\,GeV$, and E = [(EMC $\geq Q_{emc}$) AND (HAC $\leq Q_{hac}$)] OR [(EMC $\geq Q_{emc}$) AND (EMC/HAC $\geq$ 3)]. With this configuration, the rate is reduced by a factor of 2 with respect to the REMCthr trigger (figure 5.8(A)) while maintaining the same efficiency as the REMCthr trigger for NC events. The overall efficiency of the isolated electron trigger relative to a standard ZEUS software electron finder is 98% (figure 5.8(B)).

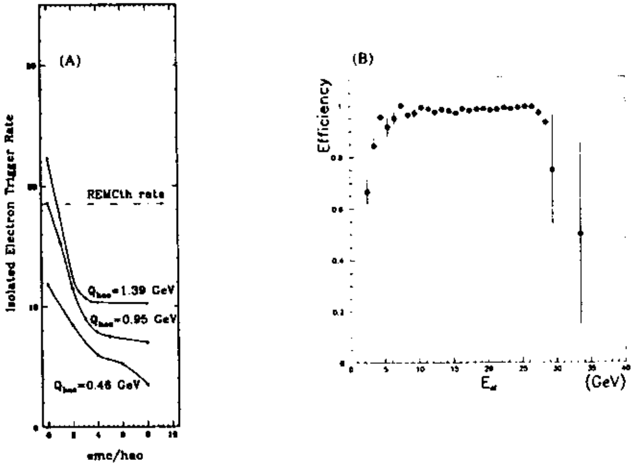

Figure 5.8: *Figure (A): The isolated electron trigger beam-gas background in arbitrary units as a function of Q_{hac} and EMC/HAC parameters. The dot-dashed line indicates the rate of the REMCthr trigger at* 3.75 *GeV. Figure (B): The isolated electron trigger efficiency relative to a standard ZEUS electron finder versus electron energy. The efficiency rises between E_{el} 2.5 and* 5 *GeV due to events where the electron energy is shared between trigger towers (Q_{emc} =* 2.52 *GeV). Events with $E_{el} \geq$* 30 *GeV are not electrons since they are outside the kinematic limit.*

Chapter 6

KINEMATIC RECONSTRUCTION AND MONTE CARLO SIMULATION

6.1 Kinematic Reconstruction

The kinematic variables x, y, and Q^2 can be reconstructed using a variety of methods with combinations of the scattered lepton and quark jet energies and angles.[30] One chooses the method giving the best average resolution and smallest kinematic biases. The kinematic variables, given in equations (2.12) and (2.17), are

$$\begin{aligned} Q^2 &= -q^2 = -(l - l')^2 \\ x &= \frac{Q^2}{p \cdot q} \\ y &= \frac{p \cdot q}{p \cdot l} \end{aligned} \tag{6.1}$$

where $l(l')$ is the incoming(scattered) lepton 4-momentum and p is the incoming proton 4-momentum.

Three methods for kinematic reconstruction are considered in this analysis:

1. The electron method: The kinematic variables are reconstructed from the scattered electron energy E'_e and angle θ_e, where θ_e is measured from the incoming proton direction defined to be along $+z$ direction. In this case, the variables become

$$\begin{aligned} Q^2_e &= 2E_e E'_e(1 + \cos\theta_e) \\ x_e &= \frac{E_e}{E_p}\left[\frac{E'_e(1 + \cos\theta_e)}{2E_e - E'_e(1 - \cos\theta_e)}\right] \\ y_e &= 1 - \frac{E'_e}{2E_e}(1 - \cos\theta_e) \end{aligned} \tag{6.2}$$

   where E_p is the incoming proton energy.

2. The Jacquet–Blondel (JB) method[31]: The kinematic variables are reconstructed from the struck quark hadronic jet using the magnitude of the vector sum of the transverse momentum of the hadrons ($P_{t_{jb}}$) and from the hadronic longitudinal energy sum $\sum(E - P_z)_{jb}$. The kinematic variables are

$$\begin{aligned} Q^2_{jb} &= \frac{(\sum_i P_{xi})^2 + (\sum_i P_{yi})^2}{1 - y_{jb}} \\ x_{jb} &= \frac{Q^2_{jb}}{s y_{jb}} \\ y_{jb} &= \frac{\sum_i(E_i - P_{zi})}{2E_e} \end{aligned} \tag{6.3}$$

   Since the calorimeter is used to measure energies, then the summation is over the calorimeter cells.

3. The Double Angle (DA) method: In this method, only the angles of the scattered electron, θ_e, and the hadronic jet, γ_H, are used. The angle γ_H is that of a massless object balancing the momentum vector of the

electron. In the näive parton model, it is the scattering angle of the struck quark. It is determined from the hadronic flow measured in the detector using the equation

$$\cos\gamma_H = \frac{P_{t,jb}^2 - 4E_e^2 y_{jb}^2}{P_{t,jb}^2 + 4E_e^2 y_{jb}^2} \tag{6.4}$$

The kinematic variables are given by

$$\begin{aligned} Q_{DA}^2 &= \frac{4E_e^2}{A}\sin\gamma_H(1+\cos\theta_e) \\ x_{DA} &= \frac{E_e}{E_pA}[\sin\gamma_H + \sin\theta_e + \sin(\theta_e+\gamma_H)] \\ y_{DA} &= \frac{1}{A}\sin\theta_e(1-\cos\gamma_H) \end{aligned} \tag{6.5}$$

where $A = \sin\gamma_H + \sin\theta_e - \sin(\theta_e + \gamma_H)$.

The DA method reconstructs Q^2 with negligible bias and good resolution[30] over a wide range of Q^2 because it is independent of the measured energy. It is used to reconstruct the NC kinematics. The electron method is used as part of the NC selection to reject background and as a consistency check.

For CC events, since only a hadronic jet is observed in the final state, the JB method must be used. However, when the calorimeter is used for energy measurements, the JB method becomes biased toward lower energy values due to hadronic energy loss in the inactive material front of the calorimeter. Therefore, in this case, the JB method has the worst resolution[30] when compared to the electron and the DA methods.

6.2 Monte Carlo Simulation

The acceptance of the trigger and data selection is determined by passing the Monte Carlo events through the reconstruction and selection procedure identical to those for the data, described in chapter 7. The detector simulation is based on the GEANT[33] program and incorporates knowledge of the apparatus, test beam results, and trigger.

Events from CC and NC DIS processes are generated using the event-generator LEPTO[34] with matrix element plus parton shower (MEPS) option. Electroweak radiative corrections are implimented with the use of HERACLES[35] as interfaced to LEPTO by DJANGO.[36] The proton parton densities are chosen to be either the MRSD$'_0$ set[45] or MRSD$'_-$. To study the sensitivity of the resolution and acceptance to models of the final state and fragmentation, additional samples are generated with ARIADNE.[38] An additional set of NC events have been generated using the Color Dipole Model + Boson Gluon Fusion model (CDMBGF) of hadronization.

Chapter 7

DATA SELECTION

7.1 NC Data Selection

In this section, the NC data selection cuts are described. These cuts are summarized in Table 7.1, which also gives each cut efficiency for the NC events surviving all cuts through the previous cut, as determined from NC Monte Carlo events with true $Q_t^2 > 400\ GeV^2$.

A cone–based algorithm[40] (ELEC5) is used to find electrons. At times this electron finder reports more than one electron candidate. By default, it selects the electron candidate with the highest transverse momentum, p_t^e. However, sometimes the electron finder selects the highest p_t^e electron candidate within the struck quark jet instead of the true electron candidate which has a lower p_t^e. Therefore, for this analysis, an improved selection procedure is used with the electron finder. The improved finder selects the electron candidate which satisfies the largest number of the following five requirements: the smallest y_e, smallest y_{jb}, and highest p_t^2, most isolated (the distance–weighted sum of energy near the candidate, $\sum_i E_i/d_i^2$, is the smallest, where E_i is the ith cell energy and d_i is the distance from the cell's center to the electron candidate position), and the smallest difference between the electron candidate angle and the jet angle of any other electron candidate.

The Third level Trigger NC filter[39] ($\delta = E - P_z > 25\ GeV$ and $E_e' > 4\ GeV$) selects 351000 candidates, out of which 1305 events have $E_e' > 10\ GeV$ and $Q_{DA}^2 > 400\ GeV^2$, where E_e' is the scattered electron energy. Many of the electron candidates selected at this stage are energetic EMC clusters in the very forward direction associated with the recoil hadrons from ep scattering. They tend to reconstruct at high y_e and are rejected by a cut of $y_e < 0.95$, reducing the sample to 863 events. To eliminate events with initial state radiation or from photoproduction, we require $\delta > 35\ GeV$. The cosmic ray background is eliminated by requiring $p_t/\sqrt{E_t} < 2\ GeV^{\frac{1}{2}}$, where p_t and E_t are summed over the whole event, leaving 493 events. To reduce the remaining photoproduction background, the electron and DA reconstruction methods are required to be consistent by demanding $0.7 < Q_e^2/Q_{DA}^2 < 1.2$. 474 events pass this cut.

After the above cuts, a small background of photoproduction events is still present in the data. This background is usually associated with energetic EMC deposits (e.g. π^0-decay) contained within or near the hadronic jet, resulting in fake electrons. Part of this background are low Q^2 DIS events, with fake electrons more forward than the true scattered electron, and resolved photoproduction events in which the electron candidate is an EMC deposit inside the photon remnant jet or a real scattered electron near the RCAL beampipe. This background is cut by requiring either a high energy scattered electron ($E_e' > 20\ GeV$) or that the scattered electron has a matched CTD track and it is either found by the Sinistra[41] electron finder (a neural network based algorithm that has a higher efficiency for rejecting events with hadronic energy near EMC deposits), or it is very isolated ($\sum_i E_i/d_i^2 < 3$, where E_i and d_i are defined above). In addition, all events must have energy within the 2 concentric rings of single towers surrounding the RCAL beampipe less than 1 GeV. The combination of these three cuts, which is referred to as "CT-Dtrk, iso, RCALbp" in table 7.1, leaves 436 events as the final NC sample with $Q_{DA}^2 > 400\ GeV^2$. Figure 7.1 shows a NC event from the final sample. The photoproduction background after these cuts is estimated to be less than 2%, by generating photoproduction Monte Carlo events, using the Pythia 5.6[42] event generator, and applying the same NC selection cuts on the reconstructed Monte Carlo events.

Figures 7.2 and 7.3 show distributions for NC data and Monte Carlo events after the successive cuts, described above, in order to see the relative cut efficiency (with respect to the events passing the previous cut) and the background rejected. For example, figure 7.2(A) shows the E_e' distribution for events with $Q_{DA}^2 > 400\ GeV^2$. Figure 7.2(B) shows events with $Q_{DA}^2 > 400\ GeV^2$ and $E_e' > 10\ GeV$, and so on. In these and all subsequent plots in this chapter, Monte Carlo events are absolutely normalized to data by luminosity, unless otherwise indicated.

Figures 7.4 and 7.5 show the event distributions, for data and Monte Carlo, after all NC selection cuts except that mentioned on the caption above each distribution. These figures show the absolute efficiency of each cut in selecting NC data events.

In all the aforementioned figures, the NC Monte Carlo predicts higher energies than the NC data, as is seen from the slight shift of the data from the

Monte Carlo predictions. This is because the NC Monte Carlo predicts more energy for the scattered electron by a scale factor of 6%. Figure 7.6 compares the scattered electron energy, E_e', distribution of the final NC data candidates with NC Monte Carlo. The 6% scale factor maybe to possibly incomplete simulation of inactive material in front of the calorimeter[1]. It is determined from the difference between the data and Monte Carlo prediction for the ratio E_e'/E_{DA}', where E_{DA}' is the scattered electron energy reconstructed with the DA reconstruction method. This method is used since the DA reconstruction is largely independent of the measured energies (section 6.1) and there is excellent agreement between data and Monte Carlo spectra for E_{DA}' (figure 7.7).

Finally, figure 7.8 shows the efficiency of the selection cuts for NC Monte Carlo events with true Q^2, Q_t^2, greater than 400 GeV^2. The overall efficiency is 0.82 .

7.2 CC Data Selection

This section details the CC selection cuts, which are summarized in table 7.2. In contrast to the NC DIS events, the final state lepton in a CC event is a neutrino and is not detected. Therefore, there is large missing transverse momentum, p_{tmiss}, in the final state. The Third Level Trigger (TLT) CC selection[39] ($p_{tmiss} > 9\ GeV$ and either a track, or $E_{FCAL} > 10\ GeV$) passes approximately 33000 events. Using events from the non-colliding electron and proton bunches, it is estimated that half of the TLT CC selected events

---

[1] The absolute calorimeter energy scale is known to better then 2% from halo-muon calibration events.

Selection Criteria	Events Remain	NC-cut ϵ	Comments
NC Trig/DST	351000	×0.92	$\delta^{\dagger} > 25\ GeV, E'_e > 4\ GeV$
$Q^2_{DA} > 400\ GeV^2$	3569	×0.94	
$E' > 10\ GeV$	1305	×0.96	High efficiency for electron reconstruction
$y_e < 0.95$	863	×0.99	php* with fake forward electrons (γ from π^0 decays)
$\delta > 35\ GeV$	613	×0.96	$\delta \sim 2E_e = 53.4\ GeV$ for events fully contained in CAL; php at $\delta < 35\ GeV$
$P_t/\sqrt{E_t} < 2\ GeV^{1/2}$	493	×0.98	cosmics
$0.7 < Q^2_e/Q^2_{DA} < 1.2$	474	×0.99	php
CTDtrk, iso, RCALbp	436	×0.97	php with fake electrons
Events remain NC events (bkg)	436 436(8.7)		SCANNED bkg = php from MC‡

*php = photoproduction, $^{\dagger}\delta = E - P_z$, ‡MC = Monte Carlo

Table 7.1: *Summary of NC selection cuts starting with $Q^2_{DA} > 400\ GeV^2$: the cuts are listed in column 1. The number of events selected is in column 2. Column 3 shows the efficiency of the cut with respect to the events passing the preceding cut using NC Monte Carlo events with true $Q^2_t > 400\ GeV^2$. The motivation for each cut is given in column 4, with further details in the text.*

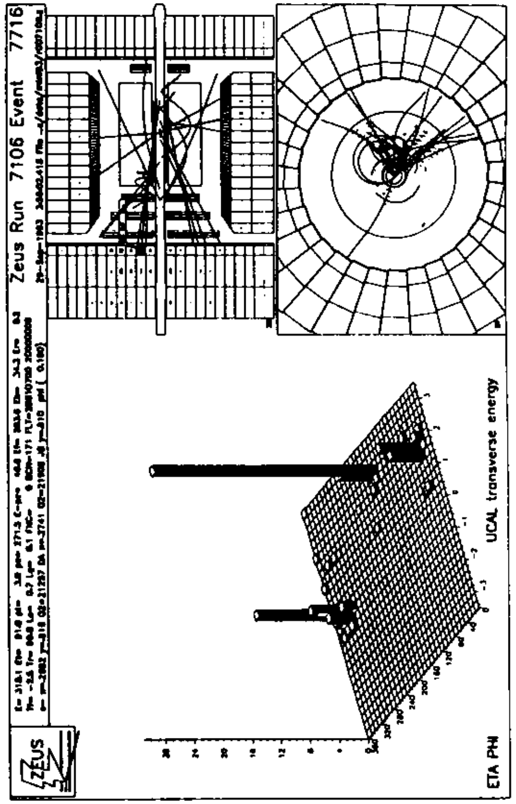

Figure 7.1: *A NC data event with $Q^2_{DA} = 20000\ GeV^2$, $x_{DA} = 0.27$, and $E'_e = 202\ GeV$.*

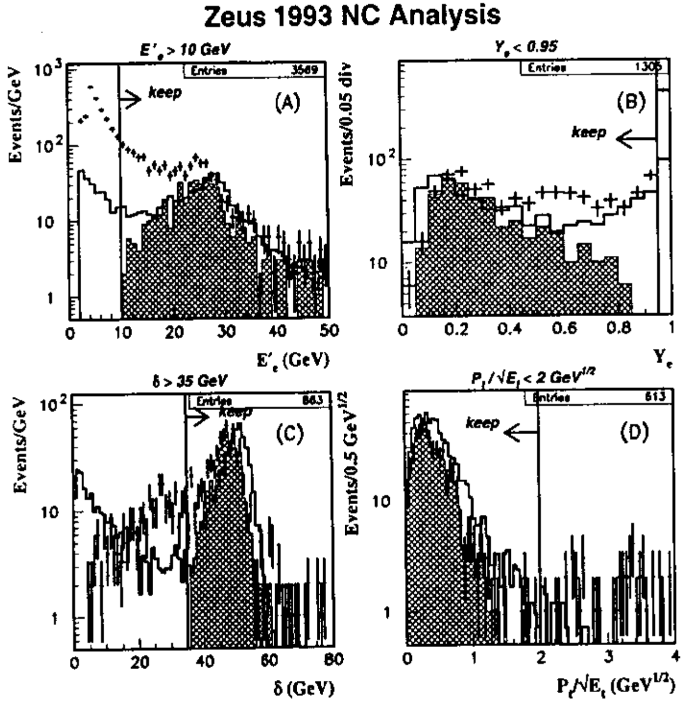

Figure 7.2: *NC data reduction. Points with error bars are the NC candidates, solid histograms are the NC Monte Carlo simulation, and shaded histograms are the final 436 NC data candidates. The cuts are indicated by the caption above each plot. The data are shown after all previous cuts: (A) Scattered electron energy, E'_e (B) y_e (C) $\delta = E - P_z$ (D) $p_t/\sqrt{E_t}$ (continued in fig. 7.3).*

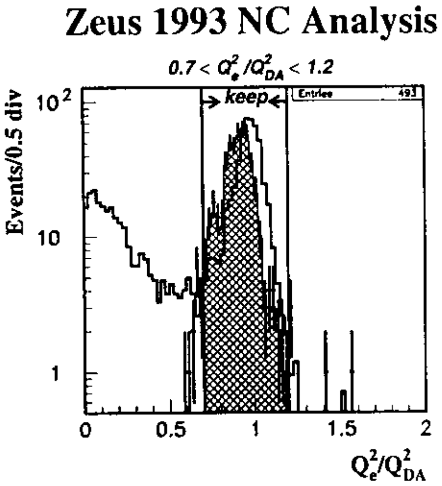

Figure 7.3: *NC data reduction, continued. Q^2_e/Q^2_{DA}: Points with error bars are the NC candidates, solid histograms are the NC Monte Carlo simulation, and shaded histograms are the final 436 NC data candidates. The cut is indicated by the caption above the plot. The data are shown after all previous cuts.*

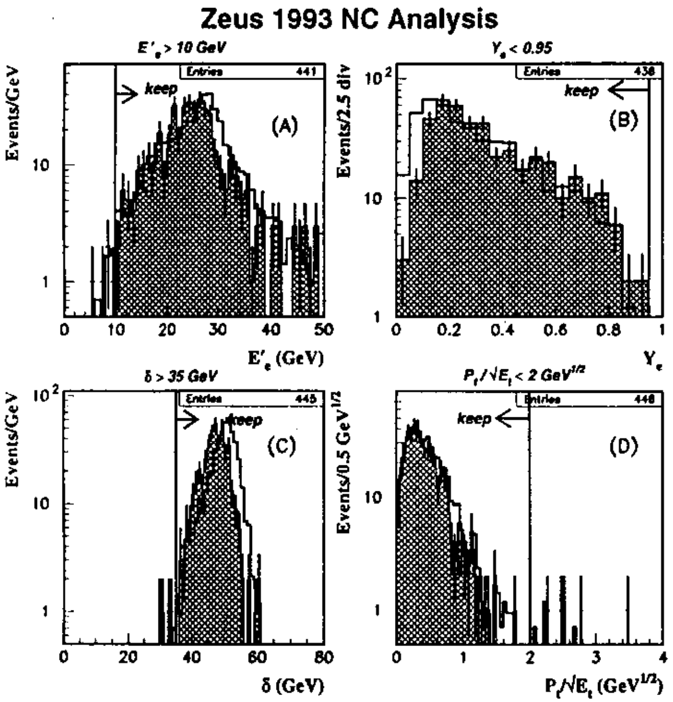

Figure 7.4: *Effects of the NC selection cuts. Points with error bars are the NC candidates, solid histograms are the NC Monte Carlo, and shaded histograms are the final 436 NC data candidates. Data are shown after all selection cuts are applied except the cut displayed in the caption: (A) Scattered electron energy E'_e (B) y_e (C) $\delta = E - P_z$ (D) $p_t/\sqrt{E_t}$ (continued in fig. 7.5).*

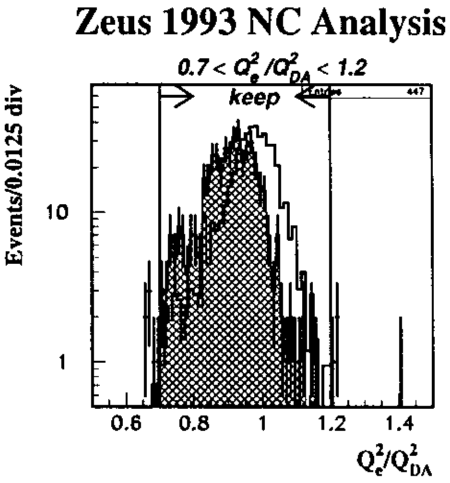

Figure 7.5: *Effects of the NC selection cuts, continued. Q^2_e/Q^2_{DA}: Points with error bars are the NC candidates, solid histograms are the NC Monte Carlo, and shaded histograms are the final 436 NC data candidates. Data are shown after all selection cuts are applied except the Q^2_e/Q^2_{DA} cut.*

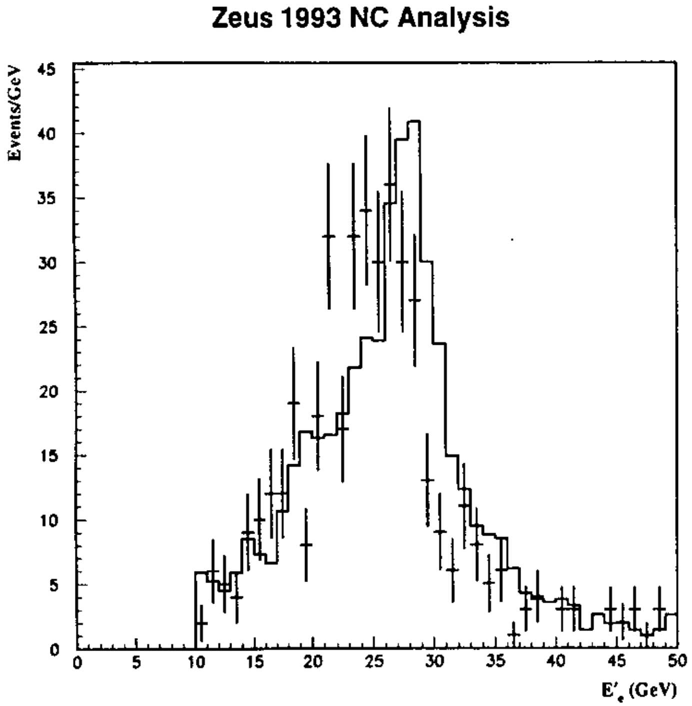

Figure 7.6: *Scattered electron energy, E'_e, for the final 436 NC data candidates (histogram with error bars) compared to NC Monte Carlo (solid histogram).*

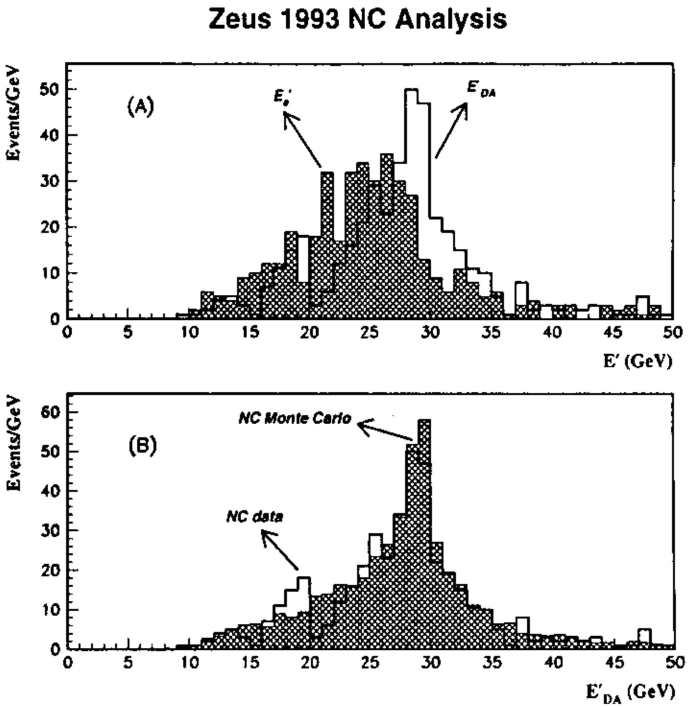

Figure 7.7: *(A) Comparison of the scattered electron energy, E'_e, (shaded histogram) and E'_{DA} (unshaded histogram) for the final 436 NC data candidates, where E'_{DA} is the scattered electron energy reconstructed by the DA reconstruction method. (B) Comparison of E'_{DA} spectra for the final 436 NC data candidates (unshaded histogram) and NC Monte Carlo (shaded histogram).*

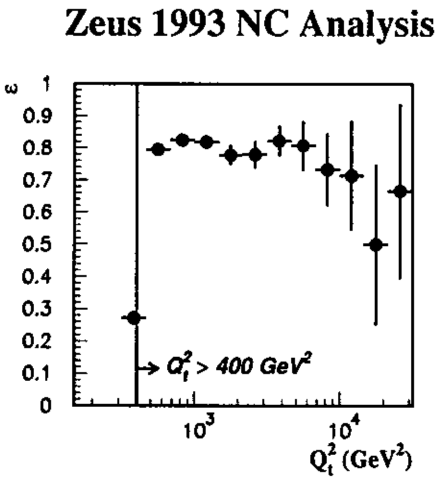

Figure 7.8: *Cut efficiency for NC Monte Carlo events with* $Q_t^2 > 400\ GeV^2$.

are cosmic ray interactions and the remainder are primarily proton beam-gas interactions. Of the 33000 events, 86%, including most of the cosmics, are rejected by requiring a vertex with at least two tracks in the CTD reconstructed in the range $|z| < 45cm$.

Figure 7.10 shows the number of tracks not associated with the primary event vertex, $|z|$, and p_{tmiss} distributions for events in non-colliding ep bunches. Beam-gas background is reduced by requiring $p_{tmiss} > 12\ GeV$ and the number of tracks not associated with the primary event vertex < 40. 1852 events pass these cuts. Figures 7.11 and 7.12 show distributions of the data after each stage of the selection cuts and compare them with the Monte Carlo event simulation.

Beam–gas interactions that occur away from the nominal interaction point downstream in the proton ring result in halo muons that are detected by the Veto Wall. Events with hits in the Veto Wall are rejected, leaving 1685 events. Residual beam-gas events within ZEUS tend to deposit energy mainly in the FCAL beampipe region. In figure 7.12 the ratio $r = p_{tmiss}^{out}/p_{tmiss}$ is shown for the 1685 events passing the above cuts, where p_{tmiss}^{out} is the total missing transverse momentum outside a box of ±50 cm centered on the FCAL beampipe axis. Most of the CC events are expected to concentrate at $r \sim 1$ while the beam-gas events are at $r < 1$. Therefore, only events with $r > 0.7$ are selected for further analysis.

The $p_{tmiss}^{out}/p_{tmiss}$ cut rejects most of the beam–gas background, reducing the number of events from 1685 to 113, at a relative efficiency of 0.9 for CC events, as shown in table 7.2. The CC events that fail this cut are concentrated at large x. The dominant remaining backgrounds are from cosmic ray interactions, including muon overlays in which a cosmic shower is contained within the same beam crossing as a beam–gas event or an ep event. 19 events are classified as muons by the muon finder [43] and are removed.

Another powerful muon rejector uses the event times available from each calorimeter cell. The calorimeter is segmented into 18 regions, 16 of which are similar to the CFLT segmentation (section 5.3.2). In addition, 2 more regions are formed by the 3 concentric rings of calorimeter cells surrounding the FCAL and RCAL beampipes. Figure 7.12 shows the distribution of the difference, ΔT, between the region with the earliest time and that of the latest time. The peak at $\Delta T = 11\ ns$ reflects the time of flight of muons traversing several sections of the calorimeter. The excess at $\Delta T > 13\ ns$ are cosmic overlays which overlap ep events. Demanding $\Delta T < 8\ ns$, the earliest and latest times less than 8 ns, and at least one region reporting a time, rejects 65 events. An additional 3 events are removed because they have reconstructed tracks in 3 or more muon chambers, leaving 26 events in the data sample.

A final selection cut is required to eliminate backgrounds from calorimeter noise pulses and from NC DIS at high x in which the hadrons go down the FCAL beampipe undetected. These backgrounds are reduced by demanding that no calorimeter cell contains more than 75% of the total p_{tmiss} of the event. This cut is shown as $p_{tmiss}^{maxcell}/p_{tmiss} < 0.75$ in table 7.2. 2 events are rejected with this cut (figure 7.12), leaving 24 CC candidates in the final sample, of which 23 candidates have $Q^2 > 400\ GeV^2$. A CC candidate from this sample is shown in figure 7.9.

Figures 7.13 and 7.14 show additional distributions of the above mentioned cut variables for CC data and Monte Carlo events. These figures show the absolute efficiency of each cut in selecting CC events by plotting data and Monte Carlo with all the CC selection cuts applied except the cut mentioned on the caption above each figure. The absolute efficiency of the $p_{tmiss}^{maxcell}/p_{tmiss}$ cut is shown in figure 7.12(C). The combination of the cut on the number of chambers of the muon detector and presence of a muon from the muon finder rejects 4 events after all the other cuts are applied, with the muon finder rejecting one cosmic event. It should be noted that $p_{tmiss}^{out}/p_{tmiss} > 0.7$ is the most powerful of the selection cuts. By applying this cut alone (figure 7.14(C)), the number of events is reduced from 1150 to 24. Although this reduces the efficiency of CC selection by 10%, as seen from table 7.2, most of the background close to the FCAL beampipe is rejected. As mentioned above, the CC events lost by this cut are high x events with hadron jets confined in the forward area of the calorimeter.

The efficiency of the cuts for CC Monte Carlo events with $Q_t^2 > 400\ GeV^2$ is shown in figure 7.15. The overall efficiency for the CC selection is 0.76 .

Selection Criteria	Events Remain	CC-cut ϵ	Comments
CC Trig/DST	33584	×0.87	$p_{tmiss} > 9\ GeV$, track or Fcal
Require Vertex	18636	×0.94	
Trks on Vertex ≥ 2	13544	×0.95	cosmics rarely make vertex
$\|z\| < 45\ cm$	4547	×0.99	cosmics + p-gas* far from nominal IP†
$p_{tmiss} > 12\ GeV$	2781	×0.92	CC have high p_{tmiss}
Number of tracks not associated with primary vertex < 40	1852	×1.00	p-gas has lots of tracks
no Veto Wall hits	1685	×1.00	halo muons
$p^{out}_{tmiss}/p_{tmiss} > 0.7$	113	×0.90	p-gas concentrated near bp‡
muon finder	94	×1.00	
Cal regional time-diff < 8 ns	29	×0.99	Remove p-gas + overlay cosmics
muon chambers < 3	26	×1.00	cosmics
$p^{maxcell}_{tmiss}/p_{tmiss} < 0.75$	24	×1.00	Remove p-gas + spark/muon overlays
Events remain	24		SCANNED
CC Candidates (bkg)	24(< 1.05)		bkg = php and NC from Monte Carlo
CC Candidates with $Q^2 > 400\ GeV^2$	23		

*p-gas = proton–gas, †IP = interaction point, ‡ bp = beampipe

Table 7.2: *Summary of CC selsection cuts: the cuts are listed in column 1. The number of events at each cut stage is in column 2. Column 3 shows the efficiency of the cut relative to the preceding cut using CC Monte Carlo with $Q_t^2 > 400\ GeV^2$. The motivation for each cut is given in column 4, with further details in the text.*

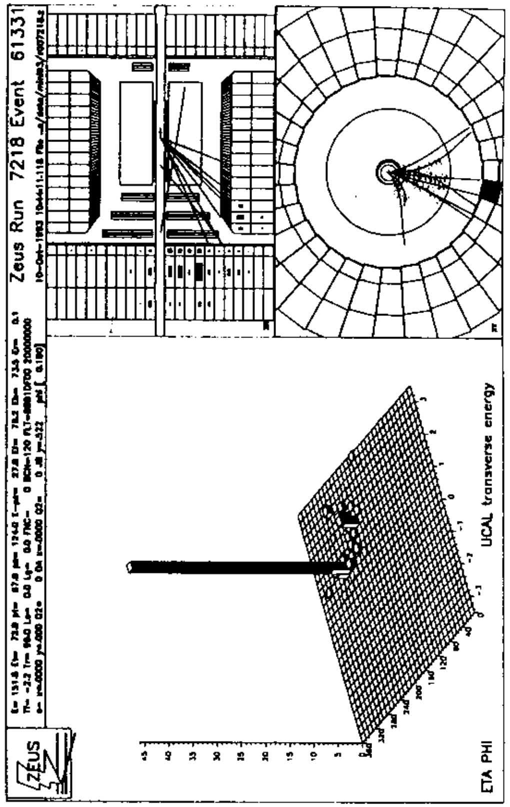

Figure 7.9: *A CC candidate with $p_{tmiss} = 67.8\ GeV$, $y_{jb} = 0.52$, and $Q^2_{jb} = 9577\ GeV^2$.*

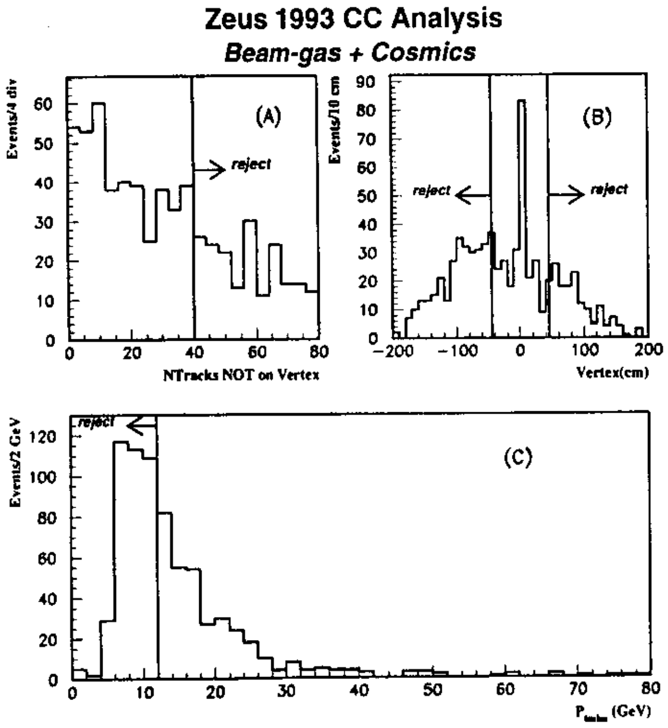

Figure 7.10: *Rejection of beam-gas and cosmic events. This figure shows distributions for non-ep events from unpaired electron and proton bunches: (A) Number of tracks not associated with the primary vertex (B) Vertex z position(C) Total missing transverse momentum,* p_{tmiss}.

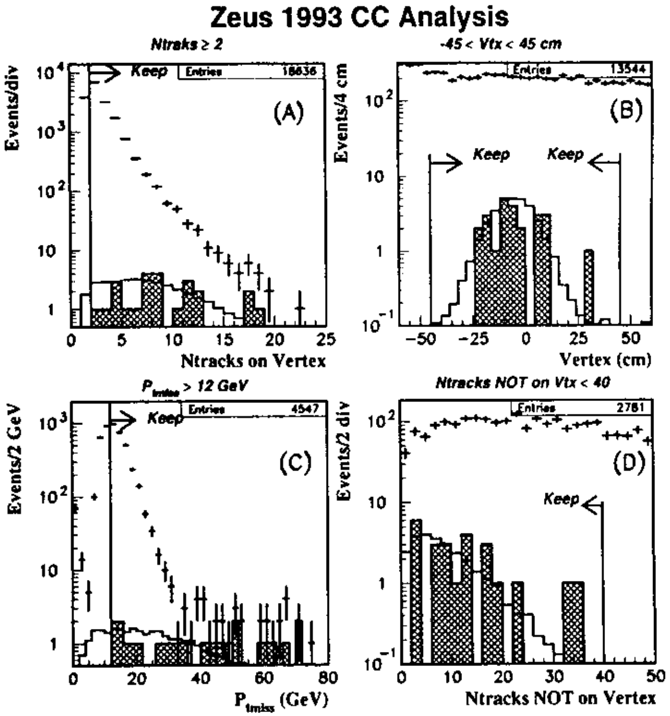

Figure 7.11: *CC data reduction. Points with error bars are the data, shaded histograms are the 24 final CC candidates, and solid histograms are the CC Monte Carlo. The selection cuts are indicated by the caption above each figure: (A) Number of tracks on primary vertex (B) Vertex z position (C) Total missing transverse momentum,* p_{tmiss} *(d) Number of tracks not associated with the primary vertex (continued in fig. 7.12).*

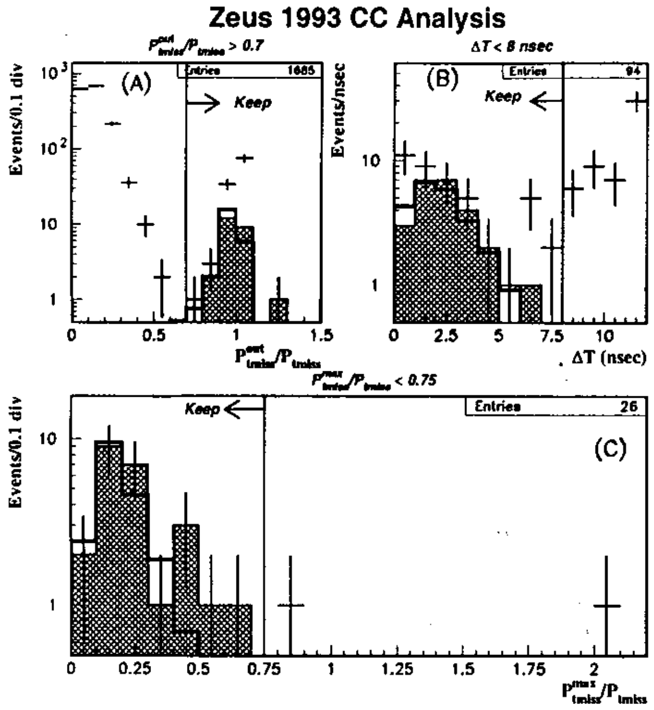

Figure 7.12: *CC data reduction, continued from fig. 7.11. Points with error bars are the data, shaded histograms are the 24 final CC candidates, and solid histograms are the CC Monte Carlo. In figure (B), the shaded histogram is NC data events normalized to the final CC data events. The selection cuts are indicated by caption above each figure: (A) $r = p^{out}_{tmiss}/p_{tmiss}$ (B) Difference in time between calorimeter regions, ΔT (C) $p^{maxcell}_{tmiss}/p_{tmiss}$.*

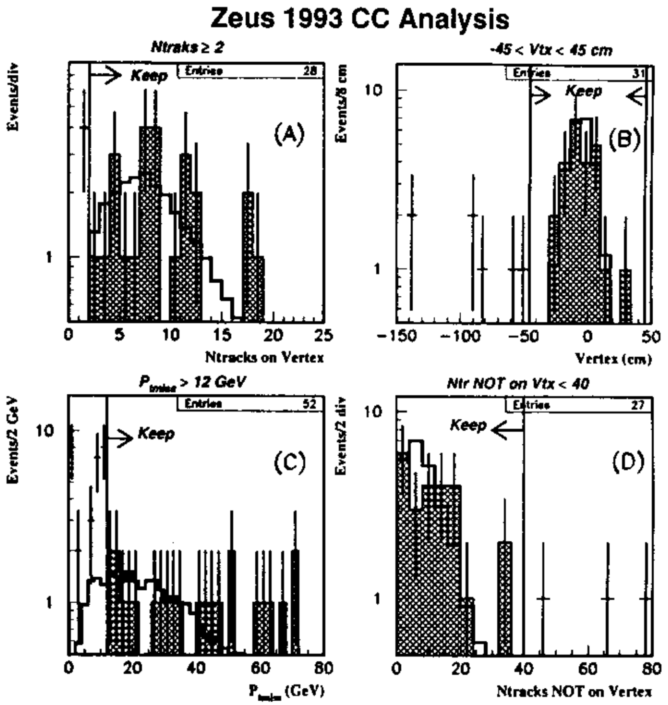

Figure 7.13: *Effects of the CC selection cuts. Data are shown after all cuts except the one mentioned in the caption above the figure. Points with error bars are the data, shaded histograms are the final 24 CC candidates, and solid histograms are the CC Monte Carlo: (A) Number of tracks on vertex (B) Vertex z position (C) Total transverse momentum, p_{tmiss} (D) Number of tracks not on the vertex (continued in fig. 7.14).*

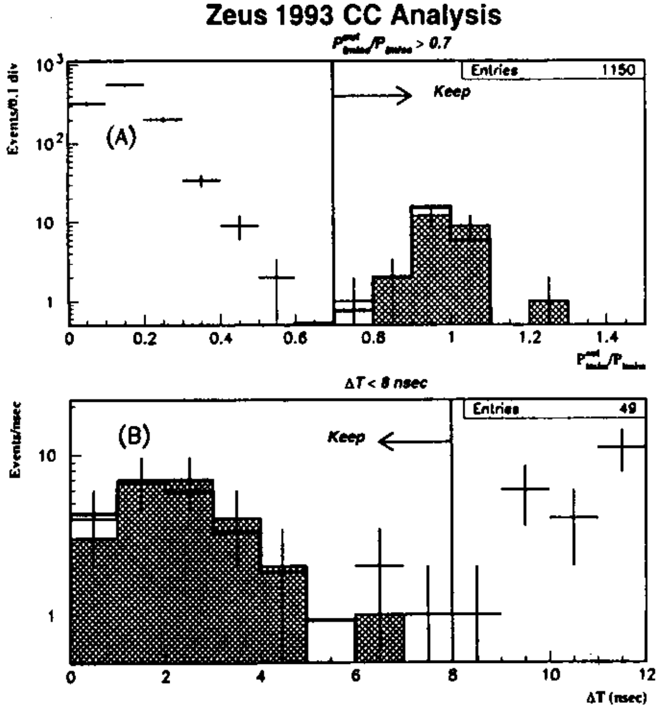

Figure 7.14: *Effects of CC selection cuts, continued from fig. 7.13: Data are shown after all cuts except the one mentioned in the caption above the figure. Points with error bars are the data, shaded histograms are the final 24 CC candidates, and solid histograms are the Monte Carlo: (A) $p^{out}_{tmiss}/p_{tmiss}$ (B) Deifference in time between calorimeter regions, ΔT.*

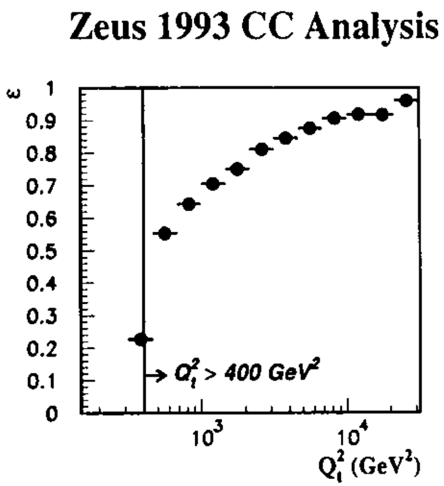

Figure 7.15: *CC cut efficiency for CC Monte Carlo for $Q_t^2 > 400$ GeV^2.*

7.3 Bins For Cross Section Measurements

The NC and CC cross section are measured in five Q^2 bins. The bins are $100\ GeV^2 < Q^2 < 1000\ GeV^2$, $1000\ GeV^2 < Q^2 < 2500\ GeV^2$, $2500\ GeV^2 < Q^2 < 6250\ GeV^2$, $6250\ GeV^2 < Q^2 < 15625\ GeV^2$, and $Q^2 > 15625\ GeV^2$.

The cross section, σ, in each NC(CC) bin is measured according to the formula

$$\sigma = \frac{N}{\mathcal{L}\mathcal{A}} \tag{7.1}$$

where N is the number of observed NC(CC) data events, $\mathcal{L} = 0.54 \pm 0.0135 pb^{-1}$ is the luminosity, and $\mathcal{A}$ is the bin acceptance. $\mathcal{A}$ is given by

$$\mathcal{A} = \frac{N^{rec}}{N^{gen}} \tag{7.2}$$

N^{rec} is the number of NC(CC) Monte Carlo events reconstructed with Q^2 in the bin and N^{gen} is the number of NC(CC) Monte Carlo events generated with Q^2 in the bin. Monte Carlo events are generated without radiative corrections. The effect of these corrections is described in section 9.2.5.

Chapter 8

CC HADRONIC CORRECTION

8.1 Motivation

As mentioned in section 6.1, the CC data can only be reconstructed with the JB method. If calorimetry is used to measure energies, then, unlike the DA reconstruction method (section 6.1), the JB reconstruction underestimates Q^2 over a large range of Q^2. This is shown in figure 8.1, which compares the JB reconstruction to the DA reconstruction using NC Monte Carlo events with true $Q_t^2 > 400\ GeV^2$ and transverse momentum, $P_{t,h}$, of the hadronic jet $> 12\ GeV$). This bias toward lower Q^2 is due to loss of particle energy in the inactive material in front of the calorimeter. To minimize the event migration between Q^2 bins, one needs to correct for this loss of energy.

We use a method of correcting for energy loss by using a set of events that (1) are measured by their hadronic energies where these energies are large enough, and (2) are reconstructed by an independent method that predicts what the hadronic energies should be if there are no losses due to dead material. The NC data are used to obtain an empirical formula that relates the observed hadronic energies to the DA predictions, since the NC events can be reconstructed by both the DA reconstruction and the JB reconstruction. This correction can then be applied to the CC data sample to determine the corrected kinematics. In this chapter this correction procedure is described, where the DA predictions are considered as the "true" predictions since they do not depend on the measured energies (section 6.1). The corrections used are two multiplicative factors, $R_i(P_{tjb}, y_{jb})$, $i = 1, 2$, that depend on P_{tjb} (transverse momentum of the hadronic sector of the event) and y_{jb}. These factors correct both P_{tjb} and y_{jb}, resulting in the corrected variables $P_{tcor} = R_1(P_{tjb}, y_{jb})P_{tjb}$ and $y_{cor} = R_2(P_{tjb}, y_{jb})y_{jb}$. Then the corrected $Q^2(Q^2_{cor})$ is found from

$$Q^2_{cor} = \frac{P^2_{tcor}}{1 - y_{cor}} \tag{8.1}$$

This method provides an event by event correction to the measured P_{tjb} and y_{jb} without making corrections on the individual calorimeter cells summed to make these quantities.

Two methods are used to determine the factors R_1 and R_2. Section 8.2 describes the first method, which uses the NC data to determine R_1 and R_2 ("data correction"). The factors obtained from this method are used to correct the CC data. Section 8.3 describes the other method, which uses the NC Monte Carlo to find R_1 and R_2 ("Monte Carlo correction"). The values of R_1 and R_2 obtained from the Monte Carlo correction are used to correct the CC Monte Carlo events.

The data and Monte Carlo corrections are also compared to the JB reconstruction. Since we are correcting the JB variables back to their DA values, the DA reconstruction predictions are treated as the true predictions. The bin to bin migration, bin acceptance, and bin purity (defined in section 8.4) are obtained from NC Monte Carlo events and compared to the CC Monte Carlo migration, acceptance, and purity after the Monte Carlo correction is applied.

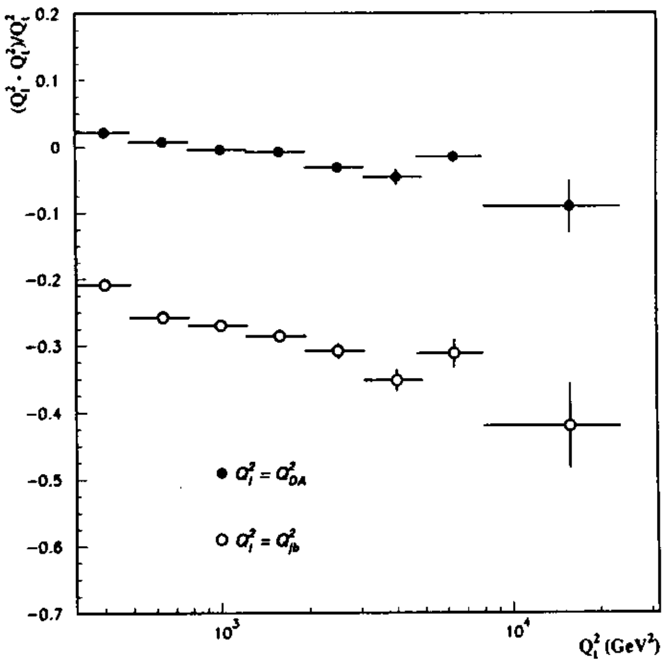

Figure 8.1: *Comparison of the JB and DA reconstruction methods. This figure shows $(Q_i^2 - Q_t^2)/Q_t^2$ vs Q_t^2 for NC Monte Carlo events with $Q_t^2 > 400$ GeV^2 and hadronic transeverse momentum $P_{tjb} > 12$ GeV.*

8.2 Data Correction Method

8.2.1 NC Data Sample and Binning

A NC data sample with $Q^2 \geq 100\ GeV^2$ is used to correct P_{tjb} and y_{jb}. The selected sample is based on the following cuts: $E_e \geq 10\ GeV$, $E - P_z \geq 35\ GeV$, $0.7 \leq Q_e^2/Q_{DA}^2 \leq 1.2$, $y_e \leq 0.95$, $P_t/\sqrt{E_t} \leq 2$, and $|z| < 50cm$. The estimated background from photoproduction with these cuts is less than 2%. This background is estimated by generating photoproduction events with the Pythia[42] event generator and applying these cuts on them.

The data are divided in 3 bins of P_{tjb} ($10\ GeV \leq P_{tjb} < 14\ GeV, 14\ GeV \leq P_{tjb} < 19\ GeV$, and $P_{tjb} \geq 19\ GeV$) and 3 bins of y_{jb} ($y_{jb} < 0.1, 0.1 \leq y_{jb} < 0.3$, and $y_{jb} \geq 0.3$) . A total of 1406 NC events are contained in these bins. In each bin, a plot of y_{DA}/y_{jb} vs P_{tjb} and P_{tDA}/P_{tjb} vs y_{jb} is obtained. Figure 8.2 shows the plots of P_{tDA}/P_{tjb} vs y_{jb} and vs P_{tjb} for the bins. In only this plot, the $|z| < 50cm$ is not applied, which results in additional 42 events. The DA method, as used by ZEUS, assumes that no p_t is lost down the beampipe. This gives the result that $y_{DA}/y_{jb} = P_{tDA}/P_{tjb}$, where P_{tDA} is p_t reconstructed using the DA reconstruction. Therefore, plots for y_{DA}/y_{jb} are the *same* as for P_{tDA}/P_{tjb}.

8.2.2 The Data Correction Function

Figure 8.2 shows P_{tDA}/P_{tjb} vs P_{tjb} and y_{jb}. As is seen from this figure, the data correction function gives a larger correction at small P_{tjb} and then decreases asymptotically with increasing momentum. This is because higher energy jets traverse the inactive material in front of the calorimeter with less fractional

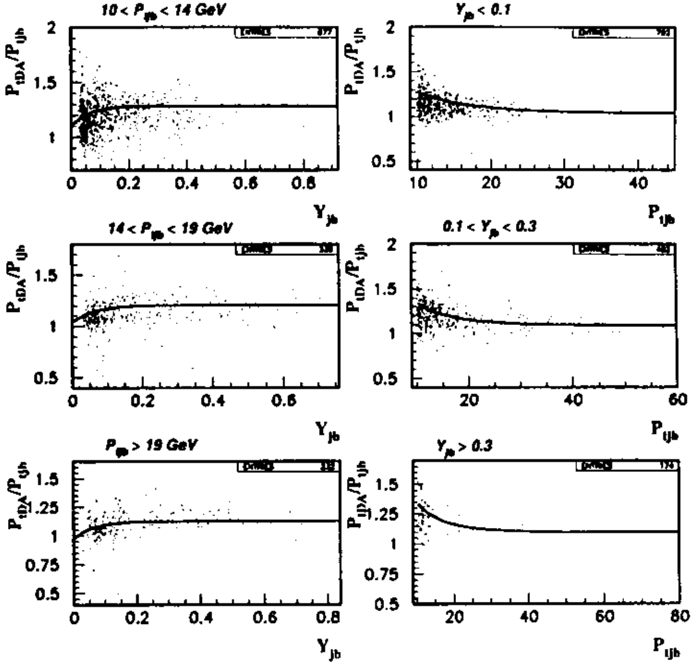

Figure 8.2: P_{tDA}/P_{tjb} *vs* y_{jb} *(left column) and vs* P_{tjb} *(right column) for various bins of* P_{tjb} *and* y_{jb}. *The solid lines represent the correction: it is small for small* y_{jb}, *rising to a constant value as* y_{jb} *becomes larger. In the case of* P_{tjb}, *the dependence on* P_{tjb} *behaves oppositely.*

energy loss. Therefore, a smaller fraction of energy is lost before these particles are detected, resulting in a smaller correction. At lower energies, more particles are lost from the jet and, therefore, a larger correction is needed. We parametrize this behavior by

$$A(P_{tjb}) = \frac{1}{a - \exp(-bP_{tjb})} \tag{8.2}$$

The opposite is true when y_{jb} is considered. In this case, a smaller correction is needed at small y_{jb}, since events with small y_{jb} are not energetic, therefore, particles are lost from the hadronic jet. At larger y_{jb}, a larger correction is needed with the function flattening out quickly with rising y_{jb} because these are energetic events that lose less energy in the inactive material before reaching the calorimeter. Therefore, we parametrize this correction as

$$B(y_{jb}) = c - f\exp(-gy_{jb}) \tag{8.3}$$

where a, b, c, f, and g are fit parameters. As mentioned above, the plots for y_{DA}/y_{jb} are the same as for P_{tDA}/P_{tjb}. Therefore, both $R_1(P_{tjb}, y_{jb})$ and $R_2(P_{tjb}, y_{jb})$ have the same functional form. This functional dependence is given by $R_{1,2}(P_{tjb}, y_{jb}) = A(P_{tjb})B(y_{jb})$ with

$$R_{1,2}(P_{tjb}, y_{jb}) = \frac{c - f\exp(-gy_{jb})}{a - \exp(-bP_{tjb})} \tag{8.4}$$

To determine the parameters of the above formula, the following function is minimized,

$$\chi^2 = \sum_{i=1}^{1406} \left\{ \left[r_i - \frac{c - f\exp(-gy^i_{jb})}{a - \exp(-bP^i_{tjb})} \right] / (\delta r_i)^2 \right\}^2 \tag{8.5}$$

where the sum is over the 1406 NC data points, $r_i = P^i_{tDA}/P^i_{tjb} = y^i_{DA}/y^i_{jb}$, and δr_i is the error estimate on r_i (see appendix for estimates of δr_i). Note that two different fits are performed because δr_i for P^i_{tjb}/P^i_{tDA} is different from that of y^i_{jb}/y^i_{DA} even though the ratios are equal (for further details, see appendix).

Fit Parameters	Data		Monte Carlo	
	R_1	R_2	R_1	R_2
a	1.38 ± 0.30	2.72 ± 1.05	3.42 ± 0.49	4.85 ± 3.85
b	0.17 ± 0.02	0.12 ± 0.04	0.10 ± 0.02	0.11 ± 0.09
c	1.50 ± 0.31	3.00 ± 1.12	3.62 ± 0.49	5.25 ± 3.68
f	0.25 ± 0.06	0.59 ± 0.30	0.49 ± 0.12	0.71 ± 0.72
g	15.24 ± 1.96	19.62 ± 5.81	33.51 ± 5.16	50.25 ± 26.77
χ^2	2.25	0.56	1.96	0.53

Table 8.1: *Fit parameters for equation 8.5 for both Data and Monte Carlo corrections. The parameters (a, b, c, f, and g) for P_{tjb} corrections (R_1) are given in columns 2 and 4. The parameters for correcting y_{jb} (R_2) are listed in columns 3 and 5.*

The values of the fit parameters for both P_{tjb} and y_{jb} corrections are listed in table 8.1 (columns 2 and 3). In order to compensate for the skew of the function due to the preponderance of events at low Q^2, a minor correction to the function is applied, yielding a final form of

$$R_1(P_{tjb}, y_{jb}) = \frac{1.50 - 0.25\exp(-15.24y_{jb})}{1.38 - \exp(-0.17P^{0.89}_{tjb})} \qquad P_{tjb}\ Correction \tag{8.6}$$

for the P_{tjb} correction, and

$$R_2(P_{tjb}, y_{jb}) = \frac{3.00 - 0.59\exp(-19.62y_{jb})}{2.72 - \exp(-0.12P^{0.89}_{tjb})} \qquad y_{jb}\ Correction \tag{8.7}$$

for the y_{jb} correction. The correction functions are plotted in figures 8.3 and 8.4 which show that both functions give a maximum correction of ~ 1.25 at $P_{tjb} \sim 12\ GeV$, falling rapidly down to ~ 0.96 at low y_{jb} and very high P_{tjb}. Both corrections tend to asymptotic values of 1.08 (P_{tjb} correction) and 1.1 (y_{jb}

	Data			Monte Carlo		
P_{tjb} , y_{jb}	R_1	R_2	Q^2_{cor}/Q^2_{jb}	R_1	R_2	Q^2_{cor}/Q^2_{jb}
12 , 0.05	1.18	1.16	1.14	1.18	1.17	1.40
12 , 0.2	1.27	1.25	1.73	1.21	1.18	1.53
12 , 0.5	1.28	1.26	2.22	1.21	1.18	1.78
20 , 0.05	1.07	1.09	1.15	1.12	1.13	1.26
20 , 0.2	1.15	1.18	1.38	1.15	1.14	1.37
20 , 0.5	1.16	1.18	1.64	1.15	1.14	1.53
70 , 0.05	1.00	1.02	1.01	1.04	1.07	1.08
70 , 0.2	1.08	1.10	1.19	1.06	1.09	1.16
70 , 0.5	1.09	1.11	1.32	1.07	1.09	1.24

Table 8.2: *Comparison of R_1 and R_2 for values of P_{tjb} (in GeV) and y_{jb} for both data and Monte Carlo (columns 2, 3, 5, and 6). Columns 4 and 7 give the ratio of Q^2_{cor}/Q^2_{jb}.*

correction). Figure 8.5 shows a plot of $(Q^2 - Q^2_{DA})/Q^2_{DA}$ vs Q^2_{DA} for the two cases of $Q^2 = Q^2_{jb}$ and $Q^2 = Q^2_{cor}$ (for NC events with $Q^2_{DA} > 400$ GeV^2 and $P_{tjb} > 12$ GeV). It is seen that Q^2 bias due to the JB reconstruction is reduced.

In practice, as y_{jb} becomes closer to 1, it may be corrected to nonphysical values. No attempt is made here to adjust the corrections given above to avoid this effect. For the CC data sample, if $y_{cor} > 0.9$, then y_{jb} is used in equation (8.1) instead of y_{cor}.

8.3 Monte Carlo Correction Method

In this section, the steps that lead to the data correction of the previous section are repeated by using NC Monte Carlo events to find R_1 and R_2 (the

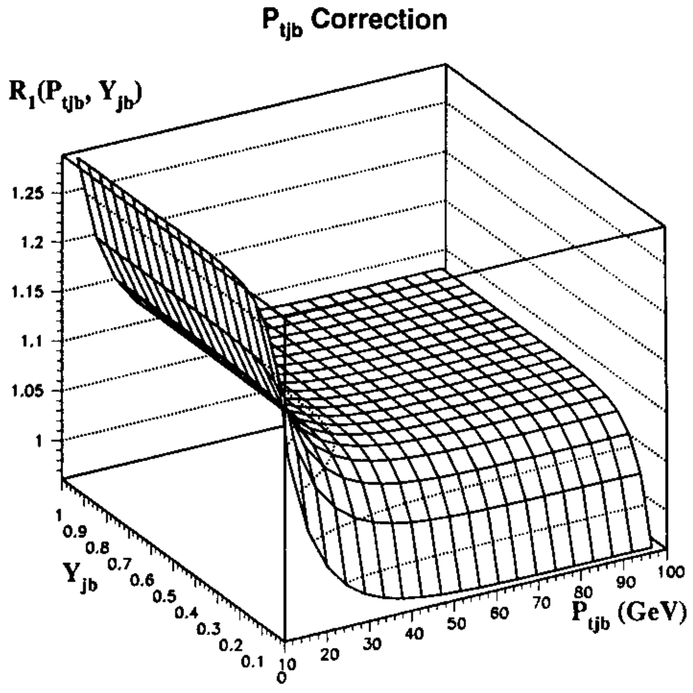

Figure 8.3: *The P_{tjb} correction used to correct the CC data. It is given by*

$$R_1(P_{tjb}, y_{jb}) = \frac{1.50-0.25\exp(-15.24y_{jb})}{1.38-\exp(-0.17P_{tjb}^{0.89})}$$

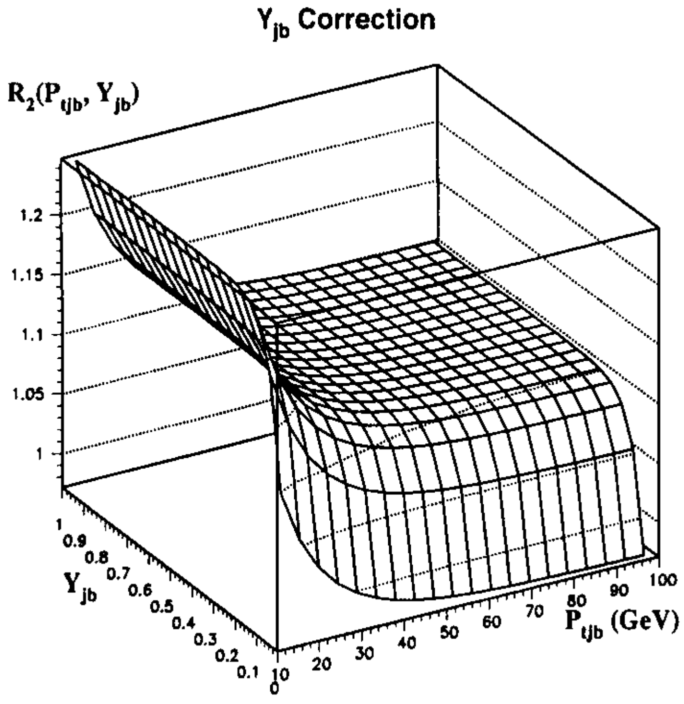

Figure 8.4: *The y_{jb} correction used to correct the CC data. The correction is*

$$R_2(P_{tjb}, y_{jb}) = \frac{3.00-0.59\exp(-19.62y_{jb})}{2.72-\exp(-0.12P_{tjb}^{0.89})}$$

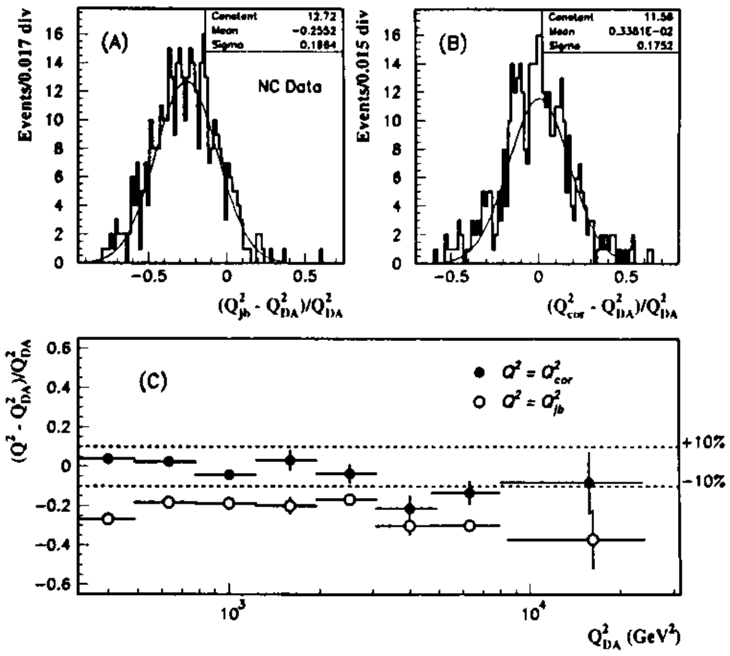

Figure 8.5: *Comparison of data correction and JB reconstruction to the DA reconstruction using NC data with $Q^2_{DA} > 400$ GeV^2 and $P_{tjb} > 12$ GeV: (A) $(Q^2_{jb} - Q^2_{DA})/Q^2_{DA}$ (B) $(Q^2_{cor} - Q^2_{DA})/Q^2_{DA}$ (C) $(Q^2 - Q^2_{DA})/Q^2_{DA}$ vs Q^2_{DA} for $Q^2 = Q^2_{jb}$ (open circles) and $Q^2 = Q^2_{DA}$ (solid circles). The last bin for the $Q^2 = Q^2_{jb}$ case is slightly shifted in order to make the vertical error bars visible.*

"Monte Carlo correction" method). The values of R_1 and R_2 obtained from the Monte Carlo correction are used to correct the CC Monte Carlo.

A sample of 6585 NC Monte Carlo events with $Q^2 > 100\ GeV^2$ is generated using the Color Dipole Model + Boson Gluon Fusion model of hadronization. The same cuts described in section 8.2.1 are used, giving 2333 NC Monte Carlo events. Equation 8.5 is minimized and the resulting values of the fit parameters are listed in table 8.1 (columns 4 and 5). As before, to compensate for the preponderance of events at low Q^2, a minor correction is applied to R_1 and R_2 giving the final forms (see equation (8.4))

$$R_1(P_{tjb}, y_{DA}) = \frac{3.62 - 0.49\exp(-33.51 y_{jb})}{3.42 - \exp(-0.1 P_{tjb}^{0.86})} \qquad P_{tjb}\ \mathit{Monte\ Carlo\ correction} \tag{8.8}$$

and

$$R_2(P_{tjb}, y_{DA}) = \frac{5.25 - 0.71\exp(-50.25 y_{jb})}{4.85 - \exp(-0.11 P_{tjb}^{0.86})} \qquad y_{tjb}\ \mathit{Monte\ Carlo\ correction} \tag{8.9}$$

Figure 8.6 compares Q^2_{jb} and the corrected $Q^2(Q^2_{cor})$ to Q^2_{DA} for events with $Q^2_{DA} > 400\ GeV^2$ and $P_{tjb} > 12\ GeV$. The bias in the JB reconstruction is reduced, with a small tail remaining.

The ratios of the data correction to the Monte Carlo correction are shown in figure 8.7 for both P_{tjb} and y_{jb}. The corrections differ from each other by at most ±6%, which occurs at $P_{tjb} = 12\ GeV$ or for $y_{jb} < 0.05$. At asymptotic values they differ by 2%. This can also be seen from table 8.2 in which R_1 and R_2 are given for values of P_{tjb} and y_{jb} (data and Monte Carlo).

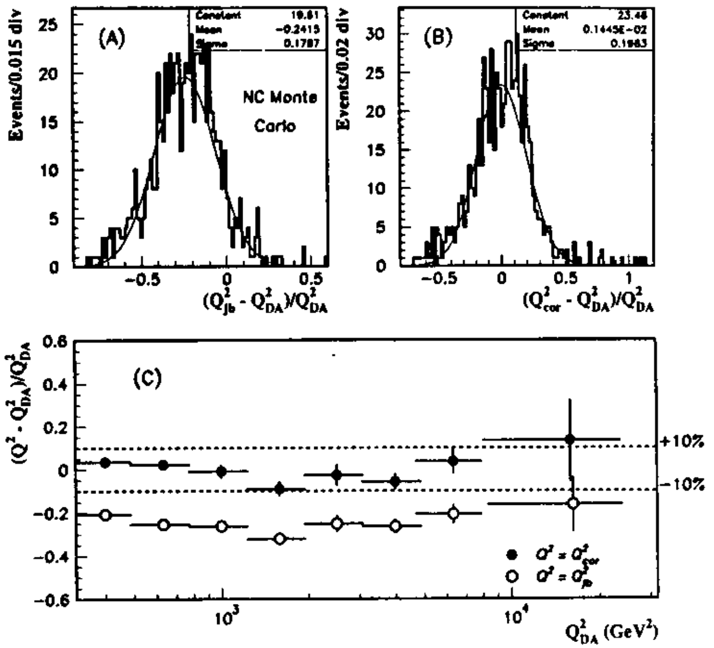

Figure 8.6: *Comparison of the Monte Carlo correction and the JB reconstruction to the DA reconstruction for NC Monte Carlo with $Q^2_{DA} > 100\ GeV^2$ and $P_{tjb} > 12\ GeV$: (A) $(Q^2_{jb} - Q^2_{DA})/Q^2_{DA}$ (B) $(Q^2_{cor} - Q^2_{DA})/Q^2_{DA}$ (C) $(Q^2 - Q^2_{DA})/Q^2_{DA}$ vs Q^2_{DA} for $Q^2 = Q^2_{jb}$ (open circles) and $Q^2 = Q^2_{DA}$ (solid circles). The last bin for the $Q^2 = Q^2_{jb}$ case is shifted in order to make the vertical error bars visible.*

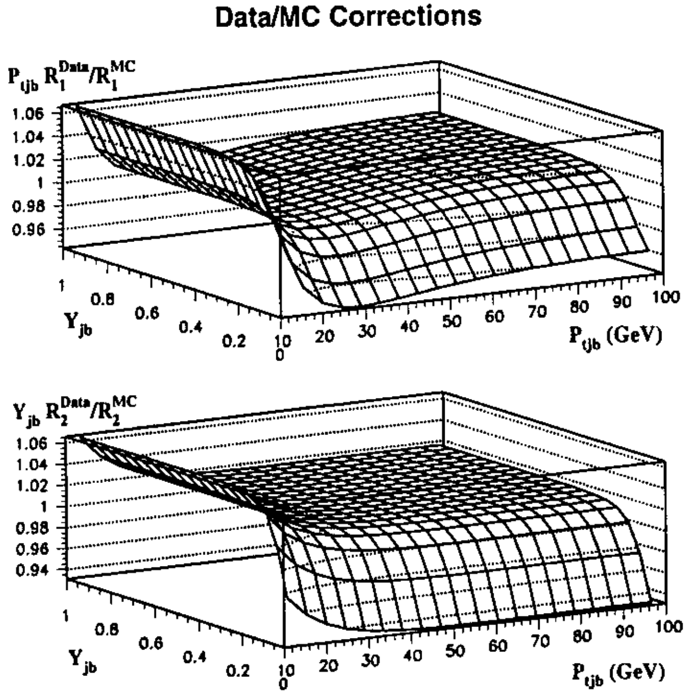

Figure 8.7: *Comparison of Data to Monte Carlo (MC) corrections for both P_{tjb} and y_{jb}. The maximum difference between the data and Monte Carlo corrections is 6% tending to an asymptotic value of 2%.*

8.4 Discussion

8.4.1 Bias Reduction and Resolution Improvement

The correction methods of sections 8.2 and 8.3 attempt to give average energy adjustments. As shown by figures 8.5(A) and 8.5(B) for the data correction (equations (8.6) and (8.7)), the mean of the distribution improves from about -25% for the $\frac{Q^2_{jb}-Q^2_{DA}}{Q^2_{DA}}$ distribution of the NC data to essentially 0% for the $\frac{Q^2_{cor}-Q^2_{DA}}{Q^2_{DA}}$ distribution. The same is true for the Monte Carlo correction of the JB variables (equations (8.8) and (8.9)) as indicated in figures 8.6(A) and 8.6(B).

From figures 8.5(C) and 8.6(C), it might be concluded that a single global scale shift, f_{scale}, is all that is needed. However, this is not the case. To see this, one can multiply Q^2_{jb} in the $\frac{Q^2_{jb}-Q^2_{DA}}{Q^2_{DA}}$ distributions of the NC data and Monte Carlo (figures 8.8(C) and 8.8(A), respectively) by $f_{scale} = 1.35$ and $f_{scale} = 1.3$, respectively, to shift the distributions to a mean of zero. As shown in figure 8.8, multiplying Q^2_{jb} by these scale factors, which results in figures 8.8(D) and 8.8(B), does correct for the shift in Q^2. However, unlike the data or the Monte Carlo correction methods, multiplying by a scale factor does not improve the sigma, σ, of the resulting distributions. Specifically, the σ of $\frac{f_{scale}Q^2_{jb}-Q^2_{DA}}{Q^2_{DA}}$ is larger when compared to the σ of the original $\frac{Q^2_{jb}-Q^2_{DA}}{Q^2_{DA}}$ distribution for NC data or Monte Carlo. σ is taken to be the width of the gaussian fits for the $\frac{Q^2_{jb}-Q^2_{DA}}{Q^2_{DA}}$ distributions or for the resulting distributions, $\frac{f_{scale}Q^2_{jb}-Q^2_{DA}}{Q^2_{DA}}$. For the NC data shown in figures 8.8(C) and 8.8(D), σ changes from 19.6% for the $\frac{Q^2_{jb}-Q^2_{DA}}{Q^2_{DA}}$ distribution to 28.6% for the $\frac{1.35Q^2_{jb}-Q^2_{DA}}{Q^2_{DA}}$ distribution. Going back to figure 8.5(B), it is seen that the data correction given by equations (8.6) and (8.7) results in $\sigma = 17.5\%$ for the NC $\frac{Q^2_{cor}-Q^2_{DA}}{Q^2_{DA}}$ distribution. Therefore, the data correction gives an improvement in σ when compared to the scale shift $f_{scale} = 1.35$ by a factor of $(28.6 - 17.5)/28.6 = 0.39$.

For NC Monte Carlo, σ changes from 17.8% for the $\frac{Q^2_{jb}-Q^2_{DA}}{Q^2_{DA}}$ distribution to 22.7% for the $\frac{1.3Q^2_{jb}-Q^2_{DA}}{Q^2_{DA}}$ distribution. The result of Monte Carlo correction (equations (8.8) and (8.9)), shown in figures 8.6(A) and 8.6(B), gives σ = 19.6%, yielding an improvement in σ when compared to the scale shift $f_{scale} = 1.3$ by a factor of $(22.7 - 19.6)/22.7 = 0.14$.

Therefore, correcting the data, or Monte Carlo, by a simple scale factor is not enough. One needs to correct the event energies first (P_{tjb} and y_{jb} in this analysis) by a more detailed correction scheme, such as the method described above.

8.4.2 Application to CC Monte Carlo

To compare the relative effects of the data and Monte Carlo corrections on CC Monte Carlo events, both corrections are applied separately to the CC Monte Carlo sample. This sample consists of 7822 generated events with true $Q^2_t > 100\ GeV^2$, of which 5928 events pass the CC selection cuts. The events are distributed in the Q^2_t bins shown in table 8.3 before and after cuts (these are the same bins used for $d\sigma/dQ^2$ measurements—section 7.3). Table 8.3 also shows the same for NC Monte Carlo for comparison. In figure 8.9, $(Q^2_{cor} - Q_t)/Q^2_t$ for both data and Monte Carlo corrections is plotted vs Q^2_t. With the exception of $Q^2_t \geq 35000\ GeV^2$, the Monte Carlo correction is slightly smaller than the data correction, reflecting greater energy loss in the data compared to the Monte Carlo. In figure 8.9, the two correction methods are compared to the

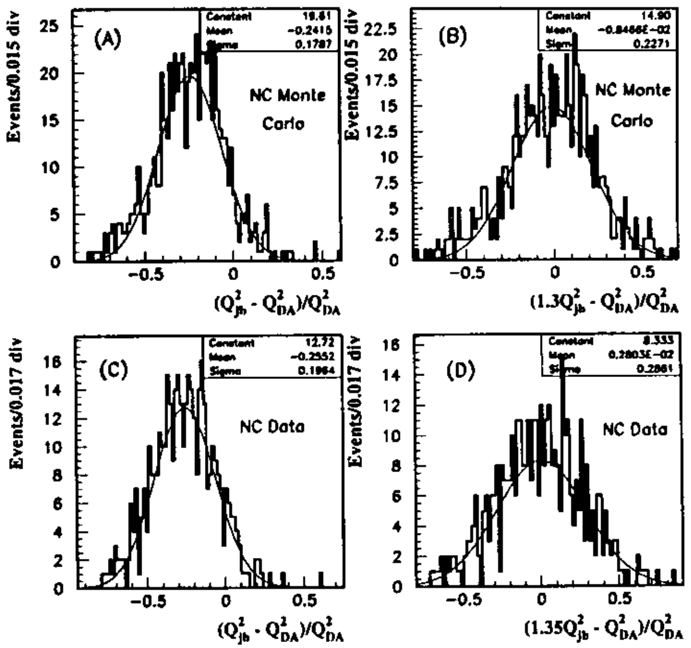

Figure 8.8: *Effects of multiplying Q^2_{jb} by a scale factor f_{scale}. Events shown in this figure have $Q^2_{DA} > 100\ GeV^2$ and $P_{tjb} > 12\ GeV$. Figures (A) and (B) show the effect of multiplying Q^2_{jb} by $f_{scale} = 1.3$ for NC Monte Carlo events. Figures (C) and (D) show the same effect for NC data, where $f_{scale} = 1.35$.*

	Q_t^2 Bins (GeV^2)				
	400-1000	1000-2500	2500-6250	6250-15625	> 15625
# CC events (no cuts)	1965	2470	2180	1012	195
# CC events (cuts)	1157	1837	1834	922	178
ϵ(CC)	0.59	0.74	0.84	0.91	0.91
# NC events (no cuts)	1840	2281	554	98	14
# NC events (cuts)	1476	1880	460	80	12
ϵ(NC)	0.80	0.82	0.83	0.82	0.86

Table 8.3: *Number of CC(NC) Monte Carlo events generated before and after passing CC(NC) selection cuts in each of the five Q_t^2 bins considered for cross section measurements. The 3rd(6th) row gives the efficiency due to the cuts.*

JB reconstruction of the CC Monte Carlo events to illustrate the improvement attained by these corrections.

As mentioned in section 8.1, the purpose of correcting for energy loss is to minimize event migration. Since the JB reconstruction of kinematic variables underestimates the reconstructed Q^2, event migrations to lower Q^2 bins are expected to be large. Correcting the reconstructed energies, and, therefore, the reconstructed Q^2, reduces the bin to bin migrations. To see this reduction, the Q^2 of the CC Monte Carlo events is reconstructed with both the JB reconstruction method (Q^2_{jb}) and the Monte Carlo correction method of section 8.3 (Q^2_{cor}). The effects of reconstruction on the event migration is shown in the two "smearing" matrices below, where a smearing matrix quantifies how many events are smeared (or migrate) from one bin to another. The left matrix shows the effect of the JB reconstruction on CC migration and the

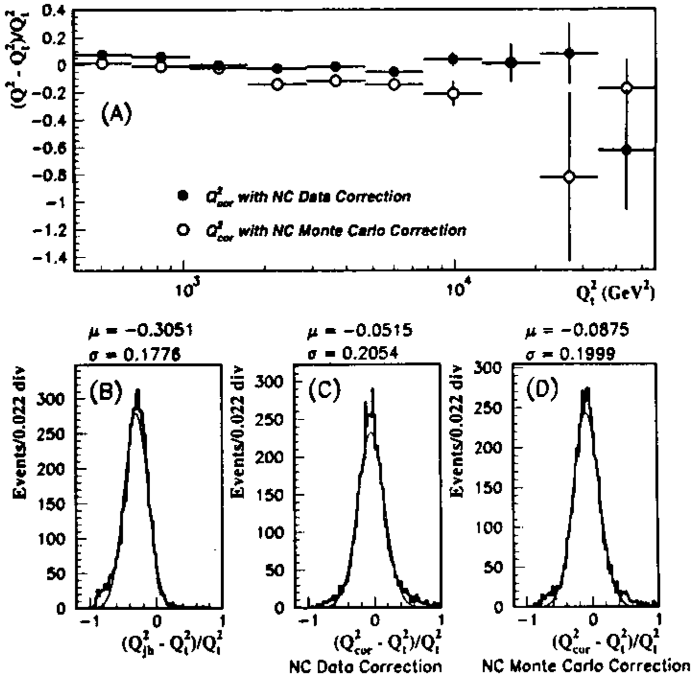

Figure 8.9: *Effect of correction on CC Monte Carlo: (A) Data and Monte Carlo corrections (solid and open circles, respectivley) are applied to the CC Monte Carlo and are compared to the true Q_t^2 (B) $(Q^2_{jb} - Q^2_t)/Q^2_t$ (C) $(Q^2_{cor} - Q^2_t)/Q^2_t$ after applying the data correction (D) $(Q^2_{cor} - Q^2_t)/Q^2_t$ after applying the Monte Carlo correction.*

right matrix gives the effect of the Monte Carlo correction. The left matrix below shows where the CC Monte Carlo events, generated in the true Q_t^2 bin and passing the selection cuts, end up after reconstructing Q_{jb}^2 for the JB reconstruction. The right matrix does the same but uses the corrected Q_{cor}^2 for bin assignments after applying the Monte Carlo correction. The columns of each matrix indicate the Q_t^2 bins. The rows of the left and right matrices indicate the Q_{jb}^2 and Q_{cor}^2 bins after the JB reconstruction and using the Monte Carlo correction, respectively. For example, from a total of 1157 events generated with $400 < Q_t^2 < 1000\ GeV^2$ and passing the CC selection cuts (table 8.3), 740 events end up with $400 < Q_{jb}^2 < 1000\ GeV^2$, 4 events with $1000 < Q_{jb}^2 < 2500\ GeV^2$, 0 events with $Q_{jb}^2 > 2500\ GeV^2$, ...etc.

$$\begin{array}{cccc} & Q_t^2 \rightarrow & & Q_t^2 \rightarrow \\ Q_{jb}^2 \downarrow & \begin{pmatrix} 740 & 727 & 92 & 20 & 1 \\ 4 & 1070 & 741 & 57 & 11 \\ 0 & 13 & 990 & 417 & 14 \\ 0 & 0 & 7 & 427 & 106 \\ 0 & 0 & 0 & 1 & 46 \end{pmatrix} & Q_{cor}^2 \downarrow & \begin{pmatrix} 974 & 212 & 20 & 1 & 0 \\ 95 & 1505 & 381 & 36 & 3 \\ 1 & 88 & 1347 & 235 & 12 \\ 0 & 0 & 85 & 615 & 65 \\ 0 & 0 & 1 & 35 & 98 \end{pmatrix} \end{array}$$

Comparing the two matrices, it is clear that there is a substantial reduction in the event bin to bin migration from using the Q_{cor}^2 instead of Q_{jb}^2 reconstruction. To find the percent improvement in reducing the bin to bin migration of the CC Monte Carlo events, each column of the above two matrices is divided by the number of generated events that pass CC selection cuts given in table 8.3. Therefore, the first column is divided by 1157, and so on. The results

are given in the following two matrices

$$\begin{array}{cc} & Q_t^2 \rightarrow \\ Q_{jb}^2 \downarrow & \begin{pmatrix} 0.64 & 0.40 & 0.05 & 0.02 & 0.01 \\ 0.0 & 0.58 & 0.40 & 0.06 & 0.06 \\ 0.0 & 0.01 & 0.54 & 0.45 & 0.08 \\ 0.0 & 0.0 & 0.0 & 0.46 & 0.60 \\ 0.0 & 0.0 & 0.0 & 0.0 & 0.26 \end{pmatrix} \\ Q_{cor}^2 \downarrow & \begin{pmatrix} 0.84 & 0.13 & 0.01 & 0.0 & 0.0 \\ 0.08 & 0.82 & 0.21 & 0.04 & 0.02 \\ 0.0 & 0.05 & 0.73 & 0.25 & 0.07 \\ 0.0 & 0.0 & 0.05 & 0.67 & 0.37 \\ 0.0 & 0.0 & 0.0 & 0.04 & 0.55 \end{pmatrix} \end{array}$$

Each element of the above two matrices is the fraction of the generated CC Monte Carlo events that pass CC selection and are reconstructed in the bin. In the following, the top matrix is called the jb–matrix and the bottom matrix is called the cor–matrix. The jb–matrix has its diagonal elements with values between 0.26–0.64 (average ~ 0.5). All its lower off-diagonal elements are close to zero while the upper off-diagonal elements are comparable to the diagonal ones. This reflects the fact that when the calorimeter is used to measure event energies, the JB reconstruction underestimates Q^2. The cor-matrix has diagonal elements that range between 0.55–0.84 (average ~ 0.72) and are 44% higher on average than the jb-matrix diagonal elements. The cor–matrix lower off-diagonal elements are between 0.04–0.08 and are more symmetric about the diagonal than the jb-matrix. This indicates that the Monte Carlo correction method eliminates much of the bias towards lower Q^2 values present in the

JB reconstruction and it lessens the bin to bin migration. However, there still remain some bias toward lower Q^2 after using the Monte Carlo correction on the CC Monte Carlo events, since the the upper off–diagonal elements of the cor–matrix are larger than the lower off–diagonal elements.

Note that the addition of the elements in each column of the jb–matrix and the cor–matrix does not result in 1.0 in some of the columns because some of the CC Monte Carlo events are reconstructed (corrected) in the $Q_t^2 < 400\ GeV^2$ bin.

Since we are correcting the JB variables back to their DA values, the predictions of the DA reconstruction are treated as the true predictions (section 8.1). From these predictions, the Monte Carlo correction is obtained. Therefore, one needs to compare the CC Monte Carlo event migration, after the Monte Carlo correction is applied to the CC Monte Carlo, to the NC Monte Carlo event migration after reconstruction with the DA reconstruction method. The cor–matrix obtained above compared the corresponding smearing matrix of the NC Monte Carlo events reconstructed with the DA variables, which is

$$\begin{array}{cc} & Q_t^2 \rightarrow \\ Q_{DA}^2 \downarrow & \left(\begin{array}{ccccc} 0.95 & 0.04 & 0.02 & 0.04 & 0.0 \\ 0.01 & 0.94 & 0.06 & 0.0 & 0.0 \\ 0.0 & 0.0 & 0.87 & 0.06 & 0.0 \\ 0.0 & 0.0 & 0.01 & 0.84 & 0.17 \\ 0.0 & 0.0 & 0.0 & 0.0 & 0.83 \end{array} \right) \end{array}$$

As expected, the bin to bin event migration is less when the DA reconstruction is used because the DA reconstruction is largely energy independent (see equation (6.5)).

Q^2 Bin (GeV^2)	$A(Q^2_{jb})$	$A(Q^2_{cor})$
400-1000	0.81	0.67
1000-2500	0.76	0.82
2500-6250	0.65	0.77
6250-15625	0.43	0.76
> 15625	0.24	0.69

Table 8.4: *Acceptance, A_{CC}, as a function of reconstructed Q^2 for the five Q_t^2 bins used in the cross section measurements. A is the ratio of the number of events passing all cuts that have reconstructed Q^2 (Q^2_{jb} or Q^2_{cor}) in the bin to the total number of events generated with Q_t^2 in the bin.*

The acceptance (chapter 7), A_{CC}, of each Q^2_{cor} bin is found after applying the Monte Carlo correction to the CC Monte Carlo events. The results are tabulated in table 8.4, which gives A_{CC} as a function of Q^2_{cor} for the five Q^2_{cor} bins. For comparison, table 8.4 also shows A_{CC}, after the reconstructing the CC Monte Carlo events with the JB reconstruction method, as a function of Q^2_{jb}. As is seen from table 8.4, $A_{CC}(Q^2_{cor})$ is relatively flat versus Q^2_{cor}, with an average of 0.74, while $A_{CC}(Q^2_{jb})$ decreases from 0.81 down to 0.24.

Table 8.5 shows the purity of each Q^2 bin. Purity is defined as the ratio of the number of generated events in the bin that pass selection cuts with Q^2 reconstructed in the bin to the total number of events passing cuts that have Q^2 reconstructed in the bin. The purity for the three lowest Q^2 bins is higher for the Monte Carlo correction method. Although the purity using the JB reconstruction is comparable to the one obtained from the Monte Carlo correction method in the highest two Q^2 bins (it is 0.98 for the highest Q^2_{jb} bin), it should be noted that the acceptances for these two bins with the JB

Q^2 Bin	Purity	
(GeV^2)	JB	Cor
400-1000	0.47	0.74
1000-2500	0.57	0.75
2500-6250	0.69	0.80
6250-15625	0.79	0.80
> 15625	0.98	0.70

Table 8.5: *Purity due to JB reconstruction and Monte Carlo correction method. Purity is defined as as the ratio of the number of generated events in the bin that pass selection cuts with Q^2 reconstructed in the bin to the number of events passing cuts that have Q^2 reconstructed in the bin.*

reconstruction are low (0.43 and 0.24—table 8.4).

For comparison with the DA reconstruction of the NC Monte Carlo, the NC bin acceptance, $\mathcal{A}_{NC}$, and bin purity are given in table 8.6.

8.5 Summary

In this chapter, a hadronic energy correction method that uses NC data and NC Monte Carlo is presented. The data and Monte Carlo corrections improve the bias and resolution for reconstructed Q^2 on an event by event basis, when compared to the JB reconstruction of kinematic variables. When the Monte Carlo correction is applied to the CC Monte Carlo, the event bin to bin migration is reduced, Q^2–dependence of bin acceptances are reduced, and bin purities are enhanced. There is still some bias toward lower Q^2 values present in the correction, which might be improved with a larger NC data sample that fits more closely the dependence of the correction at large $P_{t_{jb}}$.

Q^2 Bin	Purity	$\mathcal{A}_{NC}$
(GeV^2)	DA	DA
400-1000	0.91	0.83
1000-2500	0.94	0.82
2500-6250	0.96	0.75
6250-15625	0.89	0.77
> 15625	1.00	0.71

Table 8.6: *NC events purity (first column), due to the DA reconstruction, and bin acceptance.*

For $0.1 < y_{jb} < 0.3$, the Q^2 data and Monte Carlo correction factors (equation 8.1) agree within 1%; but, for high y_{jb} (low y_{jb}), the data correction is up to 30% larger (smaller) than the Monte Carlo Q^2 correction (table 8.2).

To find the cross sections, the measured $P_{t_{jb}}$ and y_{jb} of the CC data are corrected with the NC data correction (equations (8.6) and (8.7)), while $P_{t_{jb}}$ and y_{jb} of the CC Monte Carlo events are corrected with the Monte Carlo correction (equations (8.8) and (8.9)). The resulting Q^2_{cor} is obtained from the corrected kinematics using equation (8.1).

Chapter 9

CROSS SECTION MEASUREMENTS AND $R(\sigma_{NC}/\sigma_{CC})$

In this chapter, the measured NC and CC cross sections and cross section ratios are given in section 9.1. The error analysis on the cross section measurements is detailed in section 9.2. Finally, section 9.3 gives the final cross section measurements, after all errors are evaluated.

9.1 Bin Acceptance and Cross Sections

The NC and CC cross sections are measured in five Q^2 bins. They are $400\ GeV^2 < Q^2 < 1000\ GeV^2$, $1000\ GeV^2 < Q^2 < 2500\ GeV^2$, $2500\ GeV^2 < Q^2 < 6250\ GeV^2$, $6250\ GeV^2 < Q^2 < 15625\ GeV^2$, and $Q^2 > 15625\ GeV^2$. The cross sections are found according to equation (7.1). The NC and CC bin acceptances are listed in tables 8.6 and 8.4, respectively. The acceptances are also listed in table 9.1. In addition, table 9.1 shows the measured cross sections with statistical errors. For bins with observed number of data events more than 9, the statistical error is taken as the square root of the observed number of data events. For the rest of the bins, the error is taken as the 68% confidence limit with the measured cross section being the mean of the Poisson distribution.

Q^2_{min}, Q^2_{max} (GeV^2)	400,1000	1000,2500	2500,6250	6250,15625	15625,87500
N_{NC}	328	86	18	3	1
A_{NC}	0.83	0.82	0.75	0.77	0.71
σ_{NC}	732 ± 40	194 ± 21	44 ± 10	$7.2^{+1.6}_{-4.0}$	$2.6^{+3.4}_{-2.2}$
N_{CC}	2	7	5	7	2
A_{CC}	0.67	0.82	0.77	0.76	0.69
σ_{CC}	$5.5^{+4.6}_{-3.5}$	$15.8^{+6.3}_{-5.8}$	$12.0^{+5.7}_{-5.2}$	$17.1^{+6.7}_{-6.3}$	$5.3^{+4.6}_{-1.9}$
	$87500\ GeV^2 > Q^2 > Q^2_{min}$				
A_{NC}	0.82	0.81	0.75	0.76	0.71
σ_{NC}	979 ± 47	247 ± 24	54 ± 11.5	$9.7^{+5.4}_{-4.6}$	$2.6^{+3.4}_{-2.2}$
A_{CC}	0.76	0.79	0.76	0.74	0.69
σ_{CC}	56 ± 11.7	49 ± 10.7	34 ± 9.1	22.5 ± 7.5	$5.3^{+4.5}_{-1.9}$

Table 9.1: *NC and CC cross sections, $\sigma_{NC,CC}$. $N_{NC,CC}$ is the number of observed events and $A_{NC,CC}$ is the bin acceptance. Errors on $\sigma_{NC,CC}$ are statistical only. Also shown are $\sigma_{NC,CC}$ for $87500\ GeV^2 Q^2 > Q^2_{min}$.*

9.2 Systematics Errors

Three sources contribute to the systematic errors. The first (type I) is the uncertainty in the luminosity measurement of ±2.5%.[18] The second source (type II) comes from the difference in calorimeter energy scale between the Monte Carlo and the data. To find the systematic error due to this effect, the relevant cuts have to be scaled by a factor. The cuts are then applied to Monte Carlo only and the cross sections are calculated after applying the cuts. The third source of error (type III) is produced when the shapes of the Monte

Systematic Error Source	Q^2 bin (GeV^2)				
	400–1000	1000–2500	2500–6250	6250–15625	> 15625
e^- Scale†	2.5	1.5	2.0	1.5	0.0
H. Scale‡	2.5	2.5	2.0	1.5	0.0
$E - P_z$	1.0	1.5	0.0	0.0	0.0
y_e	0.0	1.5	1.8	1.8	1.8
E_e'	1.5	1.5	0.0	0.0	0.0
$p_t/\sqrt{E_t}$	1.2	0.0	0.0	0.0	0.0
Q_e^2/Q_{DA}^2	0.0	5.6	0.0	0.0	0.0
CTDtrk, iso RCALbp	1.0	1.0	1.0	1.0	1.0
e^- Finder	5.0	2.0	2.0	2.0	2.0
CDMBGF vs MEPS	5.0	10.0	10.0	10.0	10.0
Luminosity	2.5	2.5	2.5	2.5	2.5
Total Error	8.5	12.5	11.0	10.9	10.7

†e^- Scale = electron energy scale, ‡H. Scale = hadronic energy scale

Table 9.2: *Percent systematic errors on the NC measured cross sections due to various sources. The errors are given in percent and are added in quadrature to give the total error.*

Carlo distributions are different from data distributions, assuming there is no energy scale factor between the two. For this type of error, the cuts are varied in *both* Monte Carlo and in data and the cross sections are recalculated.

9.2.1 NC Systematic Errors

Systematic errors on the NC cross sections are discussed in this section. Table 9.2 summarizes the NC systematic errors. There are two sources of calorimeter energy scale systematic error (type II). The first source is the 6% difference between NC Monte Carlo predictions and NC data for the scattered electron energy, as mentioned in section 7.1 (see figures 7.6 and 7.7). This difference is due to incomplete simulation of the inactive material in front of the calorimeter. Multiplying the scattered electron energy and the relevant selection cuts that use this energy (E_e', y_e, $E - P_z$, and Q_e^2/Q_{DA}^2) in NC Monte Carlo by 0.94, the cross sections increase by 2.5%, 1.5%, 2%, 1.5%, and 0% from lowest to highest Q^2 bin. The percent increase of the cross sections in the bins show some fluctuations due to Monte Carlo statistics. As a result, the error assigned to the electron energy scale is 3% for all the bins.

The second source of calorimeter energy scale error is the hadronic energy scale. Figure 9.1(A) compares the *hadronic* $E - P_z$ spectra of NC Monte Carlo to NC data, showing that there maybe some difference in shape. The shift in hadronic energy scale is estimated to be 10% from the resolution obtained by comparing the hadronic true p_t^{true} to the reconstructed hadronic $P_{t,h}$, as shown in figure 9.1(B), using the NC Monte Carlo events. Varying the hadronic energy by ±10%, the changes to the cross sections are a 2.5% increase for the lowest two Q^2 bins, 2% increase for the next bin, 1.5% decrease for the fourth bin, and none for the highest bin. Therefore, the errors assigned due to hadronic energy scale are 2.5%, 2.5%, 2%, 1.5%, and 0% for the lowest to highest Q^2 bins.

Another systematic error is caused by differences between NC data and NC Monte Carlo not due to an energy scale difference (type III). For this type of error, the three highest Q^2 bins are combined into one bin with $Q^2 >$ 2500 GeV^2. In the highest three Q^2 bins, losing an event in any one bin may introduce large statistical errors, rendering the estimate of the error inaccurate, since the measured statistics in each of these bins is small. Combining the three bins enables us to utilize all 22 remaining events in these bins. When these

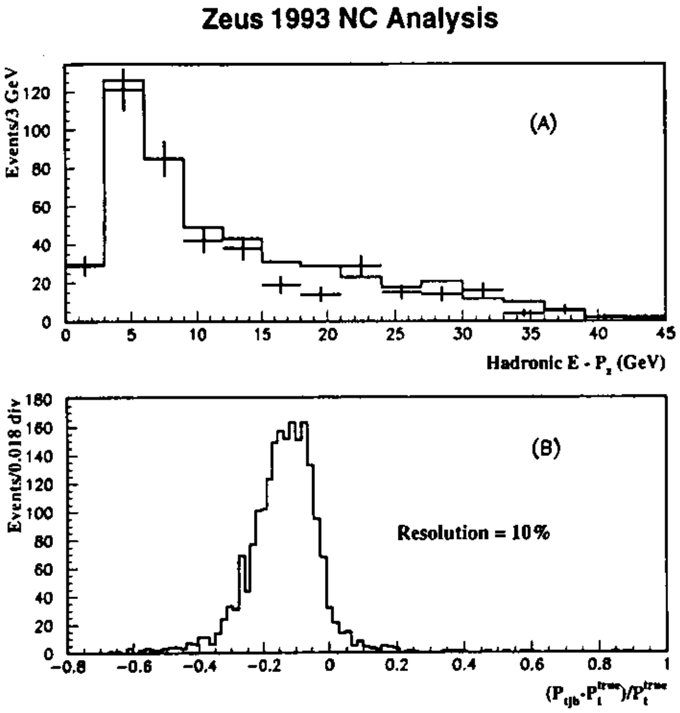

Figure 9.1: *(A) Comparison of the hadronic* $E - P_z$ *for the final 436 NC candidates (histogram with error bars) and NC Monte Carlo (solid histogram).* E *is the total hadronic energy and* P_z *is the total hadronic longitudinal energy (B)* $(P_{tjb} - p_t^{true})/p_t^{true}$ *for NC Monte Carlo events with NC selection cuts, where* P_{tjb} *is the hadronic jet measured transverse momentum and* p_t^{true} *is its true transverse momentum.*

bins are combined, the statistical error is reduced since the loss of an event or two due to cut variation does not introduce unrealistically large errors. The errors determined in this manner are assumed to be applicable to all of the three highest Q^2 bins. Unless otherwise stated, the three highest Q^2 bins are combined into the "highest bin" in the following. Possible sources of the type III systematic errors are:

- $E - P_z$: The NC Monte Carlo is generally 2 GeV higher on average than the data in all bins (figure 7.5). Increasing the $E - P_z$ cut by 2 GeV in the first Q^2 bin does not change the bin acceptance. However, the number of NC data events is decreased from 328 to 325, resulting in a 1% decrease in the cross section. When $E - P_z$ is increased by 2 GeV in the second Q^2 bin, the bin acceptance is decreased from 0.83 to 0.81. The number of NC data events stays the same (86 events), giving an increase of 1.5% in the cross section. For the highest Q^2 bin, the bin acceptance and the number of NC data events stay the same when $E - P_z$ is increased by 2 GeV. Decreasing the $E - P_z$ cut by 2 GeV leaves the bin acceptance and number of data events in each Q^2 bin unchanged. Therefore, the errors assigned due to the $E - P_z$ cut are 1%, 1.5%, and 0% in the lowest Q^2 bin, second bin, and highest bin.

- y_e: The NC Monte Carlo predicts higher values of y_e on average, as seen from figure 7.5. The difference in the mean of the distribution of y_e between data and Monte Carlo is 0.03 in the lowest bin, 0.08 in the second bin, and zero in the highest bin. However, the resolution is 0.074 in all the bins, as determined from the rms value of the $y_e - y_{true}$ distribution, shown in figure 9.2. Therefore, the y_e cut is varied by 0.1 unit in all the bins. Decresing this cut by 0.1 in the lowest Q^2 bin leaves the bin acceptance and number of NC data events unchanged. Decreasing the cut by 0.1 in the second Q^2 bin decreases the bin acceptance from 0.82 to 0.79, while number of NC data events is decreased from 86 to 84 events, resulting in 1.5% increase in the cross section. Decreasing the cut in the highest Q^2 bin decreases the bin acceptance from 0.75 to 0.7 . The number of NC data events decreases from 22 to 20 events, yielding a 1.8% increase in the cross section. Increasing the cut in all the bins has no effect on the cross sections. Therefore, the errors assigned are (from lowest to highest Q^2 bin) 0%, 1.5%, and 1.8%.

- E'_e: Figure 7.6 shows that the NC Monte Carlo predicts higher E'_e than is measured from the data on average. The rms value for $E'_e - E'_{true}$ is shown in figure 9.3 for NC Monte Carlo events passing NC selection cuts. For the lowest Q^2 bin, the NC Monte Carlo predicts higher energy by 1 GeV on average. Comparison of E'_e with E'_{true} shows that the rms of the distribution of their difference is 2 GeV in this bin. Therefore, the E'_e cut is varied by ±2 GeV. Decreasing the cut by 2 GeV increases the lowest Q^2 bin acceptance from 0.83 to 0.85. The number of NC data events is increased from 328 to 331 events, resulting in a 1.5% decrease in the cross section. However, increasing the cut by 2 GeV in the bin decreases the acceptance to 0.81 and the number of NC data events to 320, yielding no change in the cross section.

In the second Q^2 bin, the NC Monte Carlo is 2.5 GeV higher than the

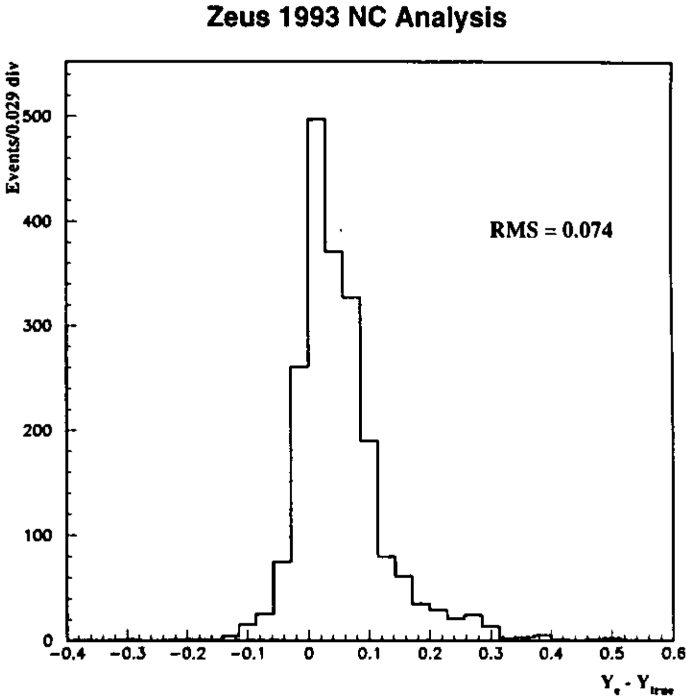

Figure 9.2: *$y_e - y_{true}$ for NC Monte Carlo events passing the NC selection cuts.*

NC data on average with the $E'_e - E'_{true}$ distribution rms of 2.4 GeV. Decreasing the E'_e cut by 2.4 GeV leaves both the acceptance and the number of NC data unchanged. Increasing the cut by 2.4 GeV decreases the acceptance from 0.82 to 0.81, while leaving the number of NC data events the same, giving an increase of 1.5% in the cross section.

For the highest Q^2 bin, mean of the NC Monte Carlo distribution is 1 GeV lower than that of the NC data. However, the $E'_e - E'_{true}$ distribution rms is 4 GeV. Varying the cut by ±4 GeV does not change either the acceptance or the number of NC data events.

Therefore, the errors assigned due to this cut are (from lowest to highest Q^2 bins) 1.5%, 1.5%, and 0%.

- $p_t/\sqrt{E_t}$: This cut is varied by 0.1 in the lowest 2 Q^2 bins and 0.2 in the highest bin. These values correspond to the shift in the mean between data and Monte Carlo. Decreasing the cut by 0.1(0.2) in the two lowest Q^2 bins (highest Q^2 bin) does not change either the number of NC data events or the bin acceptance remain unchanged.

  Increasing the cut from 2.0 to 2.1 in the first Q^2 bin increases the acceptance from 0.83 to 0.84, while leaving the number of NC data events unchanged, resulting in 1.2% decrease in the cross section. For the rest of the Q^2 bins, increasing the cut to 2.1 doeas not produce any change in the bin acceptance and the number of NC data events.

  Therefore, the errors assigned due to this cut are 1.2% in the lowest Q^2 bin and 0% for the rest of the bins.

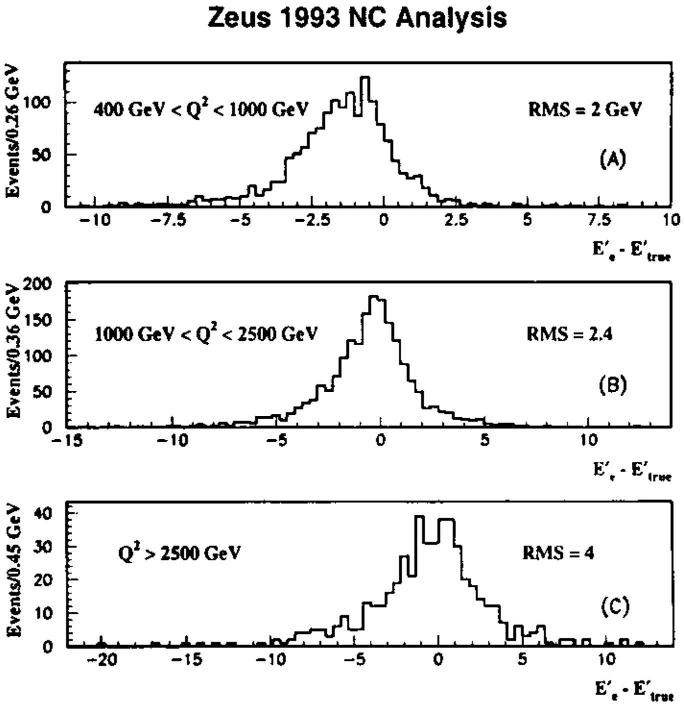

Figure 9.3: $E'_e - E'_{true}$ *distributions for NC Monte Carlo events passing NC selection cuts.* E'_e *is the measured scattered electron energy and* E'_{true} *is the true scattered electron energy.*

- Q^2_e/Q^2_{DA}: Removing this cut in the lowest Q^2 bin increases the acceptance from 0.83 to 0.84. The number of NC data events is also increased to 333 events, yielding a 0.3% increase in the cross section. When this cut is removed for the second Q^2 bin, the acceptance is increased from 0.82 to 0.83. The number of data events also increases from 86 to 92 events, resulting in 5.6% increase in the cross section. For the highest Q^2 bin, removing the cut increases the acceptance from 0.75 to 0.76. The number of NC data events stays the same, giving a 1.3% increase in the cross section.

  Therefore, the errors assigned to the cross section are (from lowest to highest Q^2 bin) 0%, 5.6%, and 0%. Note that no error is assigned to the highest Q^2 bin even though the change in the cross section is 1%. The reason is that removing the cut is in itself a rather large change, which results in a small variation in the cross section in the highest bin.

- CTDtrk, iso, RCALbp: For this cut, all the bins are combined into a single $Q^2 > 400$ GeV^2 bin. Removing this cut from data and Monte Carlo results in a 1% increase in the bin acceptance. The number of NC data events increases from 436 to 443, resulting in a 1% increase in the cross section. Therefore, a 1% error is assigned to all bins due to this cut.

- Electron finding algorithm: ELEC5[40] is used as the default electron finder in this analysis. We use Sinistra[41] instead of ELEC5 to find the effect on the cross section due to the electron finder. Using the Sinistra[41] finder for the first Q^2 bin leaves the acceptance unchanged. The number of NC data events is reduced from 328 to 313, resulting in 5% decrease in the cross section. In the second Q^2 bin, Sinistra decreases the number of NC data events from 86 to 82. The acceptance is reduced from 0.82 to 0.80, yielding a decrease of 2% in the cross section. Using Sinistra in the highest Q^2 bin reduces the acceptance from 0.75 to 0.74 with the number of NC data events remaining the same (22 events), giving an increase of 2% in the cross section.

  Therefore, the errors assigned due to electron finder are (from lowest to highest Q^2 bins) 5%, 2%, and 2%.

- Sensitivity to structure functions: NC Monte Carlo events are generated with the MRSD$'_-$ [45] set of structure functions. To quantify the dependence of the measured cross sections on various structure functions, the MRSD0,[45] CTEQ,[46] and GRV[47] sets are used. The NC Monte Carlo events are reweighted with the ratio of these sets to MRSD$'_-$. The obtained cross sections differ by less than 1% from the values given in table 9.1. Therefore, no error is assigned due to structure functions.

- Sensitivity to final state models and fragmentation: Two different final state and fragmentation models are considered. One is the Color Dipole and Boson Gluon Fusion (CDMBGF) model used by the ARIADNE 4.0[38] Monte Carlo generator. The other is the Matrix Elements Parton Shower (MEPS) used by the LEPTO 6.1[34] Monte Carlo generator. Figure 9.4 shows the acceptances using the 2 fragmentation models. The MEPS model gives acceptances that are larger by ~ 10% than the CDMBGF model. For large Q^2 bins, the difference is small compared to the statistics of the Monte Carlo events. To check if this difference in acceptance between the two models is due to one or more of the selection cuts, the efficiency of each cut is shown for the two models in figure 9.5. The figure shows that no individual cut causes more of efficiency differences than any other cut. Therefore, it is the combination of all cuts that contributes to the 10% difference in acceptance between the two models. The 10% error is assigned for the highest four Q^2 bins. In the lowest bin, an average of both final state models is used to find the bin acceptance, A_{NC}, given in table 9.1. Therefore, an error of 5% is assigned to the lowest Q^2 bin.

- Effect of trigger efficiency: For NC events, a high energy scattered electron is required in the NC selection ($E'_e > 10$ GeV), which is higher than the thresholds used to trigger the events (section 5.3.4). Therefore, the trigger effect on the NC events is estimated to be less than a percent for all of the bins.

9.2.2 CC Systematics Errors

Systematic errors on the CC measured cross sections are detailed in this section. Table 9.3 summarizes the CC systematics. In the CC cross sections, the energy scale difference (type II error) between the Monte Carlo and data affects the $p_{tmiss} > 12$ GeV cut. As is pointed out in the above section, the hadronic energy scale differs between NC data and Monte Carlo by 10%. This is shown in figure 9.1(B), where the hadronic P_{tjb} in the NC Monte Carlo is compared with the data. Changing the p_{tmiss} by ±10% results in changes of

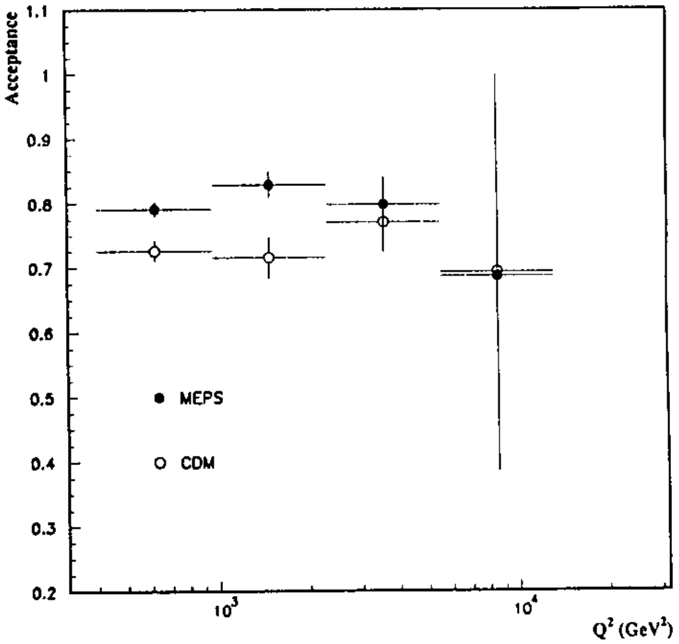

Figure 9.4: *Acceptance as a function of Q^2 for MEPS and CDMBGF hadronization models. Vertical bars are statistical errors.*

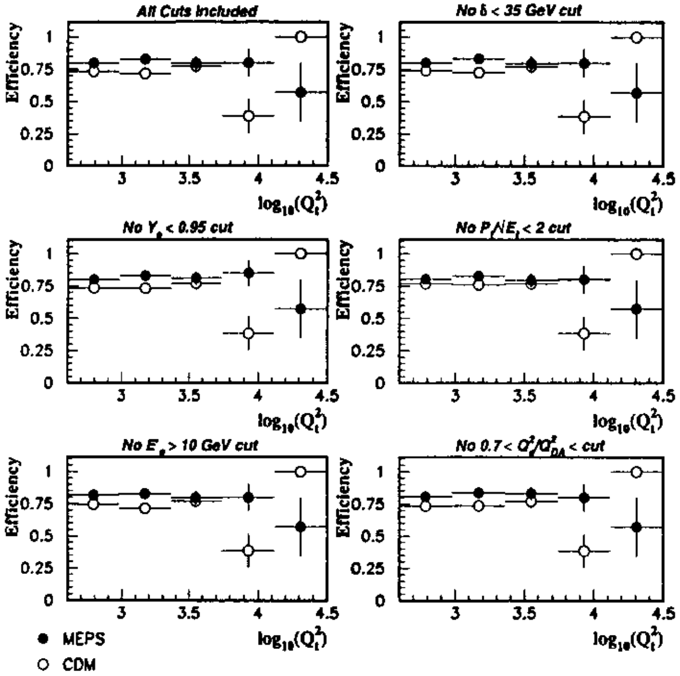

Figure 9.5: *Cut efficiency as a function of* Q_t^2 *for MEPS and CDMBGF hadronization models. Vertical bars are statistical errors. Efficiency is the ratio of the number of events that pass cuts and reconstructed in the bin to the number of events generated in the bin and pass cuts.*

Systematic Error Source	Q^2 bin (GeV^2)				
	400–1000	1000–2500	2500–6250	6250–15625	> 15625
p_{tmiss}	4.0	4.0	4.0	4.0	4.0
$p_{tmiss}^{out}/p_{tmiss}$	0.0	0.0	0.0	0.0	0.0
$p_{tmiss}^{maxcell}/p_{tmiss}$	0.0	0.0	0.0	0.0	0.0
$\|z\|$ and trks on vertex	4.4	4.4	4.4	4.4	4.4
Energy Corrections	9.0	9.0	9.0	9.0	9.0
Cal Energy Scale	5.0	0.0	0.0	0.0	3.0
CDMBGF vs MEPS	2.0	2.0	2.0	2.0	2.0
Trigger Efficiency	3.0	0.0	0.0	0.0	0.0
Trk on vertex	4.0	4.0	4.0	4.0	4.0
Luminosity	2.5	2.5	2.5	2.5	2.5
Total Error	13.3	11.9	11.9	11.9	12.3

Table 9.3: *Percent systematic errors on the CC measured cross sections due to various sources. The errors are given in percent and are added in quadrature to find the total error.*

±5%, ±1%, ±0.8%, ±0.6%, and ±3% in the measured cross sections from the lowest to the highest Q^2 bin, respectively. Therefore, an error of ±5%(3%) is assigned to the lowest(highest) Q^2 bin due to the energy scale. No error is assigned to the other bins for this effect.

Another systematic error is caused by differences between the various distributions of data and Monte Carlo irrespective of an energy scale difference (type III). The measured statistics in each Q^2 bin for CC is small. Therefore, the combined $Q^2 > 400\ GeV^2$ bin is used, utilizing all the 23 CC events. The error assigned for the $Q^2 > 400\ GeV^2$ bin is also taken to be the error for all of the five individual Q^2 bins. The sources of these systematic errors are:

- $p_{tmiss}^{out}/p_{tmiss}$: CC Monte Carlo and data are in good agreement (figure 7.14). Increasing the $p_{tmiss}^{out}/p_{tmiss}$ cut by as much as 20% from 0.7 to 0.84, the bin acceptance decreases from 0.76 to 0.73. The number of CC data events remains 23 events, resulting in a total cross section for $Q^2 > 400$ of $58pb$, comprising a 3.5% change from the measured cross section of $56pb$. Since the resulting difference in the cross section is small from a 20% change increase in the cut, no error is assigned.

- $p_{tmiss}^{maxcell}/p_{tmiss}$: Data and Monte Carlo distributions are in good agreement. Decreasing the cut from 0.75 to 0.525 (20% decrease) rejects one CC data event. The bin acceptance remains the same at 0.76, resulting in a 4.4% increase in the cross section. Because the resulting increase of the cross section is small for a 20% decrease in the cut, no error is assigned.

- p_{tmiss}: The p_{tmiss} cut is changed by ±10% (corresponding to the hadronic P_{tjb} resolution obtained from NC Monte Carlo, shown in figure 9.1). Increasing the cut by 10% to 13.2 GeV decreases the bin acceptance from 0.76 to 0.75. The number of CC data events remains the same at 22 events, resulting in a cross section of $54.3pb$, which is 3.7% lower than the measured cross section of $56pb$. Therefore, an error of 4% is assigned to all the Q^2 bins.

- $|z|$ and number of tracks on vertex: Figure 9.6 shows the z vertex distribution of the 436 NC candidates with $Q^2_{DA} > 400\ GeV^2$ compared to the NC Monte Carlo. The width of the data and Monte Carlo distributions are the same. However, there is a shift of one bin between the two distributions, where the bin width is $4cm$. In addition, the NC data distribution is wider than Monte Carlo. To account for this, another $3cm$ difference is added to the $4cm$ difference between the NC data and Monte Carlo z vertex distributions. Therefore, the cut is increased by $7cm$ to $|z| < 52cm$. This leaves the bin acceptance the same at 0.76, while increasing the CC data sample to 24, where the additional CC data event has a vertex at $z = -50.9cm$, resulting in a 4.4% increase in the cross section. Decreasing the cut by $7cm$ does not change the bin acceptance and the number of CC data events, yielding no change in the cross section.

  Number of tracks on the vertex: reducing the requirement from 2 to one track, a CC event is added to the sample, leaving the acceptance unchanged. As a result, the cross section is increased by 4.4%. Increasing the cut to 3 tracks on the vertex, reduces the number of CC candidates by 2 to 21 CC data events. The acceptance is reduced from 0.76 to 0.72, resulting in a cross section of $54 pb$, which is 4% different from the measured cross section.

Therefore, an error of 4.4% is assigned to all Q^2 bins to these two cuts.

- Uncertainty in hadronic energy corrections of chapter 8: To test the uncertainty due to the data and Monte Carlo correction methods, the data correction is applied to the NC data sample and the Monte Carlo correction is applied to the NC Monte Carlo. The resulting $\sigma_{NC}(Q^2 > 400\ GeV^2)$ is 1069 pb, 9% higher than the measured value of 979 (table 9.1). Therefore, an error of 9% is assigned to σ_{CC} for all the CC bins due to the hadronic correction. When no correction is applied, $\sigma_{CC}(Q^2 > 400\ GeV^2) = 55.5 pb$, which is consistent with the value given in table 9.1. However, in this case, 21 events survive the $Q^2 > 400\ GeV^2$ cut, where Q^2 here is Q^2_{jb}, reconstructed using the JB reconstruction method. Since the acceptance is also reduced by 9% from 0.76 to 0.7, there is no change in the cross section . Therefore, no error is assigned to the JB reconstruction of Q^2.

- Sensitivity to structure functions: CC Monte Carlo data are generated with the MRSD0 set of structure functions. To quantify the dependence of the measured cross sections on various structure functions, MRSD$'_-$, CTEQ, and GRV sets are considered. The CC Monte Carlo events are reweighted with these sets and the obtained cross sections differ by less than 1% from the values given in table 9.1. Therefore, no error is assigned due to different structure functions.

- Sensitivity to final state models and fragmentation: The default CC Monte Carlo events used in this analysis are generated by the LEPTO 6.1 generator with the MEPS model of fragmentation. If the CDMBGF model is used instead, the CC bin acceptances increase by up to 5%.[44] Therefore, an error of 5% is assigned fot the final state fragmentation model.

- Trigger efficiency: To find the effect of the trigger efficiency on $\mathcal{A}_{CC}$, the trigger threshold curves for four relevant trigger quantities are obtained (figure 9.7). These quantities are E_{BEMC}, E_{tot}, E_t, and E_{EMC}. The efficiency for the E_{BEMC} quantity is obtained by dividing the E_{BEMC} profile for the data triggered by the E_{BEMC} trigger by the E_{BEMC} profile for data events triggered by the other trigger quantities, irrespective of whether the E_{BEMC} triggered these events. The threshold curves for the rest of the trigger quantities shown in figure 9.7 are found in the same manner. Figure 9.8 shows the trigger quantity profiles for CC Monte Carlo events. Overlayed in this figure are also the efficiency corrected profiles, which are obtained by multiplying the trigger profiles for the CC Monte Carlo events by the threshold curves.

  The efficiency , ϵ_i, of each CC Monte Carlo event that passes the CC selection is found for each of trigger quantity i, where $i = E_{BEMC}$, E_{tot}, E_t, or E_{EMC}. The inefficiency for each CC Monte Carlo event due to the trigger quantity i is $1 - \epsilon_i$. The total inefficiency of each Monte Carlo event is $\prod_{i=1}^{4}(1 - \epsilon_i)$. Performing the sum $\sum[1 - (\prod_{i=1}^{4} 1 - \epsilon_i)]$, where the summation is over all the CC Monte Carlo events passing the cuts

$Q^2 > Q^2_{min}$ (GeV^2)	NC uncorr systematic	NC corr systematic	CC uncorr systematic	CC corr systematic	R
$Q^2 > 400$	7	4	11.3	6.4	$17.6^{+7.6}_{-2.1}$
$Q^2 > 1000$	7	4	11	4	$5.0^{+2.8}_{-0.3}$
$Q^2 > 2500$	4.2	4	11	4	$1.6^{+1.1}_{-0.2}$
$Q^2 > 6250$	4.2	3	11	4	$0.4^{+0.4}_{-0.1}$
$Q^2 > 15625$	4.2	2	11	5	$0.5^{+1.3}_{-0.5}$

Table 9.4: *Correlated systematic errors, uncorrelated systematics errors, and total combined error on R (statistical and systematic), given in percent. Correlated systematic errors are errors affected by the calorimeter energy scale. They correlate the NC and CC measurements. The uncorrelated systematics are the rest of the systematic errors that are not affected by the energy scale (see text for more details).*

that have Q^2 reconstructed in the bin, and dividing the result by the total number of CC events generated in the bin gives the total trigger efficiency corrected acceptance for the bin.

The effect of the trigger efficiency is a 3.0% reduction in the lowest Q^2 bin acceptance. It is less than a percent for the rest of the bins. Therfore, a 3% error is assigned for the lowest Q^2 bin and no error for the rest of the bins.

9.2.3 $R(\sigma_{NC}/\sigma_{CC})$ Errors

In this section, the errors on $R(\sigma_{NC}/\sigma_{CC})$ are evaluated. These errors are obtained by smearing the observed number of data events and the reconstructed number of events by gaussian or gamma distributions, as described

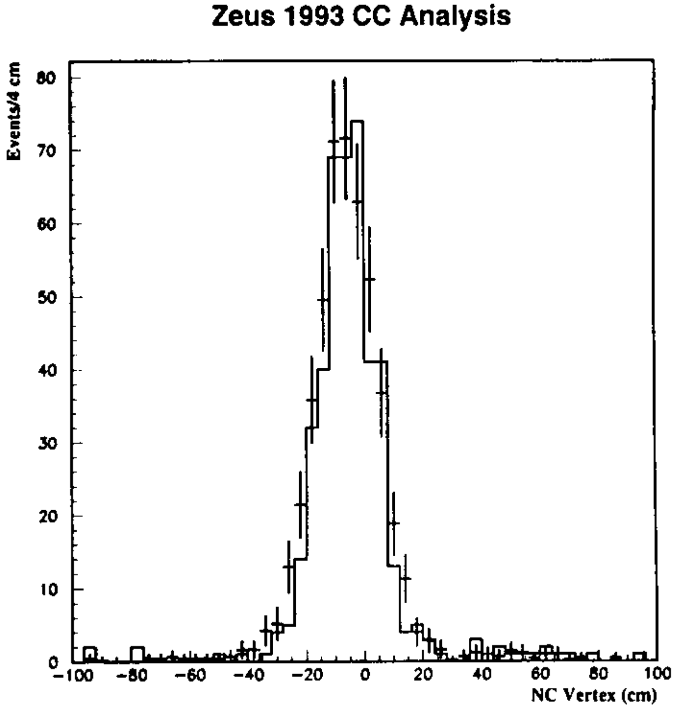

Figure 9.6: *z vertex distribution for NC data (histogram with error bars) and Monte Carlo events (solid histogram).*

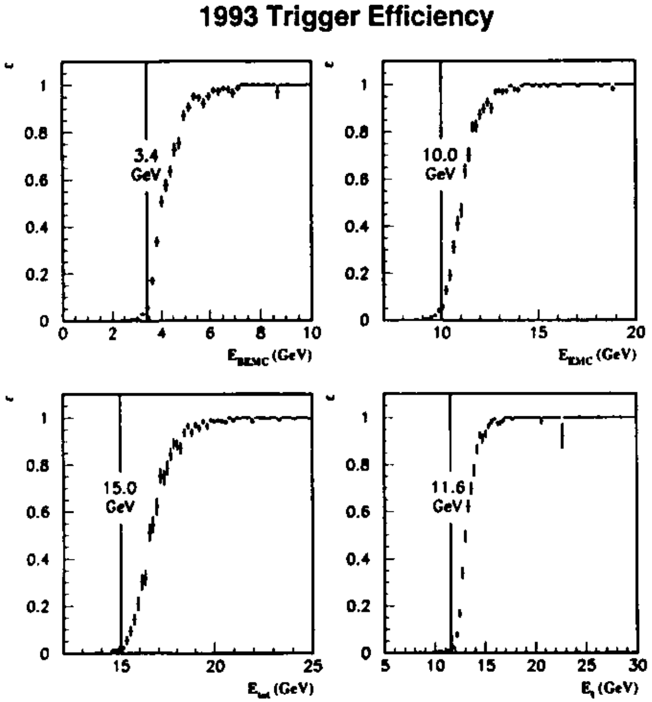

Figure 9.7: *Trigger quantity efficiency* ϵ *vs trigger quantity energy. The lines indicate the energy thresholds: (A)* E_{BEMC} *(B)* E_{EMC} *(C)* E_{tot} *(D)* E_t.

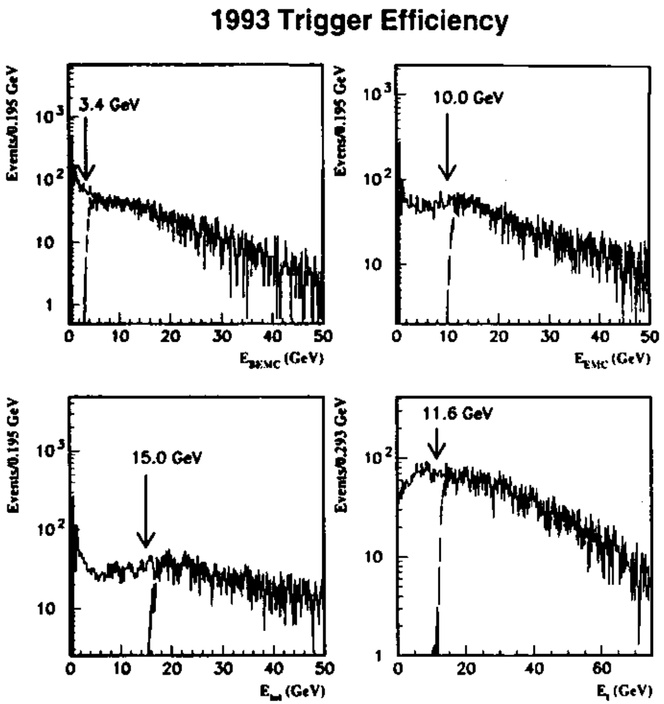

Figure 9.8: *Efficiency corrected energy spectrum of the trigger quantities. The solid histogram shows the trigger quantities profiles for Monte Carlo events and the histogram with error bars shows the efficiency corrected trigger acceptance. The lines indicate the energy thresholds.*

below. These distributions are used to obtain the total combined errors (statistical and systematic) on R. The values of R are listed with the total errors in table 9.4.

9.2.4 Errors Evaluation

R is given by

$$R = \frac{\sigma_{NC}}{\sigma_{CC}} = \frac{N^{obs}_{NC}/A_{NC}}{N^{obs}_{CC}/A_{CC}} \qquad (9.1)$$

where $A_{NC} = N^{rec}_{NC}/N^{gen}_{NC}$ and $A_{CC} = N^{rec}_{CC}/N^{gen}_{CC}$. $N^{gen}_{NC,CC}$ and $N^{rec}_{NC,CC}$ are the number of generated and reconstructed NC and CC Monte Carlo events, respectively. N^{obs}_{NC} and N^{obs}_{CC} are the number of observed NC and CC data events, respectively. R is evaluated using the values given in table 9.1 for $N^{obs}_{NC,CC}$ and $A_{NC,CC}$. The Errors on $N^{obs,rec}_{NC,CC}$ are used to calculate the uncertainty on R. $N^{obs,rec}_{NC,CC}$ is smeared according to its errors, as described below, taking into account correlated errors on N^{rec}_{NC} and N^{rec}_{CC}. The uncertainty on R is obtained in the following way:

- For Monte Carlo events, $N^{rec}_{NC,CC}$ is smeared by a gaussian distribution, resulting in the distribution $P^{rec}_{NC,CC,stat}$, with mean $N^{rec}_{NC,CC}$ and width $2\sqrt{N^{rec}_{NC,CC}}$, where $\sqrt{N^{rec}_{NC,CC}}$ is the statistical error on $N^{rec}_{NC,CC}$. The distribution is generated by the following algorithm:

  1. A random number, g_r, is generated from a gaussian distribution of mean zero.
  2. g_r is shifted to a value, g'_r, distributed around the mean $N^{rec}_{NC,CC}$, with a width of $2\sqrt{N^{rec}_{NC,CC}}$ using the following formula

  $$g'_r = g_r \times \sqrt{N^{rec}_{NC,CC}} + N^{rec}_{NC,CC} \qquad (9.2)$$

  The above two steps are repeated 50000 times (i.e. 50000 random numbers generated) for every Q^2 bin. The distribution of the 50000 values of g'_r is denoted by $P^{rec}_{NC,CC,stat}$.

- For data events, if $N^{obs}_{NC,CC} \geq 9$, it smeared by a gaussian distribution. If $N^{obs}_{NC,CC} < 9$, then it is smeared by a gamma distribution, assuming $N^{obs}_{NC,CC}$ is a continuous number. Whether a gaussian or a gamma distribution is used for smearing $N^{obs}_{NC,CC}$, the resulting distribution of smeared values is denoted by $P^{obs}_{NC,CC}$. The width of $P^{obs}_{NC,CC}$ is $2\sqrt{N^{obs}_{NC,CC}}$ if a gaussian distribution is used for smearing.

- The width of $P^{rec}_{NC,CC,stat}$ obtained thus far includes only the statistical error on $N^{rec}_{NC,CC}$. To incorporate the systematic errors on $N^{rec}_{NC,CC}$, two more distributions are obtained with the following systematic errors:

  1. NC–CC correlated systematics: These are systematic errors on the bin acceptance that depend on the calorimeter energy scale and are correlated for both NC and CC. For NC, these errors include the effects of e^- and hadronic energy scales on acceptance and on the cuts $E - P_z$, y_e, and E'_e. For CC, they affect $p_{t_{miss}}$ and the hadronic energy scale. These errors are listed in tables 9.2 and 9.3. The total error due to these effects, shown in table 9.1, is obtained for each bin by adding the individual errors in quadrature. The total error for each bin is then used as the width of the gaussian distribution needed to smear $N^{rec}_{NC,CC}$ for that bin. The identical random numbers generated from a gaussian distribution to smear N^{rec}_{NC} are also used to smear N^{rec}_{CC}. This is done in order to reflect

the fact that these errors are correlated. The resulting distributions are $P^{rec}_{NC,CC,1}$, which are obtained by

$$P^{rec}_{NC,CC,1} = g_r \times p_{corr} \times N^{rec}_{NC,CC} + N^{rec}_{NC,CC} \tag{9.3}$$

where p_{corr} is the percent total correlated systematic error, given in table 9.4, on $N^{rec}_{NC,CC}$. 50000 random numbers are generated to obtain $P^{rec}_{NC,CC,1}$.

2. Uncorrelated systematics: The remaining systematic errors (tables 9.2 and 9.3) are uncorrelated between NC and CC. The individual errors are added in quadrature to find the total error, given in table 9.4. The resulting total errors for each bin are taken as the widths of the gaussian distributions. Since these are uncorrelated, two different sets of random numbers are generated to smear N^{rec}_{NC} and N^{rec}_{CC}, giving $P^{rec}_{NC,CC,2}$, which is obtained by

   $$P^{rec}_{NC,CC,2} = g_r \times p_{uncor} \times N^{rec}_{NC,CC} + N^{rec}_{NC,CC} \tag{9.4}$$

   where p_{uncorr} is the percent uncorrelated systematic error, shown in table 9.4, on $N^{rec}_{NC,CC}$. 50000 random numbers are generated to obtain $P^{rec}_{NC,CC,2}$.

The final distribution, $P^{rec}_{NC,CC}$, that includes the statistical, and uncorrelated and correlated systematic errors on $N^{rec}_{NC,CC}$ is obtained by adding the above three distributions of shifted random numbers,

$$P^{rec}_{NC,CC} = P^{rec}_{NC,CC,stat} + P^{rec}_{NC,CC,1} + P^{rec}_{NC,CC,2} \tag{9.5}$$

- Performing the replacement $N^{obs,rec}_{NC,CC} \rightarrow P^{obs,rec}_{NC,CC}$ in equation (9.1), we obtain

  $$P(r) = \frac{P^{obs}_{NC}\left(\frac{P^{rec}_{NC}}{N^{gen}_{NC}}\right)}{P^{obs}_{CC}\left(\frac{P^{rec}_{CC}}{N^{gen}_{CC}}\right)} \tag{9.6}$$

  Since this equation performs a division of distributions, R in equation (9.1) is replaced by a distribution $P(r)$. Note that $N^{gen}_{NC,CC}$ is not replaced by a distribution since the generated Monte Carlo events are not smeared.

- The errors on R are found by calculating the areas under the distribution $P(r)$ that contain 15.9% and 84.1% of the total integrated area (this represents the 68.3% confidence interval). r_{max} and r_{min} are values of R that result in $\int_0^{r_{min}} P(r)dr = 0.159$ and $\int_{r_{max}}^{\infty} P(r)dr = 0.841$ so that $\int_{r_{min}}^{r_{max}} P(r)dr = 0.68$. R is then given as $R^{+\delta_1}_{-\delta_2}$, with $\delta_1 = r_{max} - R$ and $\delta_2 = R - r_{min}$.

The "smeared" ratio distribution of the acceptances, $P_{ratio}(\mathcal{A}_{NC}/\mathcal{A}_{CC})$, is shown in figures 9.9 and 9.10, for each Q^2 bin. It is given by

$$P_{ratio}\left(\frac{\mathcal{A}_{NC}}{\mathcal{A}_{CC}}\right) = \frac{P^{rec}_{NC}}{N^{gen}_{NC}} \times \frac{N^{gen}_{CC}}{P^{rec}_{CC}} \tag{9.7}$$

$P(r)$ distributions are shown in figures 9.11 and 9.12.

9.2.5 Radiative Corrections

Radiative corrections are calculated using HERACLES 4.1.[36] For NC events, it includes an $\mathcal{O}(\alpha_s)$ correction due to F_L, and an $\mathcal{O}(\alpha)$ correction resulting from one loop virtual corrections and real bremsstrahlung (initial and final state radiation). The final state radiated photon energy is added back to the

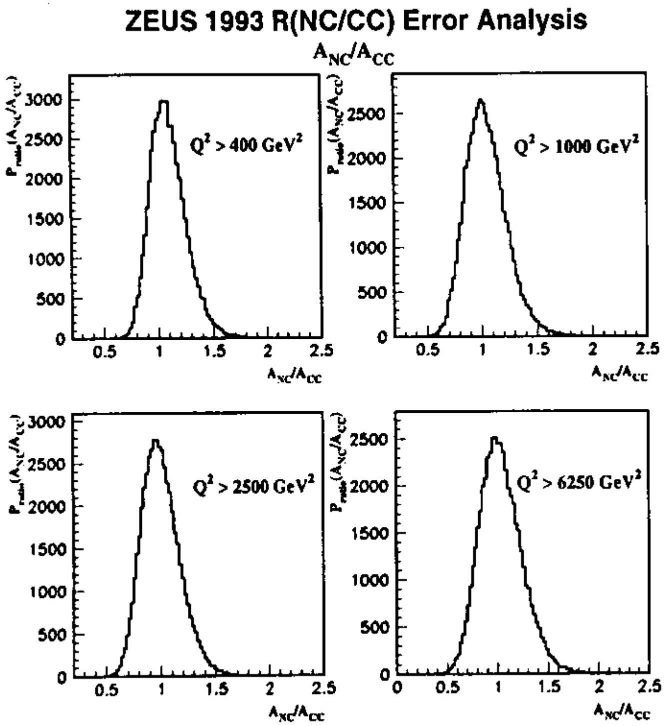

Figure 9.9: *Smeared acceptance ratio distributions, $P_{ratio}(A_{NC}/A_{CC})$, for $Q^2 > 400\ GeV^2$, $> 1000\ GeV^2$, $> 2500\ GeV^2$, and $> 6250\ GeV^2$, respectively (continued in figure 9.10).*

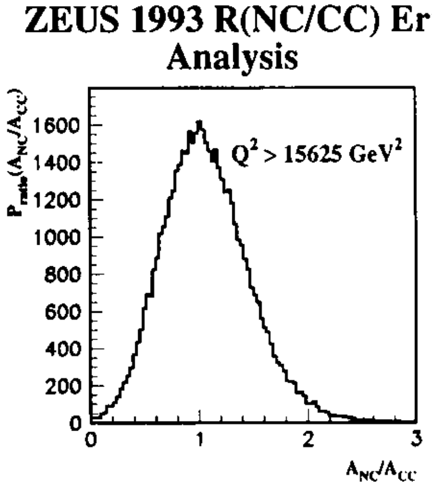

Figure 9.10: *Smeared acceptance distributions, $P_{ratio}(A_{NC}/A_{CC})$, for $Q^2 > 15625\ GeV^2$.*

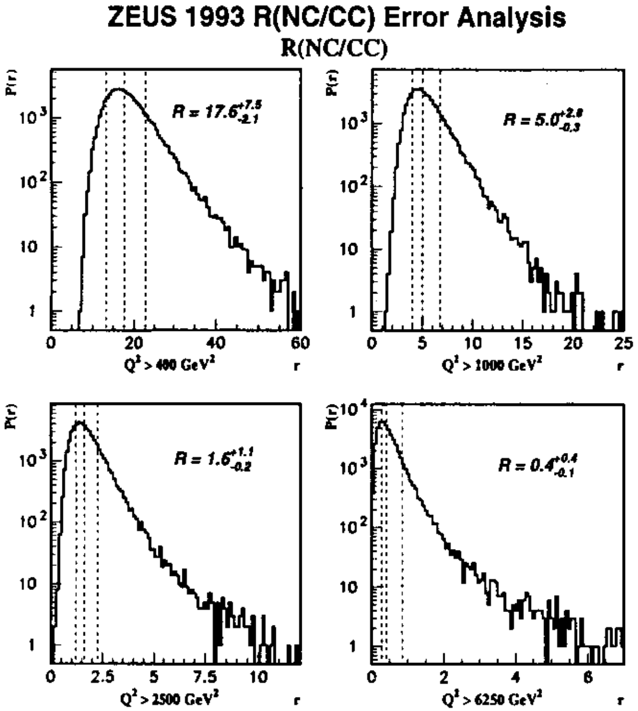

Figure 9.11: *$P(r)$ vs r for $Q^2 > 400$ GeV^2, > 1000 GeV^2, > 2500 GeV^2, and > 6250 GeV^2, respectively (continued in figure 9.12).*

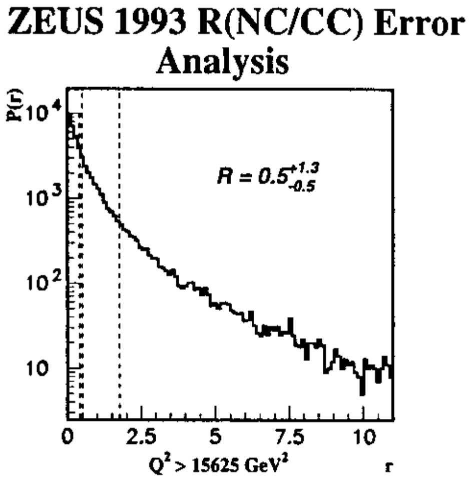

Figure 9.12: *$P(r)$ vs r for $Q^2 > 15625$ GeV^2.*

scattered electron energy before Q^2 is calculated. A cut of $y < 0.95$ is included in these calculations. For CC events, the radiative corrections include only the initial state radiation.

The radiative correction factors are 0.89, 0.88, 0.89, 0.91, and 0.95 for NC bins (lowest to highest) and 1.02, 1.03, 1.03, 1.03, and 1.02 for CC bins (lowest to highest). For 87500 $GeV^2 > Q^2 > Q^2_{min}$ bins, where Q^2_{min} = 400 GeV^2, 1000 GeV^2, 2500 GeV^2, 6250 GeV^2, and 15625 GeV^2, the correction factors are the same as listed above for the differentially binned NC and CC events. Therefore, the measured cross sections and the errors are scaled by these same factors. The correction factor for the errors on R is the ratio of the NC correction factor to the CC factor.

9.3 Final Cross Sections and R

The final cross sections are in table 9.5 and are shown in figure 9.13. The ratio of the cross sections approaches unity at $Q^2 > 2500$ GeV^2 demonstrating the equal strength of the weak and electromagnetic forces at high Q^2. The NC cross section falls rapidly with Q^2 due to the massless photon propagator. On the other hand, the CC cross section starts out flat at lower Q^2 and falls rapidly at higher Q^2 due to the finite mass W-propagator.

Q^2_{min}, Q^2_{max} (GeV^2)	400,1000	1000,2500	2500,6250	6250,15625	15625,87500
N_{NC}	328	86	18	3	1
r_{NC}	0.89	0.88	0.89	0.91	0.95
σ_{NC}	651	171	39	6.6	2.5
δ_{NC}	$\pm 36 \pm 56$	$\pm 19 \pm 21$	$\pm 9 \pm 4.3$	${}^{+4.2}_{-3.6} \pm 0.7$	${}^{+3.2}_{-2.1} \pm 0.3$
σ^{SM}_{NC}	862	218	51	9.9	1.1
σ^{γ}_{NC}	836	200	43	6.5	0.57
N_{CC}	2	7	5	7	2
r_{CC}	1.02	1.03	1.03	1.03	1.02
σ_{CC}	5.6	16.3	12.4	17.6	5.4
δ_{CC}	${}^{+4.7}_{-3.6} \pm 0.7$	${}^{+6.5}_{-6.0} \pm 2.0$	${}^{+5.9}_{-5.4} \pm 1.4$	${}^{+6.9}_{-6.5} \pm 2.1$	${}^{+4.6}_{-1.9} \pm 0.7$
σ^{SM}_{CC}	13.1	16.7	15.5	7.8	1.6
	87500 $GeV^2 > Q^2 > Q^2_{min}$				
r_{NC}	0.89	0.88	0.89	0.91	0.95
σ_{NC}	871	217	48	8.8	2.5
δ_{NC}	$\pm 42 \pm 75$	$\pm 21 \pm 27$	$\pm 10 \pm 5.3$	${}^{+4.9}_{-4.2} \pm 1.0$	${}^{+3.2}_{-2.1} \pm 0.3$
r_{CC}	1.02	1.03	1.03	1.03	1.02
σ_{CC}	57	50	35	23.2	5.4
δ_{CC}	$\pm 12 \pm 7.5$	$\pm 11 \pm 6.0$	$\pm 9.4 \pm 4.1$	$\pm 7.7 \pm 2.8$	${}^{+4.6}_{-1.9} \pm 0.7$
r_{NC}/r_{CC}	0.87	0.85	0.86	0.88	0.93
$R = \frac{\sigma_{NC}}{\sigma_{CC}}$	$15.3^{+6.5}_{-1.8}$	$4.3^{+2.4}_{-0.3}$	$1.4^{+1.4}_{-0.2}$	$0.4^{+0.4}_{-0.1}$	$0.5^{+1.2}_{-0.5}$

Table 9.5: *The number of observed events, radiative correction factors, r_{NC} and r_{CC}, measured cross sections($\pm$statistical$\pm$systematic $= \delta_{NC,CC}$) of NC and CC, Standard Model (SM) Born cross sections, and $R(\sigma_{NC}/\sigma_{CC})$, including the total error on R.*

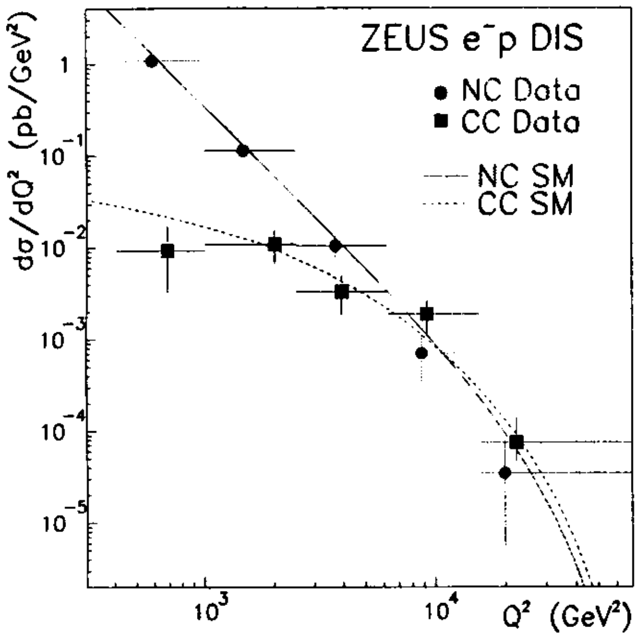

Figure 9.13: *NC and CC differential cross sections, $d\sigma/dQ^2$. Points with the error bars are the measured cross sections. The horizontal bars indicate the bin sizes. The solid curves are the Standard Model (SM) predictions. The points are plotted at the average Q^2 of Monte Carlo events reconstructed in the bin.*

Chapter 10

CONCLUSIONS AND OUTLOOK

The ZEUS detector was used to measure NC and CC cross sections at $Q^2 > 400\ GeV^2$. At high Q^2, the exchanged boson has a small wavelength, enabling it to resolve the structure of the proton. In addition, the high Q^2 regime opens a window for detection of deviations from the Standard Model. In 1993, HERA collided 26.7 GeV electrons with 820 GeV protons with ZEUS collecting $0.54 pb^{-1}$ of data.

The NC selection started with about 351000 data events, out of which 436 NC candidates were identified with $Q^2 > 400\ GeV^2$ after all selection cuts were applied. The cuts rejected background events (photoproduction and cosmics) with high efficiency. The overall cut efficiency for selecting NC events with $Q_t^2 > 400\ GeV^2$ was 0.82 .

The CC selection identified 24 CC data candidates from a total of 33000 events passed by the Third Level Trigger. The selection cuts rejected beam-gas and cosmic backgroud with high efficiency. The overall cut efficiency for selecting CC events with $Q_t^2 > 400\ GeV^2$ was 0.76 .

The NC data were reconstructed using the DA reconstruction method. The CC were reconstructed with the JB reconstruction method. The JB reconstruction is biased toward low energies due to loss of particles from the hadronic jet in the inactive material in front of the calorimeter. Therefore, two correction methods using the NC data and Monte Carlo were obtained to reduce the bias. The correction obtained from the NC data was used to correct the CC data, while the correction obtained from the NC Monte Carlo was used to correct the CC Monte Carlo.

The NC and CC cross sections and their ratios were measured in five Q^2 bins, ranging in Q^2 from 400 GeV^2 to 87500 GeV^2. These measurements show for the first time that the NC and CC cross sections are comparable at high Q^2. The NC cross sections falls rapidly with Q^2 due to the photon propagator. For the first time, the W propagator effect on the CC cross section is seen, where the CC cross section starts out flat at lower Q^2 and then falls rapidly at higher Q^2. Both NC and CC measurements are in agreement with the Standard Model predictions.

In 1994, HERA collided positrons on protons. For the NC current interactions, the third component of isospin, I_3, is $+1/2$ for e^+, the effect of which is to reduce in the NC cross section. For CC interactions, since the proton has more u quarks than d quarks, it is expected that the positron cross section is also smaller than for electron collisions. Comparing the electron and positron cross sections enables us to test the Standard Model. In addition, measuring positron cross sections with high statistics and comparing them with high statistics electron measurements will determine F_3 for both NC and CC interactions at high Q^2 values not accessable to previous fixed target experiments, enabling observation of the valence quarks and, thereby, measurement of their structure functions at these Q^2 values.

Appendix A

Error Estimates on the JB and DA Variables

Errors on measuring the DA variables are related to $\delta\gamma_H$ and $\delta\theta_e$, errors in measuring γ_H and θ_e (angles of the hadronic system and the scattered electron, respectively). Errors on the JB variables are dependent on $\delta\theta_i$ and $\delta\phi_i$, the errors on the angular positions, θi and ϕ_i, of the calorimeter cell i, and δE_i, error on energy measurement, E_i, in the cell.

P_{tDA} is given by

$$P_{tDA}^2 = Q_{DA}^2(1 - y_{DA}) \tag{A.1}$$

Using the following 2 expressions

$$Q_{DA}^2 = 4E_e^2 \frac{\sin\gamma_H(1+\cos\theta_e)}{A} \tag{A.2}$$

and

$$y_{DA} = \frac{\sin\theta_e(1-\cos\gamma_H)}{A}, \tag{A.3}$$

where

$$A = \sin\gamma_H + \sin\theta_e - \sin(\theta_e + \gamma_H) \tag{A.4}$$

and E_e is the incoming electron energy of 26.7 GeV, one can obtain

$$P_{tDA} = \frac{2E_e}{A}\sin\gamma_H\sin\theta_e \tag{A.5}$$

Assuming Gaussian errors in γ_H and θ_e, then the error on P_{tDA} is

$$\delta P_{tDA} = \left[\left(\frac{\partial P_{tDA}}{\partial \gamma_H}\delta\gamma_H\right)^2 + \left(\frac{\partial P_{tDA}}{\partial \theta_e}\delta\theta_e\right)^2\right]^{1/2} \tag{A.6}$$

From equations (A.4) and (A.5) one obtains

$$\frac{\partial P_{tDA}}{\partial \gamma_H} = \frac{2E_e}{A}\sin\theta_e\left(\cos\gamma_H - \frac{1}{A}\sin\gamma_H\frac{\partial A}{\partial \gamma_H}\right) \tag{A.7}$$

with

$$\frac{\partial A}{\partial \gamma_H} = \cos\gamma_H - \cos(\theta_e + \gamma_H) \tag{A.8}$$

Since both P_{tDA} and A are symmetric in θ_e and γ_H, the corresponding equations for $\partial P_{tDA}/\partial\theta_e$ and $\partial A/\partial\theta_e$ have the same form as given in equations (A.7) and (A.8) but with γ_H exchanged with θ_e.

Similarly, the error on y_{DA}, δy_{DA}, is

$$\delta y_{DA} = \left[\left(\frac{\partial y_{DA}}{\partial \gamma_H}\delta\gamma_H\right)^2 + \left(\frac{\partial y_{DA}}{\partial \theta_e}\delta\theta_e\right)^2\right]^{1/2} \tag{A.9}$$

Using A.3, one finds

$$\frac{\partial y_{DA}}{\partial \theta_e} = \frac{1-\cos\gamma_H}{A}\left(\cos\theta_e - \frac{1}{A}\sin\theta_e\frac{\partial A}{\partial \theta_e}\right) \tag{A.10}$$

and

$$\frac{\partial y_{DA}}{\partial \gamma_H} = \frac{\sin\theta_e}{A}\left[\sin\gamma_H - \frac{1}{A}(1-\cos\gamma_H)\frac{\partial A}{\partial \gamma_H}\right] \tag{A.11}$$

Using the Monte Carlo, the errors $\delta\theta_e$ and $\delta\gamma_H$ are estimated to be 0.0194 and 0.127 radians, respectively.

The errors on the JB variables are obtained from

$$\vec{P_{tjb}} = \Sigma_i \sin\theta_i \hat{\varepsilon}_i \tag{A.12}$$

and

$$\delta|\vec{P_{tjb}}| = \left\{\sum_i\left[\left(\frac{\partial|\vec{P_{tjb}}|}{\partial\theta_i}\delta\theta_i\right)^2 + \left(\frac{\partial|\vec{P_{tjb}}|}{\partial\phi_i}\delta\phi_i\right)^2 + \left(\frac{\partial|\vec{P_{tjb}}|}{\partial E_i}\delta E_i\right)^2\right]\right\}^{1/2} \tag{A.13}$$

where the sum is over calorimeter cells, $\hat{\varepsilon}_i = (\cos\phi_i, \sin\phi_i)$, and $\delta|\vec{P_{tjb}}|$ is the error on P_{tjb}. After evaluating the derivatives in equation (A.13), one obtains

$$\begin{aligned}(\delta|\vec{P_{tjb}}|)^2 &= \sum_i\left(E_i\hat{P_{tjb}}\cdot\hat{\varepsilon}_i\cos\theta_i\delta\theta_i\right)^2\\ &+ \sum_i\left(E_i\hat{P_{tjb}}\cdot\hat{\zeta}_i\sin\theta_i\delta\phi_i\right)^2\\ &+ \sum_i\left(\hat{P_{tjb}}\cdot\hat{\varepsilon}_i\sin\theta_i\delta E_i\right)^2\end{aligned} \tag{A.14}$$

where $\hat{\zeta}_i = (-\sin\phi_i, \sin\phi_i)$ and $\hat{P_{tjb}} = (P_x, P_y)/P_{tjb}$. The following are taken as first order estimates of ΔE_I:

$$\begin{aligned}\delta E_i &= 0.35\sqrt{E_i} \quad \text{for HAC cells}\\ \delta E_i &= 0.18\sqrt{E_i} \quad \text{for EMC cells}\end{aligned} \tag{A.15}$$

Errors on the angles vary depending on the cell position in the calorimeter. In F/RCAL, the errors on the angles are

$$\delta\theta_i = \left(\frac{\cos\theta_i}{R_i}\right)\left[(\cos\phi_i\delta x_i)^2 + (\sin\phi_i\delta y_i)^2\right]^{1/2} \tag{A.16}$$

and

$$\delta\phi_i = \left(\frac{1}{x_i^2 + y_i^2}\right)\left[(\sin\phi_i\delta x_i)^2 + (\cos\phi_i\delta y_i)^2\right]^{1/2} \tag{A.17}$$

with $R_i = (x_i^2 + y_i^2 + z_i^2)^{1/2}$ is the distance from the interaction point to the cell i. δx_i and δy_i are estimated to be

$$\begin{aligned}\delta x_i &= \frac{x - dimension\ of\ cell\ i}{\sqrt{12}}\\ \delta y_i &= \frac{y - dimension\ of\ cell\ i}{\sqrt{12}}\end{aligned} \tag{A.18}$$

The transverse dimensions are 20 x 5 cm^2 for FCAL EMC cells, 20 x 10 cm^2 for RCAL EMC cells, and 20 x 20 cm^2 for F/RCAL HAC cells.

In BCAL, the angular errors are

$$\delta\theta_i = \frac{\sin\theta_i}{R_i}\delta z_i \tag{A.19}$$

and

$$\delta\phi_i = \frac{2\pi/32}{\sqrt{12}} \tag{A.20}$$

where δz_i is taken to be the z-dimension of the cell, 5 cm for an EMC cell and 20 cm for a HAC cell.

The errors on y_{jb} are derived from

$$y_{jb} = \frac{1}{2E_e}\sum_i E_i(1-\cos\theta_i) \tag{A.21}$$

Since

$$\delta y_{jb} = \frac{1}{2E_e}\left\{\sum_i \left[\left(\frac{\partial y_{jb}}{\partial E_i}\delta E_i\right)^2 + \left(\frac{\partial y_{jb}}{\partial \theta_i}\delta\theta_i\right)^2\right]\right\}^{1/2} \tag{A.22}$$

then using equation (A.21) in (A.22), δy_{jb} becomes

$$\delta y_{jb} = \frac{1}{2E_e}\left\{\sum_i \left[\left((1-\cos\theta_i)\delta E_i\right]^2 + (E_i\sin\theta_i\delta\theta_i)^2\right]\right\}^{1/2} \tag{A.23}$$

The errors on angles are estimated as given above.

Once all the above errors are determined, then δr (see equation (8.5)) for each data point is calculated from $\delta r = \sqrt{(\delta P_{tDA}\partial r/\partial P_{tDA})^2 + (\delta P_{tjb}\partial r/\partial P_{tjb})^2}$, yielding

$$\delta r = \frac{1}{P_{tjb}^2}\left[(P_{tjb}\delta P_{tDA})^2 + (P_{tDA}\delta P_{tjb})^2\right]^{1/2} \tag{A.24}$$

for the P_{tjb} correction and

$$\delta r = \frac{1}{y_{jb}^2}\left[(y_{jb}\delta y_{DA})^2 + (y_{DA}\delta y_{jb})^2\right]^{1/2} \tag{A.25}$$

for the y_{jb} correction.

References

1. H1 Collab., I. Abt et al., *Phys. Lett.* **B324**, 241(1994).
2. ZEUS Collaboration, M. Derrick et al., *Phys. Rev. Lett.*, **Vol 75**, 1006 (1995).
3. I. J. R. Aitchison and A. J. G. Hey, *Gauge Theories in Particle Physics*, 1989, IOP Publishing Ltd.
4. C. N. Yang and R. L. Mills, *Phys. Rev.*, **96**, 191 (1954).
5. F. Halzen and A. Martin, *Quarks and Leptons*, 1984, John Wiley and Sons.
6. V. Barger and R. Phillips, *Collider Physics*, 1988, Addison–Wesley.
7. R. P. Feynman, *Photon–Hadron Interactions*, 1972, Benjamin.
8. J. Blümlein, DESY 93-124, 1993.
9. Donald H. Perkins, *Introduction to High Energy Physics*, 1987, Addison–Wesley.
10. The Particle Data Group, L. Montanet et al., *Phys. Rev.* D (1994) 1309.
11. R. Brinkmann, DESY HERA 88-03, 1988.
12. ZEUS Collaboration, *The ZEUS Detector*, Status Report 1993, ed. by Uwe Holm, 1993.
13. C. Fabjan, *Techniques and Concepts of High Energy Physics-III*, ed. by T. Ferbel, Plenum Publishing, 1985.

14. U. Amaldi, *Physica Scripta*, **Vol. 23**, 409 (1981).

15. J. Krüger, *The Uranium Scintillator Calorimeter for the ZEUS Detector at the Electron-Proton Collider HERA*, Internal Report, DESY F35-92-02, 1992.

16. A. Bernstein et al., DESY 93-076 (1993).

17. V. A. Jamieson, *Measurement of Scaled Momentum Distributions in the Breit Frame at HERA Using the ZEUS Detector*, Internal Report, DESY F35-95-01, 1995.

18. K. Piotrzkowski and M. Zachara, ZEUS-Note 94-167, 1995.

19. B. Bylsma et al., *Nucl. Instr. and Meth.*, **A305**, 354 (1991).

20. H. Uijterwaal, *The Global Second Level for ZEUS*, Ph.D. Thesis, Universiteit van Amsterdam, 1992.

21. U.Behrens et al., ZEUS-Note 91-071, 1991.

22. S. M. Fisher, *The ADAMO Data System*, Programmers manual, version 3.1, RAL-preprint, 1991.

23. F. S. Chlebana, *First Measurement of the Proton Structure Function F_2 with the ZEUS Detector*, Internal Report, DESY F35D-94-02, 1994.

24. A. Caldwell et al., *Nucl. Instr. and Meth.*, **A321**, 356 (1992).

25. L. Hervás, *The Pipelined Readout for the ZEUS Calorimeter*, Internal Report, DESY F35D-91-01, 1991.

26. Herman van der Lugt, *The Data Acquisition and Second Level Trigger System for the ZEUS Calorimeter*, Ph.D. Thesis, Universiteit van Amsterdam, 1993.

27. W. H. Smith et al., *Nucl. Instr. and Meth.*, **A355**, 278 (1995).

28. W. H. Smith et al., ZEUS-Note 89-085, 1989.

29. D. Krakauer, Private communication.

30. S. Bentvelsen, J. Engelen, and P. Kooijman, *Proccedings of the Workshop on Physics at HERA*, **Vol. 1**, DESY, ed. W. Buchmüller and G. Ingelman, 23 (1991).

31. F. Jacquet and A. Blondel, *Proceedings of the Study for an ep Facility in Europe* 79/48, ed. U. Amaldi, 391(1979).

32. ZEUS Collaboration, M. Derrick et al., *Z. Phys.*, **C65**, 379 (1995).

33. GEANT 3.13: R. Brun et al., CERN DD/EE84-1 (1987) - check this one.

34. LEPTO 6.1: G. Ingelman, *Proceedings of the Workshop on Physics at HERA*, **VOL 3**, DESY, ed. W. Buchmüller and G. Ingelman, 1366 (1991).

35. HERACLES 4.1: A. Kwiatkowski, H. Spiesberger, H.-J. Möhring, *Proceedings of the Workshop on Physics at HERA*, **VOL 3**, DESY, ed. W. Buchmüller and G. Ingelman, 1294 (1991).

36. K. Charchula, G. Shuler, H. Spiesberger, CERN-TH.7133/94.

37. A. D. Martin, R. G. Roberts and W. J. Sterling, *Phys. Lett.*, **B306**, 145 (1993).

38. L. Lönnblad, *Comp. Phys. Comm.*, **71**, 15 (1991).

39. E. Gallo, S. Nickel, J. Sedgbeer, ZEUS-Note 94-026 (1994).

40. H. Abramowics et al., ZEUS-Note 93-079, 1993.

41. H. Abramowicz, A. Caldwell, and R. Sinkus, DESY 95-054 (1995).

42. H. U. Bengtsson and T. Sjöstrand, *Comp. Phys. Comm.*, **46**, 43 (1987).

43. ZEUS Collab., PHANTOM - Physics Analysis Techniques, Operations, and Methods - Collection of Subroutines for Data Analysis.

44. S. Nickel, ***Messung von Reaktionen des geladenen Stromes*** $ep \rightarrow \nu X$ ***mit dem ZEUS-Detektor***, Internal Report, DESY F35D-94-10, 1994.

45. A. D. Martin, W. J. Sterling, and R. G. Roberts, *Phys. Lett.*, **B306**, 145 (1993).

46. CTEQ Collaboration, H. L. Lai et al., Michigan State University Report MSU-HEP-41024, October 1994.

47. M. Glück, E. Reya, and A. Vogt, *Phys. Lett.*, **B306**, 391 (1993).